NOVEL TECHNOLOGIES FOR REAL-TIME FLUORESCENT LIFETIME IMAGING DATA ACQUISITION AND PROCESSING FOR CLINICAL DIAGNOSIS

A Dissertation

by

RODRIGO CUENCA MARTINEZ

Submitted to the Office of Graduate and Professional Studies of
Texas A&M University
in partial fulfillment of the requirements for the degree of

DOCTOR OF PHILOSOPHY

Chair of Committee,	Javier Jo
Committee Members,	Kristen Maitland
	Vladislav Yakovlev
	Friedhelm Schroeder
Head of Department,	Anthony Guiseppi-Elie

May 2017

Major Subject: Biomedical Engineering

ABSTRACT

Endogenous Fluorescence Lifetime Imaging (FLIM) is a noninvasive technique that has been explored with promising results in a wide range of biomedical applications, including clinical diagnosis. A central issue for the translation of FLIM into the medical field is the development of a robust, fast and cost-effective FLIM instrumentation suitable for *in vivo* tissue imaging. This thesis directly addressed some of the technical limitations that must be overcome to enable clinical applications of FLIM. The following specific aims were accomplished.

First, endogenous FLIM imaging and high-resolution reflectance confocal microscopy (RCM) were integrated into a multimodal bench-top optical system. This multimodal system was used to image oral epithelial cancer in a hamster cheek pouch model. Second, an endoscopic system for fast (0.5-4 frames/second) endogenous wide-field FLIM imaging of oral lesions was developed. The FLIM endoscope system is being evaluate at Texas A&M University College of Dentistry, where more than 80 patients presenting oral lesions suspected of pre-cancer or cancer have been imaged up to date. Third, a novel fluorescence lifetime estimation algorithm was developed to achieve robust, accurate, and real-time fluorescence lifetime estimation. This algorithm is enabling real-time FLIM image processing and visualization during the endoscopic examination of patients with suspicious oral lesions. Finally, the endoscopic endogenous FLIM data from suspicious oral lesions collected at the Texas A&M College of Dentistry was used to develop machine learning algorithms for automated identification of pre-cancerous and cancerous lesions from benign oral epithelial lesions. Our results indicate

that endogenous FLIM endoscopy can detect oral epithelial pre-cancer and cancer from a wider range of benign conditions, with levels of sensitivity and specificity above 85%.

Altogether, this work has demonstrated the potentials of endogenous FLIM endoscopy as a clinical tool for early detection of oral epithelial cancer.

DEDICATION

To my beloved wife Emma and my daughter Vanessa whose patience, support and love made it possible for me to finish my PhD.

ACKNOWLEDGEMENTS

I would like to thank my committee chair, Dr. Javier Jo, for his help, guidance and support throughout the course of this research.

Thanks to my committee members, Dr. Kristen Maitland, Dr. Vladislav Yakovlev and Dr. Friedhelm Schroeder, for their help and time.

Thanks also go to my friends and colleagues and the department faculty and staff for making my time at Texas A&M University a great experience.

Finally, special thanks to all who participated directly into my research project Dr. Bilal Malik, my colleagues, now doctors, Joey Jabbour, Shuna Cheng and Cory Olsovsky, and our team at Texas A&M University College of Dentistry, Dr. Lisa Cheng, Dr. John Wright, Lee Jordan and the stomatology clinic personal.

CONTRIBUTORS AND FUNDING SOURCES

Contributors

This work was supervised by a dissertation committee consisting of Dr. Javier Jo (advisor), Dr. Kristen Maitland and Dr. Vladislav Yakovlev of the Department of Biomedical Engineering and Dr. Friedhelm Schroeder of the Department of Veterinary Medicine and Biomedical Sciences.

The bench-top optical systems from Section 3 were designed and developed by Dr. Shuna Cheng (FLIM subsystem) and Dr. Joey Jabbour (RCM subsystem). The handheld optical system from Section 4 was designed and developed by Dr. Shuna Cheng. The data used for developing the algorithms in Section 6 was collected in collaboration with Dr. Lisa Cheng and Dr. John Wright from the Department of Diagnostic Sciences, Texas A&M College of Dentistry, Lee Jordan and the students and doctors from the Stomatology Clinic at Texas A&M College of Dentistry, and Dr. Joey Jabbour, Dr. Shuna Cheng, Dr. Bilal Malik and Dr. Cory Olsovsky from the Department of Biomedical Engineering, Texas A&M Universtity.

All other work conducted for the dissertation was completed by the student, under the advisement of Dr. Javier Jo of the Department of Biomedical Engineering.

Funding Sources

This research was supported by the CONACyT fellowship, the 2015 Optics and Photonics Education Scholarship by SPIE, the Qatar National Research Fund (NPRP grant

8-1606-3-322), and the National Institutes of Health (grants R01CA138653, R01HL11136).

NOMENCLATURE

°C	Degree Celsius
9-CA	9-Cyanoanthracene
τ	Lifetime
μm	Micrometers
μJ	Microjoule
ANN	Artificial Neural Network
ANSI	American National Standards Institute
APD	Avalanche Photodiode
B	Benign
BDE	Blind Deconvolution Estimation
CADSS	Computer Aided Decision Support Systems
CCD	Charge Coupled Device
CMM	Center of Mass Method
dB	Decibel
DM#	Dichroic Mirror
DMBA	Dimethylbenz[α]anthracene
Dys	Dysplasia
Dys/SCC	Dysplasia or Squamous Cell Carcinoma
EP	Error Percentage
f	Focal length

F#	Filter
FAD	Flavine Adenine Dinucleotide
fIRF	Fluorescence Impulse Response Function
FLERIT	Fluorescence Lifetime Estimation via Rotational Invariance Techniques
FLIM	Fluorescence Lifetime Imaging
FOV	Field of View
fps	Frames per second
FWHM	Full Width at Half Maximum
GB	Gigabytes
GHz	Gigahertz
GUI	Graphic User Interface
H&E	Hematoxylin and Eosin
Hz	Hertz
ICCD	Intensified Charge Coupled Device
kHz	Kilohertz
L#	Lens
L-domain	Legendre domain
LOOCV	Leave-One-Out Cross-Validation
LOOPCV	Leave-OnePatient-Out- Cross Validation
LSIR	Least-Square Iterative Reconvolution
M	Molar
mm	Millimeter

mM	Millimolar
MPE	Maximum Permissible Exposure
mRMR	Minimum Redundancy Maximum Relevance
MSE	Means Square Error
NADH	Nicotamide Adenine Dinucleotide
NaOH	Sodium Hydroxide
NIR	Near Infrared
ns	Nanosecond
PBS	Phosphate Buffered Saline
PCA	Principal Component Analysis
POPOP	1,4-bis (5-phenyloxazol-2-yl) benzene
ps	Picosecond
QDA	Quadratic Discriminant Analysis
RCM	Reflectance Confocal Microscopy
RLD	Rapid Lifetime Determination
RMS	Root Mean Square
SCC	Squamous Cell Carcinoma
SFS	Sequential Forward Search
SGOI	Segmented Gated Optical Imager
SNR	Signal to Noise Ratio
TCSPC	Time Correlated Single Photon Counting
UV	Ultraviolet

TABLE OF CONTENTS

Page

LIST OF FIGURES

Page

LIST OF TABLES

Page

1. INTRODUCTION

1.1 Motivation

Fluorescence lifetime imaging (FLIM) is a noninvasive technique that acquire the temporal decay of the fluorescence allowing us to calculate the fluorescence lifetime. FLIM has been used with promising results in a wide range of biosciences applications such as cancer diagnosis [1-3], cardiovascular diseases [4, 5] and monitoring cellular parameters[6, 7]. A central issue for the translation of FLIM into the medical field is the development of a robust, fast and cost-effective FLIM instrumentation suitable for *in vivo* tissue imaging [8]. Real time tissue imaging can help the physician to locate tumors and define borders between normal and abnormal tissues [9]. Being able to identify tissue abnormalities and composition in real time has the potential to significantly advance patient care [9].

The motivation of this work is to develop technologies that allow us to achieve real-time FLIM data acquisition and data processing. As a particular application, this work has been focused on the early detection of oral cancer.

1.2 Oral Cancer

Close to 50,000 Americans will be diagnosed with oral or pharyngeal cancer in 2017 and only 64% will be alive in 5 years[10]. In 2017 it will cause over 9,000 deaths. The death rate of oral cancer is higher than that of more common cancers such as cervical cancer, Hodgkin's lymphoma, cancer of the testes, and endocrine system cancers[11]. However, when detected in early stages, oral cancers can have a five-year survival rate as

high as 80% [10]. Sometimes, oral cancer is only detected when it has metastasized to another location. This can be mainly attributed to the current method of diagnosis of oral lesions, which are based on a visual inspection followed by biopsies when needed and also because in its early stages, oral cancer may not be noticed by the patient, as it can frequently prosper without producing pain or symptoms [11]. There are several types of oral cancers, but around 90% are squamous cell carcinomas (SCC), squamous cell compose most of the skin's upper layers (the epidermis) [11].

Due to the superficial location of oral lesions, optical techniques have shown considerable promise towards early detection of pathological changes and are being explored for noninvasive detection of early cancer. The progression of a malignant lesion is accompanied by both biochemical changes (such as alterations in the relative abundances of tissue autofluorophores) and morphological changes (such as epithelial thickening or changes in the nucleus-to cytoplasm ratio). However imaging systems are typically designed to either have a macroscopic view with low resolution or to have high resolution within a limited field of view [2]. An optical system that can provide information about tissue biochemistry and morphology, has the potential to improve diagnosis and diagnostic yield by identifying the most advanced state of disease within the oral cavity [12, 13].

1.3 Computer Aided Decision Support Systems

Computer Aided Decision Support Systems (CADSS) has become one of the major research topics in medical imaging field [14]. Such systems are designed to detect

and/or classify abnormalities and thus assist a medical expert in improving the accuracy of medical diagnosis and reduce variability amongst expert opinions. The concept of CADSS has been widely applied into real clinical practice because the correct computer output has the ability to assist clinicians in improving their medical decisions. So far, CADSS can play an important role in medical imaging of cancer by differentiating between benign and malignant lesions.[15].

There are three main components in CADSS: feature detection, feature extraction, and classification algorithm. A feature is any property you can measure from the tissue; in our particular case, features could include tissue autofluorescence intensities and lifetimes at certain emission wavelengths. Feature detection is the process to calculate these features from the measured data. Feature extraction is the process to transform the detected features into a lower dimensional space. Most of the times, the number of features is high and even for low number of features, the number of combinations become very large. One of the most used feature extraction algorithms is Principal Component Analysis (PCA), which is a process to reduce the data dimension by removing correlations among the data and to describe the sample by fewer feature vectors while retaining the necessary information of recognition [16]. Another popular feature extraction algorithm is the Minimum Redundancy Maximum Relevance (mRMR) algorithm, a filter based approach to perform feature selection [17]. mRMR aims at selecting features that are mutually different but are highly relevant for classification. A special type of feature extraction is feature selection, in which each original feature is simply either retained or discarded. Finally, classification is the process of assigning each input vector of features into one of

a finite number of discrete categories. In this work we proposed using a quadratic discriminant analysis (QDA) as the classification algorithm. QDA models the likelihood of each class as a Gaussian distribution, then uses the posterior distributions to estimate the class for a given input [18].

1.4 Objectives Dissertation Outline

A central issue for the translation of FLIM into the medical field is the development of a robust, fast and cost-effective FLIM instrumentation suitable for *in vivo* tissue imaging. This thesis directly addressed some of the technical limitations of FLIM needed to overcome to enable clinical applications of FLIM. The following objectives were accomplished. First, endogenous FLIM imaging and high-resolution reflectance confocal microscopy (RCM) were integrated into a multimodal bench-top optical system. Second, an endoscopic system for fast (0.5-4 frames/second) endogenous FLIM imaging of oral lesions was developed and tested on patients. Third, a novel fluorescence lifetime estimation algorithm was developed to achieve robust, accurate, and real-time fluorescence lifetime estimation. Finally, the data collected with the endoscopic FLIM system was used to develop a classifier for automated identification of pre-cancerous and/cancerous from benign oral epithelial lesions

The remaining sections of this dissertation are organized as follows. Section 2 provides an introduction to basic concepts of fluorescence and an overview of FLIM. Section 3 focuses on the bench-top combined FLIM-RCM system. Section 4 presents the handheld FLIM endoscope which has been used to collect data from patients at Texas

A&M College of Dentistry. Section 5 describes the novel bi-exponential deconvolution algorithm for real-time FLIM. Section 6 describes the classifier for automated identification of pre-cancerous and cancerous from benign oral epithelial lesions, and present the results. Finally in Section 7, some concluding remarks and future work are discussed.

2. FLUORESCENCE LIFETIME IMAGING

2.1 Fluorescence

Fluorophore is the term commonly used to define fluorescent substances. When a fluorophore absorbs a photon it gets excited from its ground state to a higher energy state. Once in the higher energy state, the fluorophore can return to its ground state through different methods such as internal conversion or vibrational relaxation (no light emission), fluorescence, intersystem crossing and phosphorescence, as illustrated in the Jablonski diagram provided in Figure 1. The singled ground, first and second electronic states are depicted by S_0, S_1, and S_2, respectively. At each electronic energy levels the molecule can exist in a number of vibrational energy levels, depicted by 0, 1, 2, etc. The transition between states are depicted as vertical lines.

Again, after light absorption, several processes can occur. The fluorophore is excited to a higher vibrational level, S_1 or S_2. Then the fluorophore rapidly relax to the lowest vibrational levels of S_1 through internal conversion. Once in the S_1 state, the fluorophore can relax to one of the vibrational states of S_0 through a radiative process. This process is called fluorescence and is typically in the order of nanoseconds. Molecules in the S_1 state can also undergo a spin conversion to the first triplet state T_1 through intersystem crossing. Transition from T_1 to the S_0 is also a radiative process and is called phosphorescence. Since this transition is forbidden, the rate of phosphorescence is several orders of magnitude smaller than those for fluorescence [19].

As mentioned before, there are several vibrational levels per electronic level, and since the transitions can go from and to any of this vibrational levels, the fluorophore can

absorb and emit fluorescence in a broad spectrum. Some transitions are more likely than others; the most probable transition from S_0 to an excited state yields to the peak of the absorption spectrum. In the same way, the most probable transition from an excited state to the ground state yields to the peak of the emission spectrum. Since the vibrational energy levels have similar spacing in S_0 and S_1, the absorption and the emission spectrum in general have a symmetric nature.

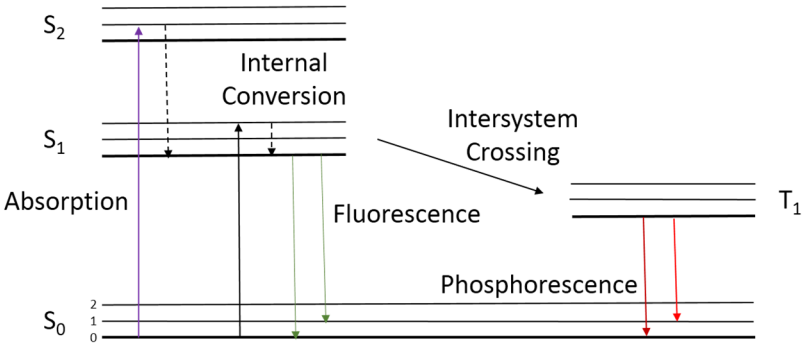

Figure 1. Jablonski diagram illustrating the various electronic and vibrational states of a molecule.

2.2 Fluorescence Lifetime and Quantum Yield

Fluorophores are often conjugated to a macromolecule and can be used as fluorescent dyes. Quantum yield and fluorescence lifetime are perhaps the most important characteristics of a fluorophore [19]. The fluorescence quantum yield is the ration of the number of photons emitted to the number of photons absorbed and is given by:

$$\phi = \frac{k_r}{k_r + k_{nr}} \quad \textbf{(1)}$$

where k_r is the radiative rate constant, and k_{nr} the non-radiative rate constant. The quantum yield is always less than unity because of Stokes losses [19]. The closer the quantum yield to 1, the easiest it is to measure the emitted fluorescence and the higher signal to noise ratio (SNR) we can obtain from the fluorescence system. This become important when imaging *in vivo* tissue, since there is a limited amount of power you can use in order to not damage the tissue. Quantum yield can be measured by steady-state fluorescence measurements, in which the sample is excited by a constant light source and fluorescence intensity is recorded. Since the fluorescence decay is in the order of nanoseconds, when the sample is excited, steady state is reached essentially instantaneously.

The fluorescence lifetime is defined as the average time the fluorophore spends in the excited state and is given by:

$$\tau = \frac{1}{k_r + k_{nr}} \quad \textbf{(2)}$$

The actual time the molecule spends in the excited state before emitting a fluorescent photon and returning to the ground state is a random variable with a characteristic probability distribution which is specific to that fluorophore. Because of this, the fluorescence intensity over time follows an exponential decay [19] and in the case of a single decay it can be expressed as:

$$I(t) = I_0 e^{-t/\tau} \quad \textbf{(3)}$$

where I_0 is the intensity at t = 0, t is time and τ is the lifetime.

2.3 Fluorescence Lifetime Imaging

FLIM is a noninvasive time-resolved technique that calculates the fluorescence lifetime in a two-dimensional space. FLIM techniques can be divided in time-domain and frequency-domain. Time-domain and frequency-domain are related via the Fourier transform and provide equivalent information on the fluorescence decay. In frequency-domain, the excitation light is modulated at certain frequencies and the phase difference is measured between the fluorescence emission and the excitation light [19]. In time-domain, the fluorescence decay is directly measured as a function of time upon excitation with a pulse of light [19]. Time-domain can be implemented using a time-correlated single photon counting (TCSPC) , time gated imaging or pulse sampling using a digitizer. The work presented in this dissertation is focused on the time-domain technique.

In time-domain FLIM by TCSPC the sample is scanned by a high-frequency pulsed laser. Data recording is done by detecting single photons, and measuring the arrival times of the photons with respect to the pulse excitation time at each pixel of the image [20]. For each pixel a histogram of the arrival time is generated. This histogram represents the fluorescence intensity decay as a function of time. The main advantages of TCSPC are: high sensitivity, high temporal resolution, low pulse energy and low noise. The main disadvantages are its slow acquisition speed and high cost.

In time-domain FLIM by pulse sampling a relatively high energy pulse generate a complete temporal decay, then this temporal decay is sampled using a high speed digitizer. The advantage of this method is the pixel rate speed, which could reach the laser repetition rate. The main disadvantages are the low temporal resolution, limited

by the instrument response, high noise, due to the low photon efficiency, and the use of a relatively high energy pulses which can damage the sample.

In time-domain FLIM by time gated, the imaging is usually accomplished in wide field by a gated intensified charge coupled device (ICCD). As in the pulse sampling, a relatively high energy pulse generate a complete temporal decay but now the temporal decay is recorded by the image intensifier. The gate of the ICCD opens at specific time to detect the fluorescence intensity. By taking successive images for different delay of the gate, an exponential decay can be reconstructed. Gated image intensifiers are typically used in combination with wide-field excitation. The benefit of wide-field imaging is that the spatial information is acquired at the same time for all pixels. The disadvantage is the low sensitivity, low temporal resolution and poor spatial resolution.

2.4 Literature Review – Lifetime Calculation Algorithms

In time-domain FLIM, the measured fluorescence decay $y(n)$ is the convolution of the fluorescence impulse response function (fIRF) $h(\ n)$ and the instrument response $x(n)$:

$$y(n) = h(n) * x(n) \quad \textbf{(4)}$$

In order to estimate the fluorescence lifetime, $h(n)$ must be estimated, and in order to estimate $h(n)$, the instrument response must be deconvolved from the measured fluorescence decay [19-21]. The most common deconvolution method is the least-square

iterative reconvolution (LSIR) [21]. Using a multi-exponential model, LSIR can estimate the parameters of the model that minimizes the residuals between its convolution with the instrument response and the measured fluorescence decay. The main disadvantage of LSIR is that even with numerical methods such as Gauss-Newton and Levenberg-Marquardt algorithms, the method involves iterative computations, making real-time calculations impossible.

There are several different algorithms that have been implemented to estimate fluorescence lifetimes and can be divided in two. Algorithms that implement the deconvolution of the instrument response to the measured decay and algorithms that do not implement the deconvolution. In general the algorithms that do not implement the deconvolution are faster, but they are less precise, more sensitive to noise and only accurate for mono-exponential decays. In the other hand, algorithms for FLIM processing based on deconvolution offer a better estimation of the fluorescence decay, are more robust to noise, can solve multi-exponential models but in consequence they are time consuming and not suitable for real-time FLIM. A review of the more used fast algorithms are presented next.

2.4.1 Rapid Lifetime Determination (RLD)

A class of techniques for faster lifetime calculation called Rapid Lifetime Determination methods (RLD) has been developed for real time applications [22]. RLD calculates the lifetime by dividing the fluorescence decay curve into areas of fixed time width, which then are used to calculate the lifetime. Since the RLD collects the decay

data in only a few areas, it is less precise but considerably faster than multiple methods.

2.4.2 Center of Mass Method (CMM)

Assuming a mono-exponential decay this method calculate the coordinate *t* of its center of mass which corresponds to the average fluorescence lifetime. The advantage of this method is the simplicity and speed to estimate the average lifetime. Its main limitation is the high sensitivity to noise.

2.4.3 Method of Successive Integration

An extension from the linear regression of the sum method [23] and is based on the fact that integration of an exponential function is another exponential function. In this way, the original function can be found again in integral form and solved using numerical methods [24, 25]. This method has better performance than the RLD and CMM methods but is slower.

2.4.4 Fluorescence Lifetime Estimation via Rotational Invariance Techniques (FLERIT)

Based on an algorithm called estimation of signal parameters via rotational invariance techniques, since this algorithm use more complex calculations like, correlation matrices, singular value decomposition and eigenvalues, it is considerably slower than the previous methods. Its advantage is that it can resolve multi-exponential decays [26].

2.4.5 Artificial Neural Network FLIM (ANN-FLIM)

ANN-FLIM uses an ANN to estimate the fluorescence lifetime. The ANN is trained with synthesized samples using the fluorescence decay as input and the biexponential parameters as their matching vectors. Once trained, ANN-FLIM is able to estimate the parameters from an unknown fluorescence decay. This technique can be extremely fast and accurate, unfortunately is very susceptible to noise.

2.4.6 Phasor Approach

The phasor approach is used in the frequency domain, the idea is to transform the acquired data of each pixel into a phasor. The resulting coordinates can be represented in a phasor plot as a two dimensional histogram. Single exponential lifetimes are located on the edge of the semicircle. For multi-exponential lifetime decays, the phasor is given by the normalized linear combination of the component phasors [27]. The advantage is that it's fast, the disadvantage is that is performed in the frequency domain.

2.4.7 Laguerre Deconvolution Method

The Laguerre deconvolution method is a model-free method based on the Laguerre expansion of the kernel technique [28]. The fIRF is expanded on orthonormal sets of discrete Laguerre functions, and allows fast converging kernel estimation [28, 29]. This method has been proven to be a fast, robust, and model-free algorithm to estimate the fIRF. The original algorithm has two limitation, the first is that the resulting fIRF might not have a monotonic decay [30], the second limitation is the need to choose a priori

optimal values of the Laguerre parameter α to get good estimation of the fIRF. These two limitations can been addressed, first, by imposing a constrained quadratic optimization to compute the scaling coefficients [31] and second, by a method to automatically select the best value of α [29, 32].

2.4.8 Legendre Space Fitting and Filtering

In this method the measured fluorescence decay is transformed into the Legendre domain (L-domain) reducing the dimensionality of the signal into a few Legendre components. Moreover, removing the higher components in the L-domain e.g. just keep the first 10 components, acts as a filter in the time-domain, reducing even more the dimensionality. After the transformation, a nonlinear least square fitting is conducted. The advantage of this method, in addition that filters the signal, is that the fitting algorithm is done in the L-domain with a few Legendre components instead of all the samples. The limitation of this method is that you still need to do a nonlinear fitting method.

2.4.9 Blind Deconvolution Estimation (BDE)

The BDE algorithm solves a quadratic approximation problem, where the decision variables are the samples of the instrument response and the scaling coefficients of the fluorescence impulse response modeled by Laguerre functions. The problem is solved using an alternating least squares methodology that iteratively estimates the instrument response and scaling variables [30]. The advantage of this method is that it does not require previous knowledge of the instrument response, while its main limitation is speed.

2.4.10 Global Fit Analysis

The Global analysis can simultaneously fit the fluorescence decay of all pixels in an image or dataset to a multi-exponential model under the assumption that the lifetime components are invariant across the image [33]. By doing this the algorithm can be used to simultaneously fit an entire dataset assuming that only the fractional contributions of a limited number of unknown but spatially invariant lifetime components vary from pixel to pixel [33]. The advantage of this method is that it can fit the fluorescence decay even when the number of detected photons per pixel is low. The main limitation is that it only fits the fluorescence decay to a combination of a fixed number of fluorescence lifetime components, and even that is faster than a nonlinear analysis is not fast enough for real-time applications.

2.4.11 Library of Exponentials

This method assumes that the fluorescence impulse response at each can be represented by the conical combination of a library of N pre-defined exponential functions. This method searches for the scaling coefficients of the library by non-negative least squares approximations plus Thikonov/l2 or l1 regularization terms [34].

2.5 Literature Review – High-Speed FLIM Systems

In this section several FLIM systems attempting real-time FLIM measurements are being reviewed. In most cases, in order to achieve real-time frame rates, fast but not accurate lifetime calculation algorithms were adopted.

A single-shot wide-field FLIM instrument based on a segmented gated optical imager (SGOI) was reported by Elson *et. al.* [35]. In this image intensifier the photocathode is split into quadrants, which provide channels that can be gated at different delay times. They were able to acquired FLIM data at 20 frames per second using a two gates RLD algorithm to display the FLIM images. A wide-field fluorescence lifetime imaging reported by McGinty *et.al.* [36] used the RLD method in a wide-filed FLIM microscope to achieve frame rates of ~7.7 Hz. In this system a CCD camera acquired 2 time-gated images at different delays. Another approach using a CCD camera by Grant *et. al.* [37] achieved full frame rate (336 x 256 pixels) of 10 fps. Using the CMM algorithm Shrestha *et. al.* [8] reported a multispectral FLIM system capable of image at a pixel rate of 20 kHz. Becker *et. al.* [38] built an eight-channel parallel FLIM system were they use 8 TCSPC channel in parallel and a multichannel PMT detector to increase the counting capability 8 times. They report acquisition of 256 x 256 pixels images at 4 frames per second or 262 kHz pixel rate for lifetimes between 200 ps and 600 ps. Gersbach *et. al.* [39] combined wide-field with TCSPC using an array of 32 x 32 single-photon avalanche diodes. They reported frame rates of 14.5 frames per second, almost 15 kHz pixel rate for lifetimes between 900 ps and 1800 ps.

3. MULTIMODAL BENCH-TOP OPTICAL SYSTEM[1]

3.1 Combined FLIM-RCM System

In this section, a description of the combined FLIM-RCM system is presented. More details about the design of the optical system and its validation can be found in [2]. In order to determine specific design parameter for the endoscope system and characterize the system's performance for detecting oral precancer and cancer, a bench-top combined FLIM-RCM system was built[2]. The bench-top system was designed to probe the biochemical properties of tissue on a macroscopic scale (FLIM subsystem) and the cellular morphology with a high resolution (RCM subsystem). In this way FLIM is being used to provide real-time macroscopic images of the tissue detecting suspicious sites to where the RCM can be placed and scan the morphological imaging of the sub-cellular structure of the tissue with small field of view (FOV). A schematic of the integrated system is shown in Figure 2.

[1] Reprinted with permission from "Fluorescence lifetime imaging and reflectance confocal microscopy for multiscale imaging of oral precancer" by Jabbour J.M., Dheng S., Malik B.H., Cuenca R., Jo J.A., Wright J., Cheng Y-S.L., Maitland K.C., 2013. Journal of Biomedical Optics, 18(4), p. 046012, copyright [2013] by Society of Photo-Optical Instrumentation Engineers.

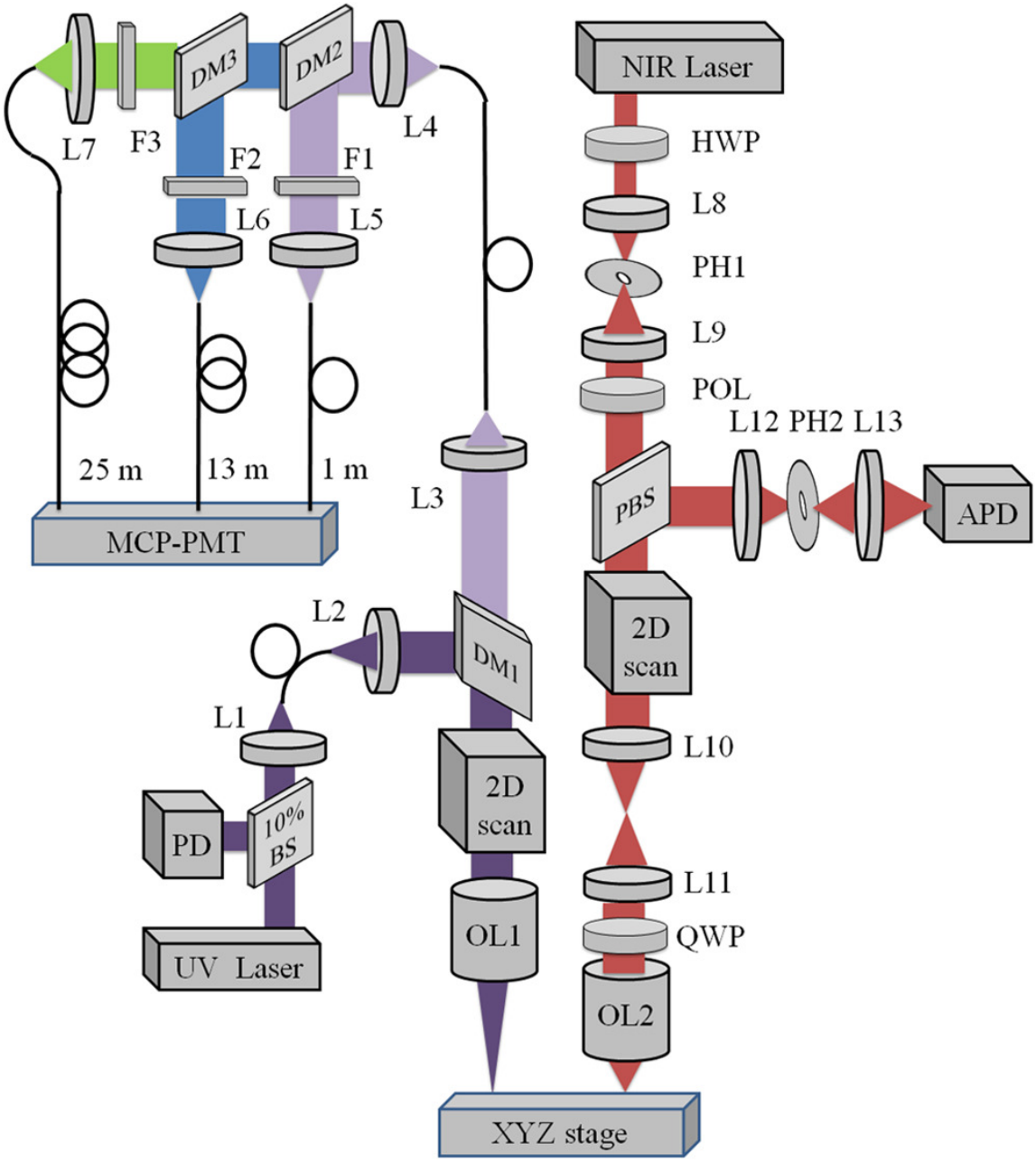

Figure 2. Schematic of both subsystems [2].

3.2 Instrumentation

As shown in Figure 2, a frequency-tripled Q-switched ND: YAG laser (355 nm, <1ns pulse duration, 100 kHz maximum repetition rate, AOT-YVO-100QSP/MOPA, Advanced Optical Technology) was used as excitation. The laser light was coupled into a multimode fiber with a core diameter of 50 μm (FVP050055065, Polymicro Technologies) and delivered to the bench-top system. The output of the excitation fiber was collimated and then reflected by a dichroic mirror (DM1: NC176741-z355rdc, Chroma) to a pair of galvanometer mirror scanners (6200HM40, Cambridge Technology) for two-dimensional raster scanning. A UV-NIR corrected triplet (f=45mm, NT64-837, Edmunds Optics) was used to focus light onto the sample. The fluorescence emission was collected by the same triplet and passed the dichroic mirror (DM1) to the collection fiber with a core diameter 200 μm (BFL22-200, Thorlabs). The output of the collection fiber was launched to a multispectral detection unit which consisted of dichroic mirrors (DM2: T>95%@439-647 nm, LM01-427-25, DM3: T>95%@492-950 nm, FF484-Fdi01, Semrock), bandpass filters (F1: FF01-390/40, F2: FF01-452/45, Semrock), a long pass filter (F3: FF01-496, Semrock) and three multimode fibers with lengths of 1m, 13m and 25m (BFL22-200, Thorlabs). The detection unit separated the fluorescence emission into three spectral bands which were selected based on emission spectrum of the three endogenous fluorophores of interest: collagen (F1: 390 ± 20 nm), nicotinamide adenine dinucleotide (NADH) (F2: 452 ± 22.5 nm) and flavine adenine dinucleotide (FAD) (F3: >500 nm). The three multimode fibers with different lengths provided a time delay of 60ns with 12 meter length difference and helped temperately separate the signals from the three

spectral bands. Therefore, for each laser pulse, three fluorescence decays for three spectral channels could be detected simultaneously with one single detector. The outputs of the three fibers were then detected by a high-speed micro-channel plate photomultiplier tube (MCP-PMT, 180 ps rise time, 90 ps transit time spread, R5916U-50, Hamamatsu), amplified by a preamplifier (C5594-12, Hamamatsu) and sampled by a digitizer at 6.25 GHz (PXIe-5185, National Instruments) using custom software programmed in LabVIEW (National Instruments). For the RCM subsystem a near infrared (NIR) continuous wave diode-pumped solid state laser (1064 nm, 1 W, CL1064-1W0, Crystalaser, Reno, NV) was used as the illumination source. A combination of a half-wave plate and a linear polarizer in the beam path served as a variable attenuator to control the optical power incident on the sample. A spatial filter in the beam path was used to produce a clean Gaussian beam. An 8 kHz resonant scanner and a galvanometer scanner operating at 7 Hz (CRS 8K and 6215HM40, Cambridge Technology) were close-coupled to raster scan the NIR beam. A 2× beam expander filled the back aperture of a water immersion objective lens (60×, 1.0 NA, 2 mm working distance, LUMPLFLN60X/W, Olympus, Center Valley, PA), which focused the light onto the sample. A combination of linear polarizer, polarizing beam splitter, and quarter wave plate were used to remove specular reflections within the optical system. Finally, a spatial filter with a confocal pinhole of 30 μm diameter for optimized system characterization and 50 μm diameter for tissue imaging rejected the out of focus light prior to signal detection by an avalanche photodiode (APD) module (APD110C, Thorlabs). An automated translation stage (XYZ stage) was used to move the sample between the FOVs of the FLIM and the RCM subsystems. A 1951 positive USAF

resolution target placed on a white paper was used to acquire co-registered images from the two subsystems.

3.3 Computer Program

Because both subsystems are custom made, in order to integrate both subsystems, a computer program was developed to control them and keep track of the sample position to co-register the images. The computer program consist of 5 stages: Control Signal Generation, Image Acquisition, Image Processing, Image Visualization and Saving, and Graphic User Interface (GUI).

3.3.1 Control Signal Generation

For the FLIM subsystem, a square signal and two sawtooth signals are generated to trigger the laser and control the galvo mirrors, respectively. To keep the tissue exposure to the laser excitation at a minimum, the laser is turned off during the flyback of both galvo mirrors. Figure 3 shows an example of the signals for an image of 10 x 10 pixels, the green signal is the laser trigger and it can be notices that there are no pulses during the x-axis flyback (blue signal) nor during the y-axis flyback (red signal). For the RCM subsystem, only a sawtooth signal for the galvo mirror is generated. The resonant mirror doesn't need a signal and act as the trigger to synchronize the image acquisition.

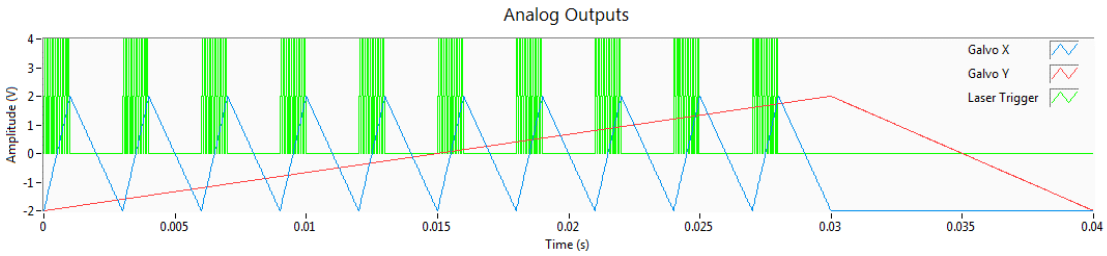

Figure 3. Generated signals for the FLIM subsystem.

3.3.2 Image Acquisition

For the FLIM subsystem we need to be able to acquire and fetch the data to the computer at a faster rate than the trigger repetition rate. Because the action of fetching data consumes a fixed amount of time independently of the number of pixels, it is better to read multiple pixels (1 packet) at the same time than only one pixel. In addition, software pipelining was implemented to avoid dead times between the stages. Figure 4, shows an example of a time diagram for the different stages. In this example, each packet consists of 4 pixels, and one frame consists of 4 packets. In reality, the packet size can vary from 1,600-10,000 pixels and the number of packets can vary from 4-25, depending upon the image size. For the RCM subsystem, since there is only one sample per pixel we, can fetch the whole frame at once. Once the acquisition starts, we wait until we collect the total number of pixels and then fetch them to the computer.

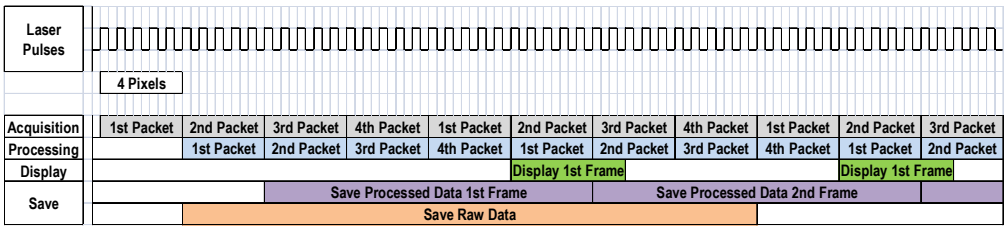

Figure 4. Time diagram for an image size of 4 x 4 pixels.

3.3.3 Image Processing

In this stage we need to process the acquired data to generate the images. For both subsystems we condition the signal by removing some noise, removing the offset and flipping the signal, as depicted in Figure 5. For the FLIM images we also calculate for each pixel: the integrated fluorescence intensity, the normalized integrated fluorescence intensity and the average fluorescence lifetime for each spectral band. The fluorescence impulse response function h(n) is approximated directly from the recorded decay by using only the falling part.

The integrated fluorescence intensity was calculated as:

$$I_{int\_i} = \sum_{n=0}^{N} h(n) \quad \textbf{(5)}$$

where I_{int_i} is the integrated intensity of the spectral band *i*.

The normalized intensity I_{norm_i} of the spectral band *i* was calculated as:

$$I_{norm\_i} = \frac{I_{int\_i}}{I_{int\_1} + I_{int\_2} + I_{int\_3}} \quad \textbf{(6)}$$

The average lifetime was calculated as:

$$\tau_{avg} = \frac{\sum nh(n)}{\sum h(n)} \quad (7)$$

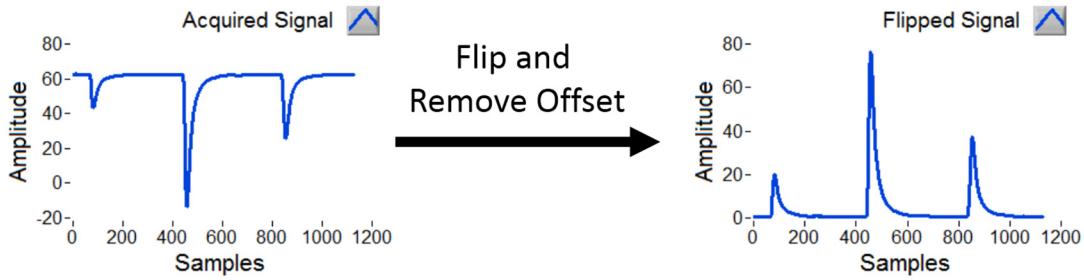

Figure 5. Example of removing the offset and flipping the signal.

3.3.4 Visualization and Saving

In this stage we need to reconstruct the images for each calculated parameter. In the case of the FLIM images, 3 integrated intensities, 3 normalized intensities, and 3 lifetimes are displayed (one for each spectral channel) and the user have the option to save the raw data for a complete frame. In the case of the RCM images, only the intensity is acquired and the frames are always saved as a video.

3.3.5 Graphic User Interface

The GUI let the user modify the laser repetition rate, image size in pixels, field of view in mm, and the sampling rate. Also, the user is able to start and stop the acquisition,

and save the raw data. For the co-registration, the user is able to pick an area on the FLIM image to image with the RCM subsystem. The program automatically translates the selected area onto the RCM subsystem FOV.

3.4 Combined FLIM-RCM System Validation - Tissue Phantom Imaging

A two-layer tissue phantom was developed to test the system's capability to detect the macroscopic biochemical and microscopic morphological properties of a relatively complex sample. The phantom was produced with a thin top layer of 100-120 μm consisting of polymer beads to model the epithelial nuclei. NADH and FAD (Sigma-Aldrich) were also added to the top layer to mimic autofluorescent metabolic coenzymes in the epithelium. The NADH powder was concentrated towards the center and FAD was uniformly distributed throughout this layer. The top layer was set on top of a thick lower layer of collagen matrix which represented of stroma layer. In order to get a homogenous collagen matrix, collagen solution (rat tail tendon type I collagen, BD Biosciences) was used instead of collagen fiber. The dissolved collagen solution was added to 10×phosphate buffered saline (PBS) solution and 1 M sodium hydroxide (NaOH) along with deionized water. The solution was allowed to gel at 37°C for 30 minutes.

Figure 6 shows the results, For the FLIM images only the second and third channels are displayed because we found that the collagen used was only fluorescent at wavelengths lower than 390 nm. As we can see from the normalized intensity images, Figure 6(a) and Figure 6(b), the center of the phantom were NADH and FAD are present, display fluorescent signal in both spectral channels and is impossible to know if the signal

is coming from FAD alone or from both FAD and NADH. Figure 6(c) and Figure 6(d) shows the fluorescent lifetime maps, and Figure 6(e) and Figure 6(f) are their corresponding histograms. As we can see form the histograms the average lifetime for the center of the phantom in the 452 nm channel is 0.32 ± 0.15 ns corresponding to the lifetime of unbound NADH. The average lifetime in the >500 nm channel is 2.08 ±0.15 ns at the periphery which represents FAD, and 1.72 ±0.14 ns in the center which is the lifetime combination of NADH and FAD, probing that with the fluorescent lifetime maps we can differentiate between FAD alone and FAD and NADH together. Figure 6(g) and Figure 6(h) show the confocal images from the top-layer of the tissue phantom at depths of approximately 30 μm and 60 μm, respectively. The polystyrene beads appear as white dots in the reflectance images, and are fairly uniformly distributed over the entire FOV. These results demonstrate that such a two-layer phantom is well-suited to validate our multimodal imaging system.

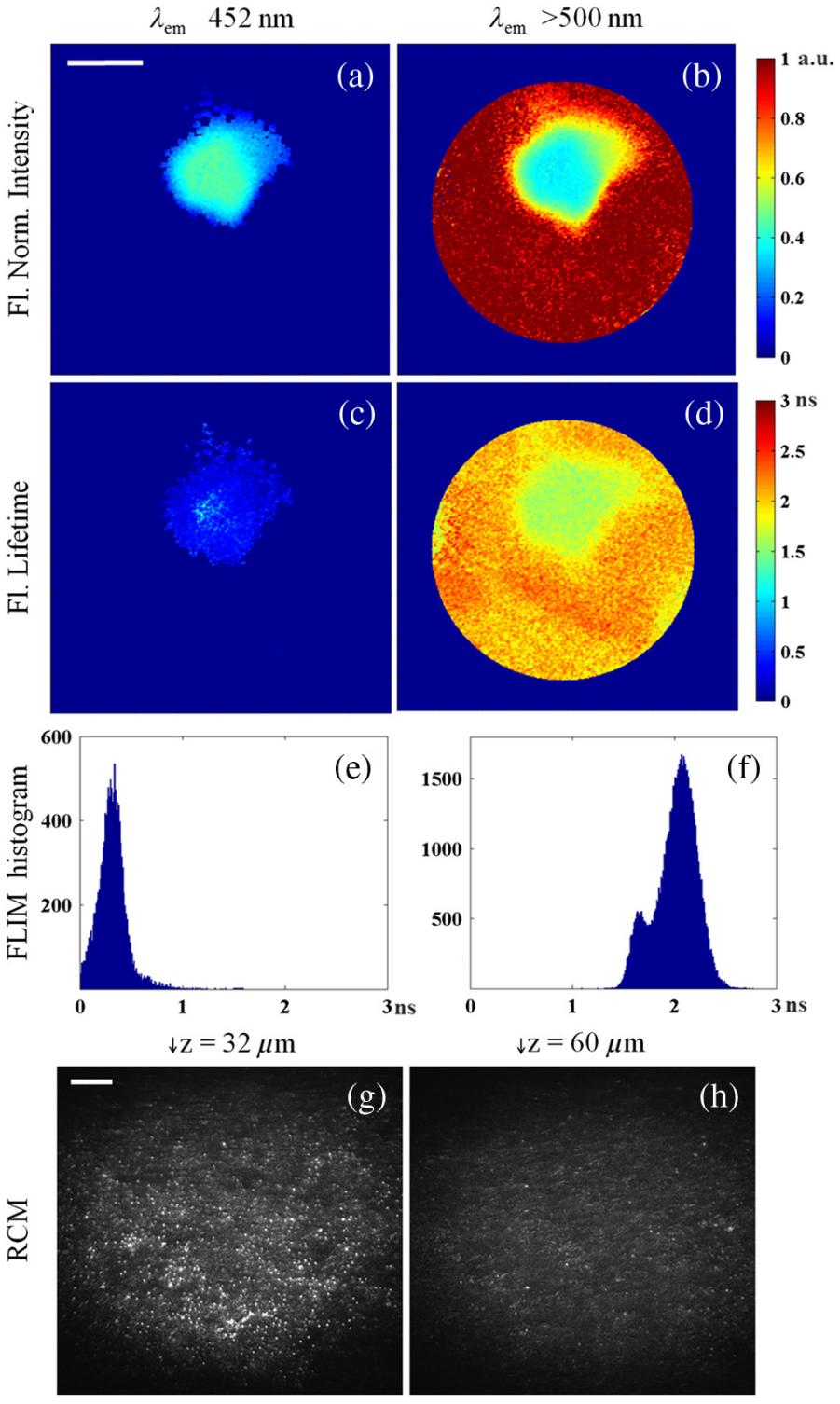

Figure 6. FLIM-RCM images of the two-layer phantom [2].

3.5 Combined FLIM-RCM System Validation – Hamster Cheek Pouch Model

A hamster cheek pouch model of oral cancer was performed to evaluate the system's performance to differentiate cancer from normal tissue. The right buccal pouch of the hamsters was treated 3 times a week for 8 weeks with 0.5% solution of 7,12-dimethylbenz[α]anthracene (DMBA) dissolved in mineral oil. The left pouch was treated with mineral oil to serve as a normal control. Samples were first imaged with the FLIM subsystem, then moved with a translation stage to the RCM subsystem. The FLIM-RCM system software recorded the mapping coordinates of RCM imaging sites for accurate registration to the FLIM image and for localization relative to the edge of the tissue mount. After imaging, the cheek pouches were excised, fixed in 10% formalin, and processed for hematoxylin and eosin (H&E) histology. The software controlled the stage and the user was able to select the locations to image with the RCM from the FLIM images.

Figure 7 show the results for the normal and the DMBA-treated hamster cheek pouch, respectively. Figure 7(a)-(f) show the normalized fluorescence intensity and average lifetime maps for the normal hamster cheek pouch. The results for the normal cheek pouch are consistent with normal tissue where collagen fluorescence is dominant because of the thin epithelium. The RCM images taken from the center of the FLIM FOV at different depths are shown in Figure 7(h) and Figure 7(i), Figure 7(j) is a zoomed view of Figure 7(i) where we can clearly see cell membranes and nuclei identified by arrows. RCM images doesn't show nothing abnormal. Figure 7(l)-(q) show the normalized fluorescence intensity and the average lifetime maps for the DMBA-treated hamster cheek pouch. The label on the arrows 1 and 2 correspond to Region 1 and Region 2 which were

diagnosed as cytologic atypia and low-grade dysplasia respectively. We can notice some differences if we compare both regions and against the normal cheek pouch, for instance the fluorescence lifetime in the 452 nm channel is shorter, we can attribute this to the presence of NADH, and the fluorescence lifetime in the 500 nm channel is longer, indicating contribution of both FAD and porphyrin. The RCM images of Region 1 just below the surface (Figure 7 (s)) and deeper in the epithelium (Figure 7 (t) and Figure 7(u) zoomed in) show very small features that may be epithelial nuclei or possibly nucleoli that can be seen in the corresponding histology section in Figure 7(v). In contrast, the RCM images of the epithelium in Region 2, shown in Figure 7(w), Figure 7(x) and Figure 7(y) zoomed in, show much larger nuclei indicative of precancerous changes. Arrows in RCM images identify cell nuclei.

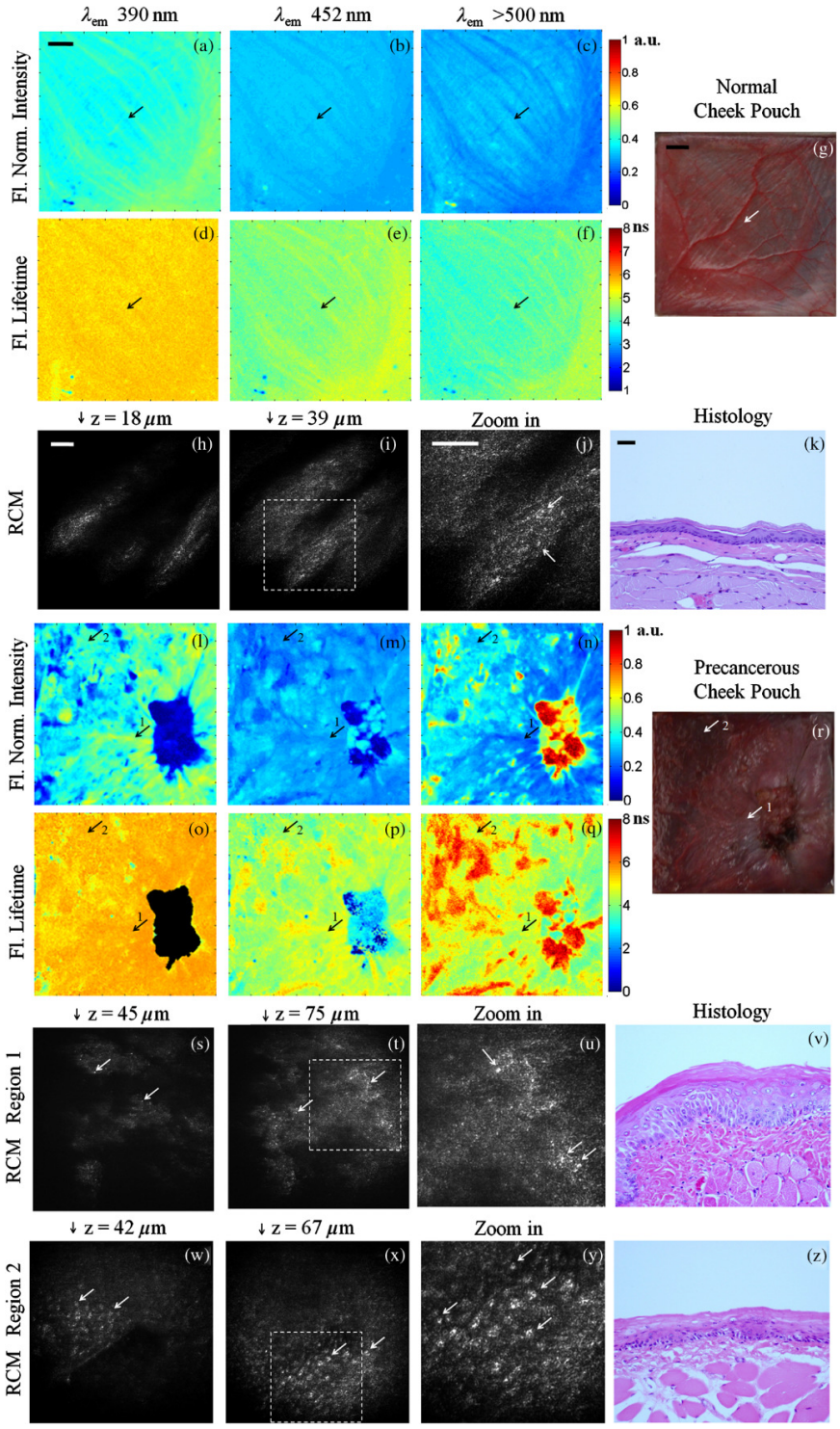

Figure 7. ***In vivo*** **FLIM-RCM images of normal hamster cheek pouch [2].**

3.6 Discussion and Conclusion

This work shows that our dual-modality multispectral FLIM and RCM imaging system can effectively image biochemical and morphological features in tissue. While large-field FLIM enables fast macroscopic tissue evaluation, it lacks the ability to provide optical sectioning and high spatial resolution for cellular evaluation. The RCM subsystem can provide much higher spatial resolution and optical sectioning necessary for cellular imaging but has a limited FOV. The combination of these two imaging techniques on a single platform offers an important and powerful tool utilizing the strengths of the individual subsystems. The complementary information acquired from the integration of the two modalities is important for the study of biological changes such as those seen in the progression of early cancer.

In all instances, FLIM imaging provides macroscopic biochemical maps which represent the relative contribution of the endogenous fluorophores, both with respect to fluorescence intensity and lifetime. While the FLIM images of the tissue phantom show some physical features due to the geometry of the phantom and the distribution of NADH and FAD, the images of the biological samples showed differences in intensity and lifetime signals between normal and cancer. In comparison, the hamster tissue has a wide range of pathologies, resulting in spatial features in both the intensity and lifetime images. Additionally, the spectral and lifetime data of the DMBA-treated pouch is different than the normal control pouch, indicating the ability to detect precancerous changes. By comparing the normalized intensity and average lifetime values in Table 1, differentiation between normal and tumorous tissue may be achieved with intensity measurements alone.

However, based on some similarity in normalized intensity values and differences in lifetimes between normal tissue and the DMBA-treated RCM Regions 1 and 2, the more challenging and relevant problem of distinguishing between benign and precancerous lesions may be realized with FLIM. It should be noted that the histopathological difference between the normal and pre-cancerous lesions being compared are very subtle; yet, difference in the FLIM signal could already be observed. Nevertheless, the high resolution of RCM is still necessary for identifying cellular changes indicative of precancer.

The results from the high-resolution reflectance confocal microscope demonstrate the potential of the imaging system towards characterization of sub-cellular morphological features of the epithelial tissue. The brighter nuclei against the darker background can be delineated in the RCM images. The normal cell nuclei in the porcine tissue are on the same scale as the normal human epithelial cell nuclei. Although the normal hamster epithelial nuclei are smaller, they are still detectable with our RCM imaging system. An increase in nuclear size is distinguished between normal and dysplastic tissue in hamster cheek pouch. The RCM system was able to distinguish between two pathologically different regions that look similar using FLIM. This shows the importance of these two complementary techniques.

Table 1. Normalized fluorescence intensity and average lifetime for phantom, normal hamster and DMBA treated hamster.

Sample	λ_{em}	390 nm		452 nm		>500 nm	
		Intensity	Lifetime	Intensity	Lifetime	Intensity	Lifetime
Phantom	Center	--		0.48 ± 0.08	0.32 ± 0.15	0.45 ± 0.08	1.72 ± 0.14
	Outer	--		--		0.88 ± 0.09	2.08 ± 0.15
Normal Hamster	Entire FOV	0.42 ± 0.04	5.61 ± 0.13	0.30 ± 0.01	4.60 ± 0.25	0.28 ± 0.03	4.22 ±0.29
DMBA Treated Hamster	Tumor	0.06 ± 0.03	5.43 ± 0.14	0.19 ± 0.11	2.62 ± 0.79	0.75 ± 0.14	5.62 ± 1.27
	Region 1	0.49 ± 0.02	5.49 ± 0.16	0.28 ± 0.01	4.32 ± 0.18	0.23 ± 0.02	4.03 ± 0.21
	Region 2	0.42 ± 0.02	5.43 ± 0.14	0.27 ± 0.01	4.29 ± 0.29	0.30 ± 0.01	5.16 ± 0.34

In conclusion, we have presented the design and development of a dual-modality multi-scale bench-top FLIM—RCM imaging system applied to the characterization of oral epithelial tissue. The integrated system is capable of identifying both morphological and biochemical features, which together can potentially serve as a powerful diagnostic aid towards classification of pathological condition of the tissue.

4. HANDHELD MULTISPECTRAL FLIM ENDOSCOPE[2]

4.1 Handheld Multispectral FLIM Endoscope System

In order to use the previous FLIM subsystem on human patients and be able to image them *in vivo*, the FLIM subsystem was converted into an endoscope probe. The endoscope was validated with standard dyes, hamster cheek pouch, human oral biopsy imaging *ex vivo* and human oral imaging *in vivo*. The system is based on the point scanning direct pulse recording implementation, using safe and permissible exposure levels at pixel rate of several tens of kHz. Taking advantage of this high pixel rate, we were able to perform the fastest *in vivo* multispectral FLIM imaging in the human oral cavity. Also with this system we were able to report the first demonstration of real-time deconvolution of the instrument response from the fluorescence decay at each pixel of the image, which allowed accurate real-time lifetime map estimation and visualization at multiple spectral bands simultaneously. The system is currently in use at Texas A&M University College of Dentistry in Dallas, where more than 80 patients presenting oral lesions have been imaged up to date.

[2] Reprinted with permission from "Handheld multispectral fluorescence lifetime imaging system for *in vivo* applications" by Cheng S., Cuenca R.M., Liu B., Malik B.H., Jabbour J.M., Maitland K.C., Wright J., Cheng Y-S.L., Jo J.A., 2014. Biomedical Optics Express, 5(3), p. 921-931, Copyright [2014] by The Optical Society.

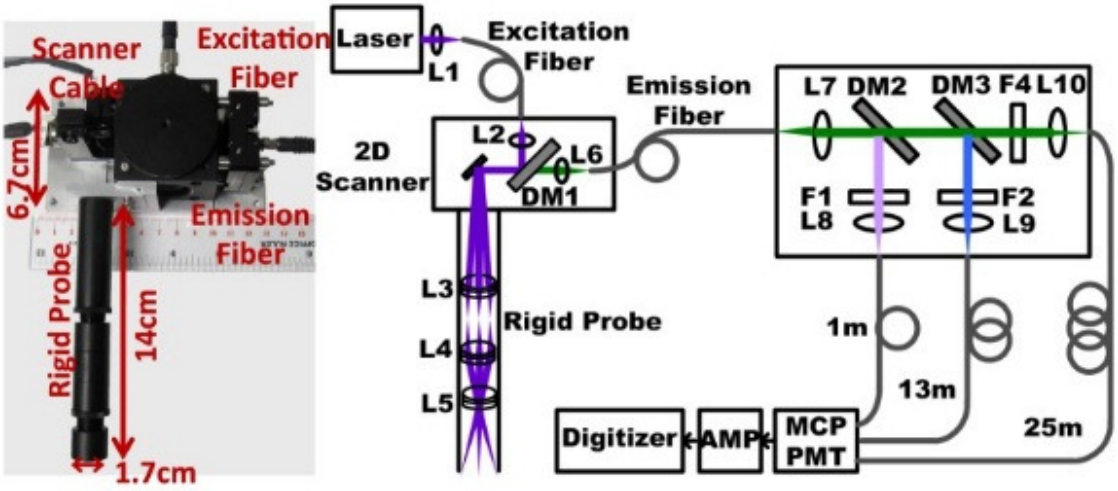

Figure 8. Photograph of the handheld rigid endoscope and schematic of the system [40].

4.2 Instrumentation

The system consists of a handheld box (volume: 7 × 13 × 5 cm3, mass: 450 g) fitted with a custom-designed rigid endoscope (length: 14 cm, diameter: 1.7 cm) as shown in Figure 8. The schematic of the proposed system is also shown in Figure 8. A frequency-tripled Q-switched Nd:YAG laser (355 nm, 1 ns pulse width, 100 kHz max. rep. rate, Advanced Optical Technology) is used as the excitation source. A multimode fiber with core diameter of 25μm (0.10 NA, HPSC25, Thorlabs) or 50 μm (0.22 NA, FVP050055065, Polymicro Technologies) delivers the excitation light to the handheld box. Inside the handheld box, the excitation light is collimated (L2: f = 11 mm, ARC 350-700 nm, CFC-11X-A, Thorlabs) and scanned by a pair of galvanometer mirrors (5 mm beam aperture, ± 5 mechanical degrees, Cambridge Technology) on the proximal end of the rigid endoscope. The rigid endoscope was built using standard 0.5 inch lens tubes and

consists of three lenses. The first two lenses from the proximal end (L3, L4: f = 30 mm, LB003, Thorlabs) serve as an image relay, while the third lens (L4: Near UV achromat doublet; f = 30 mm, 50 mm or 60 mm; Edmund Optics) works as the objective. In this configuration, the excitation fiber core diameter and the focal length of the objective determine the lateral resolution and the FOV of the system. Finally, a lens tube with length equal to the objective's focal length is added at the distal end, which allows the sample to be placed in contact with the probe. Such a configuration can potentially reduce motion artifact during image acquisition.

4.3 Data Processing

The multispectral FLIM data consisted of three fluorescence decays per pixel (one per emission band). The relatively long excitation pulse width (FWHM: ~1 ns) necessitated the temporal deconvolution of the instrument response from the measured fluorescence decay in order to obtain accurate estimation of the fluorescence lifetime. Time deconvolution was performed offline using an optimized Laguerre expansion technique algorithm [32]. After deconvolution, nine images were generated to quantify the fluorescence emission of the samples: absolute integrated fluorescence intensity, normalized integrated fluorescence intensity, and average lifetime maps for each of the three emission bands. In addition, to demonstrate real-time estimation and visualization of the multispectral FLIM maps, an online deconvolution method was applied.

4.3.1 Fluorescence Lifetime Online Algorithm

To calculate the fluorescence lifetime online, the measured decay for each pixel was compared against a lookup table of decays generated by convolving the instrument response with single exponential decays with time constants ranging from 0.2 to 8 ns (in steps of 0.2 ns). The best match in terms of the minimum means squared error (MSE) was selected and used as the estimation of the fluorescence lifetime, the MSE was calculated as follows:

$$MSE = \frac{1}{N}\sum_{n=0}^{N}(y(n) - \hat{y}(n))^2 \quad \textbf{(8)}$$

where N is the total number of samples, n is the sample time, $y(n)$ is the measured fluorescence decay and $\hat{y}(n)$ is the simulated measured fluorescence decay.

Figure 9 shows an example using 3 possible fIRF's ($\hat{h}(n)$) of 1 ns, 4 ns and 8 ns. The 3 possible fIRF's are convolved with the instrument response to get 3 simulated measured decays ($\hat{y}(n)$). The MSE between each of this 3 exponential decays and the measured fluorescence decay (y(n)) is calculated and the simulated measured decay with the minimum MSE is selected, in this example, the decay with the average lifetime of 1 ns is selected.

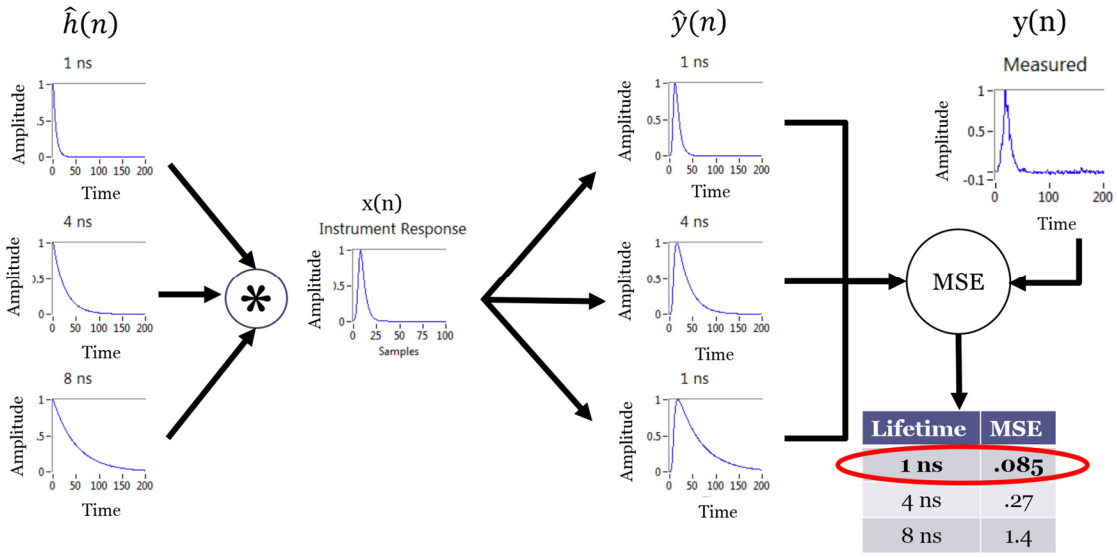

Figure 9. Online algorithm example using 3 single exponential decays: 1 ns, 4 ns and 8 ns.

4.4 Validation

The handheld imaging system was first validated with 1 mM solutions of 1,4-bis (5-phenyloxazol-2-yl) benzene-POPOP (in ethanol), NADH and FAD (in PBS). The standard dye solutions were loaded into three quartz capillary tubes and placed side by side under the probe. A video was recorded at ~1.33 frames per second.

To demonstrate its ability for *in vivo* application in animal models, the handheld system was validated by imaging a normal hamster cheek pouch *in vivo*. The imaging protocol was approved by the Institutional Animal Care and Use Committee at Texas A&M University. During imaging, the hamster was first anesthetized, and a cheek pouch was pulled out and extended, and the rigid probe was gently placed on the mucosal surface.

A video was recorded during the movement of the probe on top of the mucosa tissue at ~1.33 frames per second.

The clinical potential of this system was further demonstrated by imaging a human oral biopsy *ex vivo* and the ventral surface of a human tongue *in vivo*. The respective imaging protocols were approved by the Institutional Review Boards at Texas A&M University and Baylor College of Dentistry. For the *ex vivo* study, the oral tissue biopsy was transported immediately in PBS to the imaging system following excision. A single FLIM image was recorded with the epithelium in contact with the probe. One end of the biopsy was sutured to mark the image orientation to allow comparison with the respective histology section. Finally, the tissue specimen was fixed in 10% formalin and processed for hematoxylin and eosin (H&E) histological analysis. For the *in vivo* study, the ventral tongue region of a human volunteer was imaged. The probe was inserted into the volunteer's month and gently placed on the target location. Only one frame was collected to minimize exposure to UV radiation.

For all the aforementioned experiments, the following working parameters were used. The laser pulse energy at the sample was set at ~1 μJ/pulse, resulting in adequate signal-to-noise ratio (SNR ≥ 30 dB). Since only one pulse is required per pixel, the pixel rate is equal to the laser repetition rate. The laser repetition rate was set at 30 kHz and the total number of pixels per frame was set at 150 × 150, corresponding to an acquisition speed of ~1.33 Hz. The 50 μm excitation fiber and the 50 mm focal objective lens were used, corresponding to a lateral resolution of ~110 μm.

4.5 Results

4.5.1 Capillary Tubes with Fluorophores

For 355 nm excitation wavelength, the emission peaks for POPOP, NADH and FAD are approximately at 390 nm, 450 nm and 540 nm, respectively [8]. The normalized intensity maps (Figure 10) confirmed strong emission of POPOP at both the 390 nm and 452 nm channels, strongest emission of NADH at the 452 nm channel, and emission of FAD only at the >500 nm channel. The average lifetime maps (Figure 10) were also in good agreement with the previously published values for the corresponding fluorophores [8].

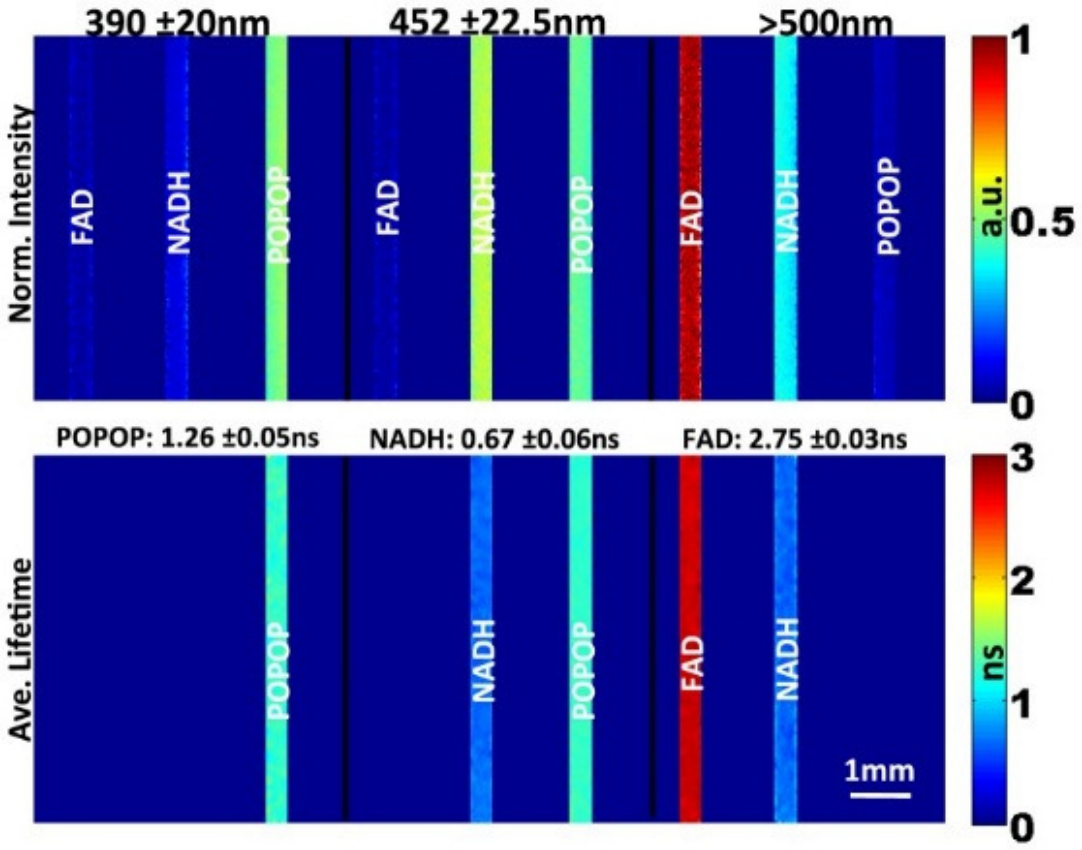

Figure 10. In vitro validation imaging of quartz capillaries loaded with FAD, NADH, and POPOP [40].

The average lifetime values for each fluorophore estimated using the offline and the online methods are compared in Table 2 (calculated pixel-to-pixel for the areas corresponding to the entire capillary).

Table 2. Comparison of offline and online fluorescence lifetime estimations (mean ± standard deviation).

	Offline Estimates (ns)	Online Estimates (ns)
POPOP (390 nm)	1.26 ± 0.07	1.03 ± 0.13
NADH (452 nm)	0.67 ± 0.04	0.32 ± 0.08
FAD (>500 nm)	2.75 ± 0.03	1.91 ± 0.14
Pouch (390 nm)	5.86 ± 0.17	3.91 ± 0.58
Pouch (452 nm)	4.44 ± 0.13	2.36 ± 0.45
Pouch (>500 nm)	3.40 ± 0.19	1.92 ± 0.41

4.5.2 In Vivo Hamster Cheek Pouch

Results from an imaged region are shown in Figure 11. The FLIM maps indicate strong fluorescence intensity at the 390 nm and 452 nm channels (Figure 11(a) and Figure 11(b)), and lifetime values between 4 and 6 ns (Figure 11(c)), reflecting a collagen-dominant autofluorescence expected in normal epithelial tissue. Notice that the vasculature network can be observed in the absolute fluorescence intensity maps, as blood absorption attenuates the fluorescence signal. The normalized intensity and lifetime maps, on the other hand, were insensitive to blood absorption, and indicated spatially uniform spectral and lifetime properties of the autofluorescence emission of normal cheek pouch epithelial tissue. This was expected, since both the layered structure and the relative concentration of endogenous fluorophores (NADH and FAD in the epithelium, and collagen in the underlying stroma) are maintained throughout the normal epithelial tissue. The average lifetime from these two normal cheek pouch regions estimated using either of the methods (offline or online) are compared in Table 2 (calculated pixel-to-pixel for the area corresponding to the entire FOV).

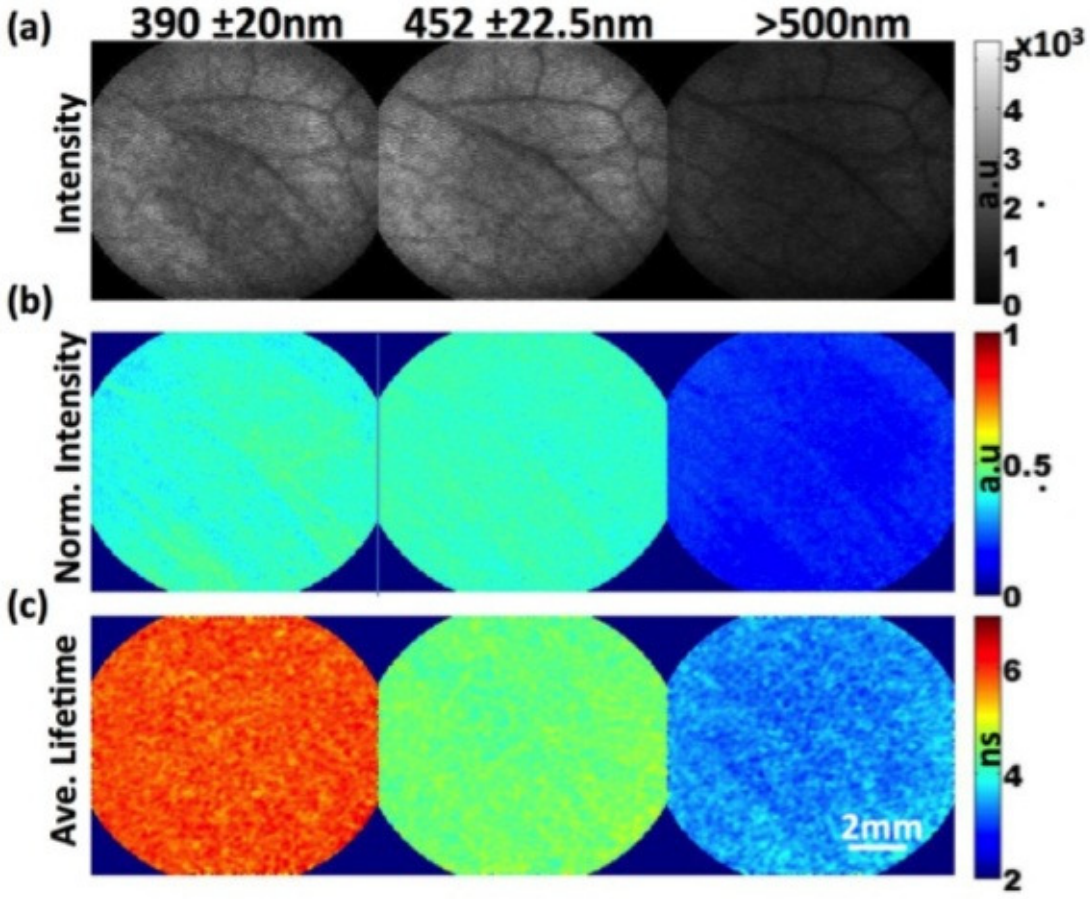

Figure 11. *In vivo* validation imaging of normal hamster cheek pouch. (a) Absolute integrated fluorescence intensity maps. (b) Normalized integrated fluorescence intensity maps. (c) Fluorescence lifetime maps. FOV: 10 x 10 mm^2 [40].

4.5.3 Ex Vivo Human Oral Biopsy

The absolute intensity, normalized intensity and average lifetime maps are shown in Figure 12(a), Figure 12(b), and Figure 12(c), respectively. For the intensity maps, strong emission was observed at the 452 nm channel, followed by comparatively lower fluorescence at the 390 nm and >500 nm channels. For the average lifetime maps, the 452 nm channel showed relative shorter lifetime than 390 nm channel attributed to NADH,

which shows a short lifetime and peak emission at ~450 nm. While most of the FLIM parameters (intensity and lifetime) did not show significant variation across different regions of the biopsy, a small region (marked as Region 1 in Figure 12(c)) in the lifetime map for >500 nm channel showed larger value of lifetime (5.19 ± 0.30 ns) in contrast to rest of the biopsy. This area was later diagnosed as superficial invasive squamous cell carcinoma. The corresponding histology image is shown in Figure 12(d). For comparison, the histology image of a region which represented the rest area of this biopsy (marked as Region 2 in Figure 12(c)) with relatively lower lifetime values (4.03 ± 0.19 ns) was also included and shown in Figure 12(e). This particular region in Figure 12(e) was diagnosed as dysplasia as most of the biopsy. The increase in lifetime in Region 1 can be attributed to porphyrin, the presence of which is known to increase with progression of precancer [41].

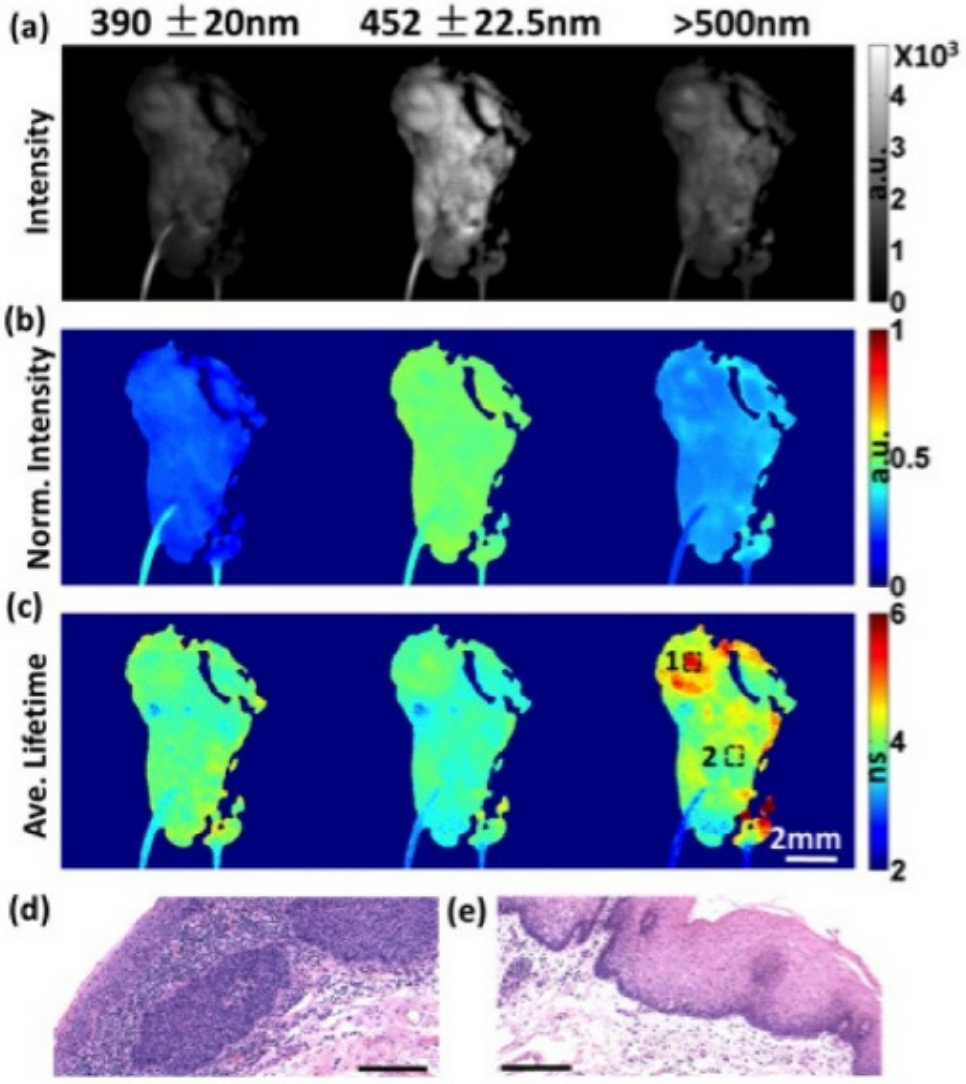

Figure 12. *Ex vivo* human oral biopsy. (a) Absolute integrated fluorescence intensity maps. (b) Normalized integrated fluorescence intensity maps. (c) Fluorescence lifetime maps. FOV: 10 x 10 mm^2. (d) Histology image for the position marked in (c) as Region 1. (e) Histology image for the position marked in (c) as Region 2 [40].

4.5.4 In Vivo Ventral Region of Human Tongue

The absolute intensity, normalized intensity and average lifetime maps are shown in Figure 13. Strong emission was observed in 452 nm channel, followed by comparatively

lower fluorescence at 390 and >500 nm channels. The average lifetime maps showed similar lifetime of 4.04 ± 0.29 ns, 4.22 ± 0.28 ns and 4.19 ± 0.28 ns for 390 nm, 452 nm and >500 nm channels, respectively. Notice also here that spatial contrast was evident in the absolute fluorescence intensity maps, while little contrast was observed in the normalized intensity and lifetime maps, as expected for normal epithelial tissue.

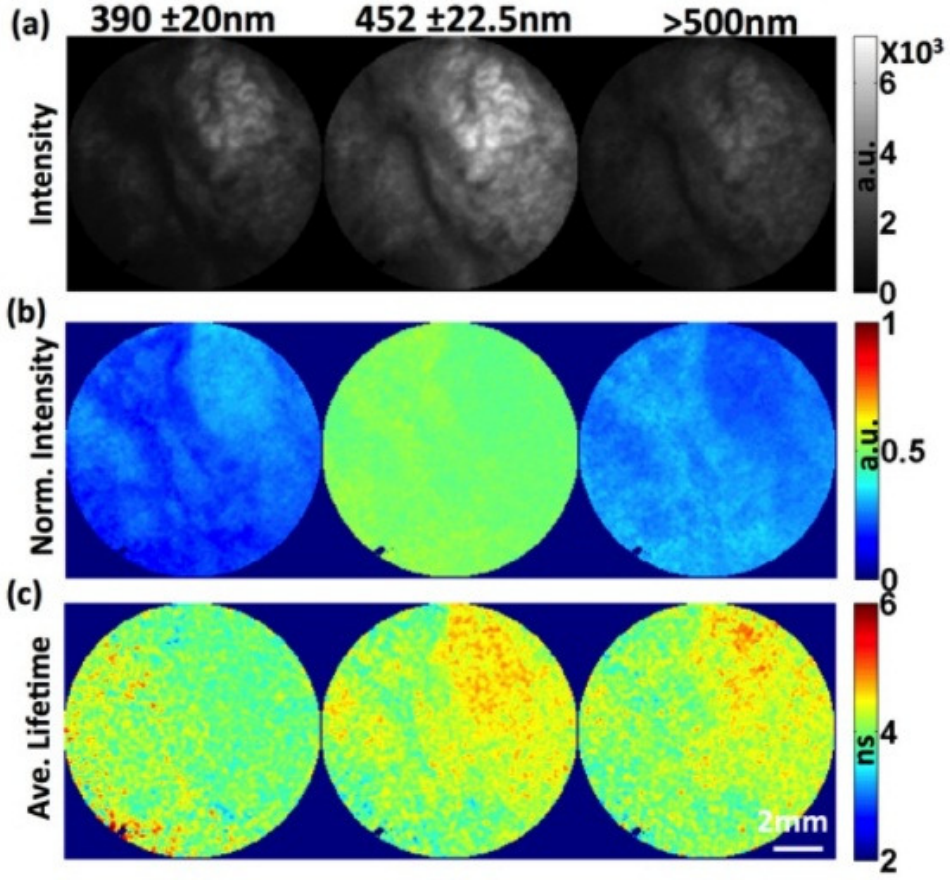

Figure 13. *In vivo* imaging of the ventral tongue from a normal human volunteer. (a) Absolute integrated fluorescence intensity maps. (b) Normalized integrated fluorescence intensity maps. (c) Fluorescence lifetime maps. FOV: 10 x 10 mm^2 [40].

4.6 Discussions and Conclusion

In order to use this system in a clinical setting *in vivo*, the laser energy levels should not exceed the tissue damage threshold which can be estimated in terms of the maximum permissible exposure (MPE) provided by the American National Standards Institute (ANSI) standards for the safe use of lasers [42]. The single pulse limit for a 1 ns pulse at 355 nm is 303 μJ for both eye and skin. Therefore, we are limited by the average irradiance in the limiting aperture (3.5 mm diameter) which was calculated to be 29.8 μJ. For our system, the actual energy deposited is 2.8 μJ, which is an order of magnitude lower than the MPE for both ocular and skin use. We are thus confident that *in vivo* imaging can be performed safely with the proposed handheld FLIM imaging system.

One significant advantage of the proposed multispectral FLIM endoscope design is that, unlike previous implementations, it can achieve relatively high imaging speed without sacrificing temporal resolution. The achieved high temporal resolution allows correcting for the non-ideal instrument response through time deconvolution. In addition, since the entire fluorescence decay is measured directly, the full complexity of its temporal dynamics can be captured and is no longer limited to a single exponential approximation.

Although our imaging systems allows measuring time-resolved fluorescence data with high temporal resolution, accurate estimation of fluorescence lifetimes still requires computationally expensive iterative deconvolution methods. Our fully validated Laguerre deconvolution method is significantly faster than standard nonlinear least square deconvolution algorithms, but it is still not suitable for online processing and visualization of FLIM data [32]. To take advantage of the relative high pixel rate achieved by our system

and to demonstrate real-time FLIM data processing and visualization, the online deconvolution method described above was proposed. An interesting observation was the fact that the online processing and visualization of the multispectral FLIM maps were insensitive to movement. In Table 2, the values of the online lifetime estimations are compared against the offline estimation obtained with the Laguerre deconvolution method. The reported fluorescence lifetime values correspond to the average fluorescence lifetime. If the fluorescence decay follows a single exponential dynamic, the average fluorescence lifetime and the single exponential time constant should have the same value. However, when the measured fluorescence decay follows more complex dynamics, as it is usually the case for endogenous fluorescence measured in our experiments, the corresponding average fluorescence lifetime will be underestimated is the data is treated as a single-exponential decay. As expected, the online values were underestimated with respect to the offline values due to the single exponential approximation. Nevertheless, the online FLIM maps provided fluorescence lifetime contrast similar to that of the offline FLIM maps.

In conclusion, we report the first demonstration of a time-domain multispectral FLIM endoscope that requires only one excitation pulse per pixel; thus, the pixel rate equates to the laser repetition rate. Taking advantage of this relatively high pixel rate, we were able to perform the fastest *in vivo* multispectral FLIM imaging in the human oral cavity reported thus far. Finally, we also report the first demonstration of real-time deconvolution of the instrument response from the fluorescence decay at each pixel of the image, which allowed accurate real-time lifetime map estimation and visualization at

multiple spectral bands simultaneously. This design will facilitate the evaluation of multispectral FLIM for *in vivo* applications, and is currently being explored to image oral cancer, which is our target clinical application.

5. NOVEL BI-EXPONENTIAL DECONVOLUTION FOR REAL-TIME FLIM

5.1 Introduction

As discussed in Section 2.4, in time-domain FLIM, the measured fluorescence decay $y(n)$ is the convolution of the fIRF $h(n)$ and the instrument response $x(n)$:

$$y(n) = h(n) * x(n) \quad \textbf{(2)}$$

In order to estimate the fluorescence lifetime, $h(n)$ must be estimated, and in order to estimate $h(n)$, the instrument response must be deconvolved from the measured fluorescence decay [19, 21]. In order to deconvolve the instrument response, first we need to estimate it. Usually the instrument response is measured by imaging a sample with extremely short lifetime, in this case the instrument response will be very close to the measured fluorescence decay. Another method is to measure the scattered light from the excitation pulsed source. Also, as mentioned in Section 2.4.9, BDE is an algorithm that can estimate de instrument response without measuring directly the instrument response. The right measurement of the instrument response will have a direct impact in the fluorescence lifetime estimation. For our proposed algorithm we only need to know the instrument response and the range of possible fluorescence lifetimes (for instance, between 0.5 and 10 ns). In section 2.4 we reviewed several deconvolution algorithms; however, as it was discussed, none of them are fast enough for real-time FLIM analysis and visualization.

In this section, we described a biexponential model fitting algorithm based on a

lookup table and pattern recognition techniques. Because of its robustness to noise and speed, this method has the potential to estimate fluorescence lifetimes in real-time allowing real-time FLIM application.

5.2 Algorithm

Our novel approach works by comparing the measured fluorescence decay against a database of synthetic fluorescence decays and picking the best match based on a set of features. Figure 14 shows the block diagram of the algorithm. First, a library of fIRF's $\hat{h}(n)$ is generated using a bi-exponential model and convolved with the instrument response $x(n)$. Each of these conlvolved decays $\hat{y}(n)$ is characterized by a feature vector $\varphi(\hat{y})$. Then, these feature vectors, along with the exponential model parameters and the average lifetime are saved in a database. At this point our algorithm is ready to start processing data. Each new measured fluorescence decay $y(n)$ is characterized by the same feature vector $\varphi(y)$ and compared against the feature vectors $\varphi(\hat{y})$ from the database. Finally, based on the selection criteria, the exponential model parameters and the average lifetime of the selected feature vector are extracted from the database. Since these values are calculated directly from the fIRF's there is no need for any deconvolution algorithm.

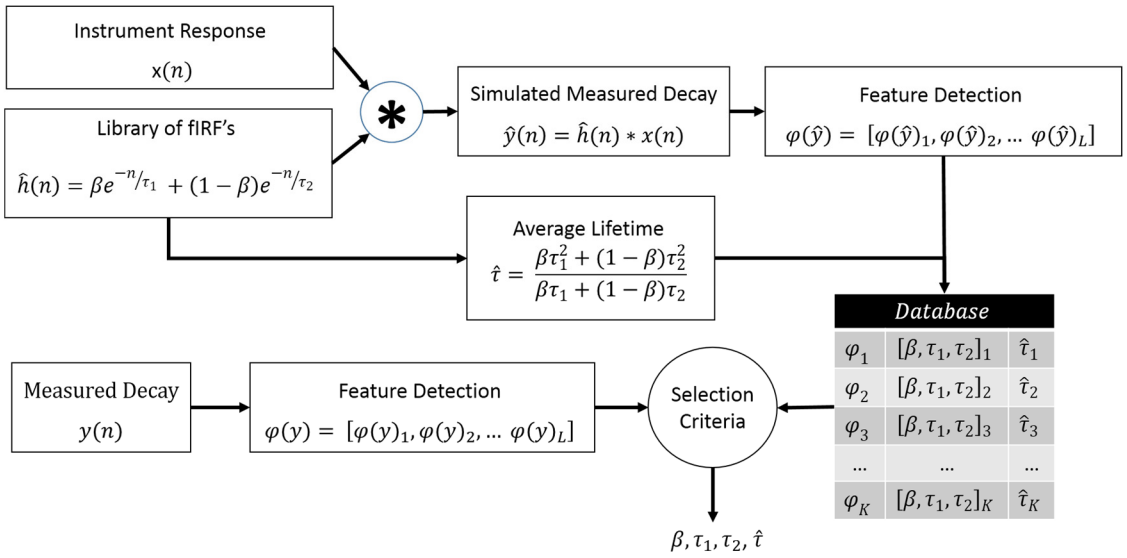

Figure 14. Algorithm diagram concept.

5.2.1 Database of Synthetic Data

To create the database, first we generated the possible fIRF's ($\hat{h}(n)$) using a bi-exponential model:

$$\hat{h}(n) = \beta e^{-n/\tau_1} + (1-\beta)e^{-n/\tau_2} \quad \textbf{(9)}$$

where n is the sample time, β and (1- β) are the relative contributions, and τ_1 and τ_2 are their respective lifetimes. Table 3 show the settings to create the library of fIRF's. In total there are 64,380 different bi-exponential fIRF's.

Table 3. Synthetic exponential decay library parameters settings.

	$\boldsymbol{\beta}$	$\boldsymbol{\tau_1}$ (ns)	$\boldsymbol{\tau_2}$ (ns)
Range	0 – 1	0.125 – 15	0.125 - 15
Resolution	0.1	0.125	0.125

After we had all the possible bi-exponential IRF's, we convolved each of them with the impulse response $x(n)$ to obtain:

$$\hat{y}(n) = \hat{h}(n) * x(n) \tag{10}$$

where $\hat{y}(n)$ is the simulated measured decay. Each of these simulated measured decays was characterized by a feature vector $\varphi(\hat{y})$. These feature vectors, along with the exponential model parameters and the average lifetime were saved in the database. Finally, we sorted the database by one of the features; this feature will be used to select a subset of the database later on.

5.2.2 Features

The feature set is the most important part of our algorithm, they need to be able to distinguish between similar exponential decays and also be robust to noise. Because of the latter characteristic we proposed a set of transformations ϕ_k to the original measured decay $y(n)$ as follows:

$$\phi_1(n) = \frac{1}{N}\sum_{n=0}^{N} y(n)\,; n > 0 \tag{11}$$

$$\phi_2(n) = \frac{1}{N}\sum_{n=0}^{N} n \cdot y(n)\,; n > 0 \quad \textbf{(12)}$$

$$\phi_3(n) = \frac{1}{N}\sum_{n=0}^{N} n \cdot y(n)\,; n > 0 \quad \textbf{(13)}$$

$$\phi_4(n) = \frac{1}{N}\sum_{n=0}^{N} n^3 \cdot y(n)\,; n > 0 \quad \textbf{(14)}$$

$$\phi_5(n) = \frac{1}{N}\sum_{n=0}^{N} \mathrm{y}(n)^2\,; n > 0 \quad \textbf{(15)}$$

where n is the time sample and N is the number of time samples.

To make the features invariant to size we are normalizing the signal and its transformation between 0 and 1. Figure 15 shows two simulated exponential decays of τ = 1 ns and τ = 1.5 ns at 20 dB, as observed it is easier to differentiate them in transformations ϕ_1 and ϕ_2. We can also notice that the transformations are less noisy than the original signal.

Therefore, we end with 6 signals, the original signal ($\phi_0(n) =$ y(n)) and its five transformations. For each signal ($\phi_{\mathrm{k}}(n), \mathrm{k} = 0,1,..,5$), the following 5 features are calculated:

1. 1st Moment defined as:

$$A_k = \sum_{n=0}^{N} n \cdot \phi_{\mathrm{k}}(n) \quad \textbf{(16)}$$

2. 2nd Moment defined as:

$$B_k = \sum_{n=0}^{N} n^2 \cdot \phi_{\mathrm{k}}(n) \quad \textbf{(17)}$$

3. 3rd Moment defined as:

$$C_k = \sum_{n=0}^{N} n^3 \cdot \phi_{\mathrm{k}}(n) \quad \textbf{(18)}$$

4. Area defined as:

$$D_k = \sum_{n=0}^{N} \phi_{\mathrm{k}}(n) \quad \textbf{(19)}$$

5. Square defined as:

$$E_k = \sum_{n=0}^{N} \phi_{\mathrm{k}}(n)^2 \quad \textbf{(20)}$$

In total we have 30 features that the classifier can use to select the best match from the database.

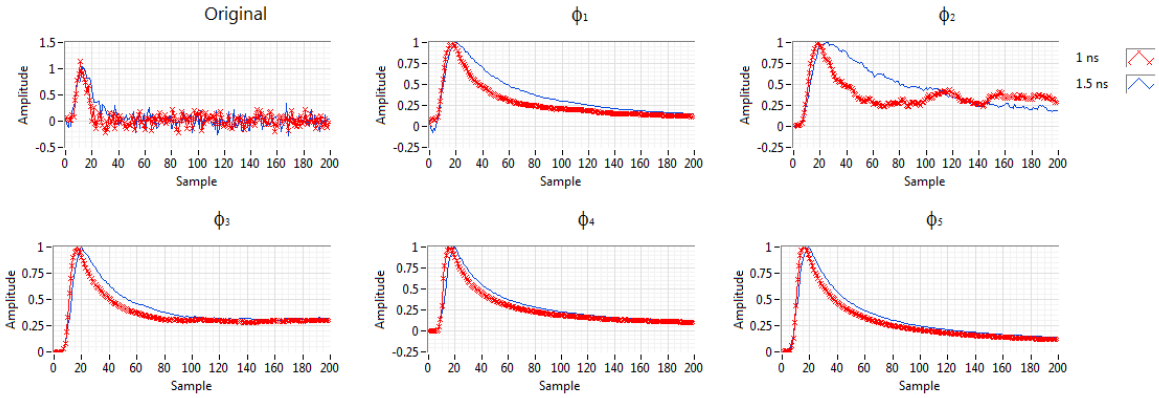

Figure 15. Original and its five normalized transformations of two simulated sampled decay of 1 ns and 1.5 ns at 20 dB.

5.2.3 Classifier

For each simulated measured decay in the database, a feature vector, with the resulting best feature set, will be pre-computed and stored. The same feature vector will also be computed for each pixel measured fluorescence decay. The classifier algorithm used is a minimum distance classifier, in which each simulated measured decay in our database is a class and a new input (a pixel measured fluorescence decay) is assigned to the class that minimizes the squared Euclidian distance between the class and the input feature vectors. The squared Euclidian distance is measured as follows:

$$d^2 = \sum_{i=0}^{L} (\varphi_i(y) - \varphi_i(\hat{y}))^2 \qquad \textbf{(21)}$$

where d is the Euclidian distance, $\varphi(y)$ is the feature vector of the measured decay, $\varphi(\hat{y})$ is the feature vector of the simulated measured decay, and L is the size of the feature vector.

To compensate for different variance between features, we normalized each feature between 0 and 1 as follows:

$$\bar{\varphi}_l = \frac{\varphi_l - \min\limits_{l \in L} \varphi_{k,l}}{\max\limits_{l \in L} \varphi_{k,l} - \min\limits_{l \in L} \varphi_{k,l}} \quad \mathrm{k} = 1, \ldots, 64380 \qquad \textbf{(22)}$$

where $\bar{\varphi}_l$ is the normalized feature *l*, $\min\limits_{l \in L} \varphi_{k,l}$ is the minimum value of feaure *l* from all the simulated measured decays, and $\max\limits_{l \in L} \varphi_{k,l}$ is the maximum value of feature l from all the simulated measured decays.

Since our database has 64,380 different "classes" it´s not feasible to calculate the Euclidean distance between the input and each of the 64,380 classes. Instead, we use a subset of classes; this subset is determined by two parameters: an initial index "k" and a subset of size "α". Figure 16 shows an example of a subset for values of k = 250 and α = 5. The smaller the size the faster our classifier is going to be, but also the higher the risk to misclassify. The initial guess of "k" is going to be based on one of the features. The database is going to be sorted by this particular feature so we can easily find the closest value.

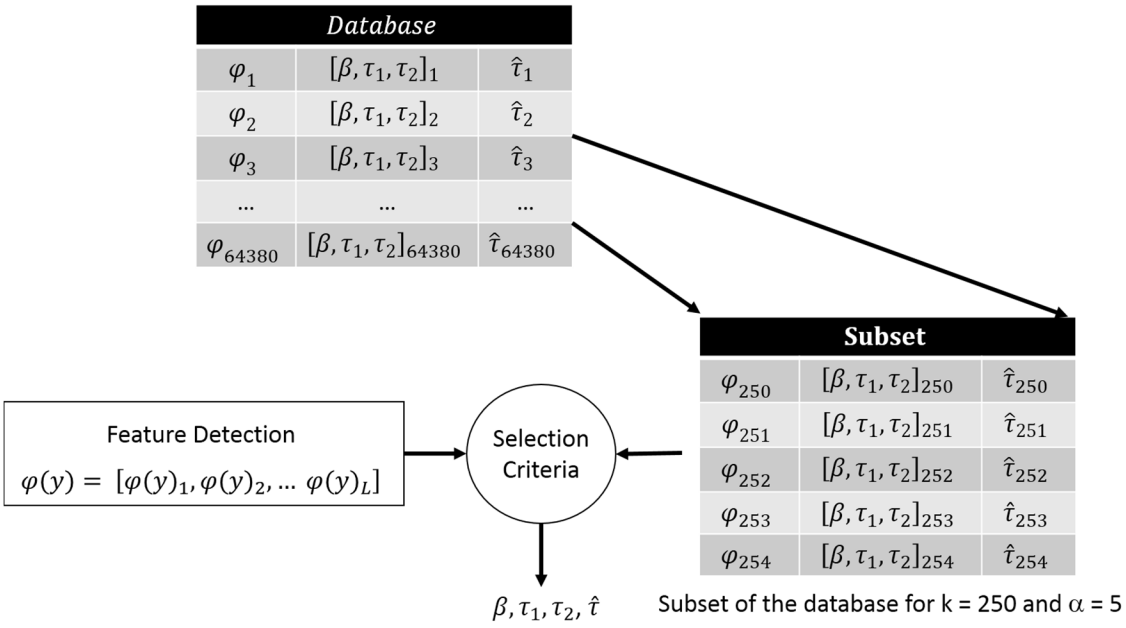

Figure 16. Example of a subset of the database for k = 250 and α = 5.

5.2.4 Feature Selection

From the 30 possible features we need to select a subset of features. It may seem logical that using all the features is the best option, but that's not the case in pattern recognition. Including "bad features," for example, features that are very sensitive to noise, decrease the performance of the classifier. In addition, using too many features increases the processing time and the chances of overfitting.

The method used for feature selection was a Sequential Forward Search (SFS) wrapped around the classifier algorithm. We start the SFS with the best combination of three features and stopped the search when the number of features equals six. The best combination of three features was obtained by exhaustive search. The criterion used to

select the best set of features was the Root Mean Square (RMS) value of the average lifetime error percentage between our algorithm and the non-linear LSIR method. The RMS and error percentage (EP) was calculated as follows:

$$\text{RMS} = \sqrt{\frac{1}{n}\left(EP_1{}^2 + EP_2{}^2 + \cdots + EP_n{}^2\right)} \quad \textbf{(23)}$$

$$\text{EP} = \frac{\hat{\tau}_{LSIR} - \hat{\tau}_{ours}}{\hat{\tau}_{LSIR}} x100 \quad \textbf{(24)}$$

where n is the number of bi-exponential decays in the test, $\hat{\tau}_{LSIR}$ is the estimated lifetime using LSIR and $\hat{\tau}_{ours}$ is the estimated lifetime using our method.

5.3 Validation Methods

Our algorithm was tested using synthetic data and experimental FLIM data from standard fluorescent dyes and human tissue. The performance of our algorithm was compared against the LSIR method and the goodness of fit was evaluated using the Ljung-Box test [43].

5.3.1 Synthetic Data

Synthetic data was generated using the bi-exponential model for the fIRF, with random values of β between 0 and 1, and random values of τ_1 and τ_2 between 0.1 and 10 ns. To simulate measured data, the simulated fIRF's were convolved with a pre-measured instrument response. The instrument response was obtained by imaging Erythrosine B, a

fast decaying dye. Finally Gaussian and Poisson noise contributions were added to yield different SNR levels between 15-40 dB. The resulting synthetic data was normalized against its peak intensity.

5.3.1.1 Comparison against True Lifetime and LSIR

Synthetic data allow us to compare the estimated average lifetime against the "true" average lifetime. To test the performance of our algorithm we compared the results against the LSIR method with a bi-exponential model. The average lifetime of both methods was calculated using equation (25). The error percentage of each method against the "true" average lifetime was calculated using equation (24) and compared.

$$\hat{\tau} = \frac{\beta\tau_1^2 + (1-\beta)\tau_2^2}{\beta\tau_1 + (1-\beta)\tau_2} \quad \textbf{(25)}$$

5.3.2 Experimental Data

Experimental FLIM data acquired with the handheld system described in Section 4 were used for our method validation.

5.3.2.1 Standard Dyes

The algorithm was validated with 1mM solutions of Fluorescein and 9-cyanoanthracene (9-CA) (in ethanol), and nicotinamide adenine dinucleotide (NADH) and

flavine adenine dinucleotide (FAD) (in PBS). The solution were loaded into four quartz capillary tubes and imaged.

5.3.2.2 Tissue Data

The algorithm was validated with existing tissue samples from the system described above. Data were collected from consented patients.

5.3.3 Whiteness of Residual Test

To test the goodness of fit we use the Ljung-Box test. The Ljung-Box test, assesses the randomness of a time series based on its autocorrelation and is defined as:

$$Q_{LB} = n(n+2)\sum_{k=1}^{k=M}\frac{r_k^2}{n-k} \quad \textbf{(26)}$$

where r_k is the autocorrelation at lag k, n is the number of samples, and M is the number of lags being tested. Under the hypothesis that the residual is a random signal, the statistic Q follows a chi-squared distribution with h degrees of freedom ($\chi^2{}_{(h)}$), where h = M – 3, since the bi-exponential model has 3 parameters. The test rejects the hypothesis that the residual is a random signal if:

$$Q_{LB} > \chi^2{}_{1-a,h} \quad \textbf{(27)}$$

where $\chi^2{}_{1-a,h}$ is the a-quantile of the chi-squared distribution with h degrees of freedom. We used M = 20 and a = .05.

5.4 Results

5.4.1 Feature Selection

The feature selection method was implemented using synthetic and experimental data. The synthetic data consisted of 4000 synthetic decays covering the whole lifetime range (0.1-10 ns) with varying SNR levels between 20-30 dB. The experimental data consisted of 3000 random pixel decays from 20 random datasets, which included standard fluorescence dyes (NADH and FAD), tissue from *in vivo* human oral mucosa and tissue form *ex vivo* human coronary arteries. In our first attempt, we tried to identify a single subset of features that would result adequate performance (in terms of the RMS-EP) for the entire range of average lifetimes. Unfortunately, the overall performance was not adequate. We noticed that a specific feature subset that was adequate for a specific range of average lifetimes was not adequate for decays with average lifetimes outside that range. To address this problem, we modified our classification strategy as follows. First, we identified the input measured signal as corresponding to an either 'fast' or 'slow' decay in terms of the value of one of our features: $D_0 = \sum \phi_0(n)$ (the area under the normalized signal). Input measured decays with values of $D_0 < 28$ were considered fast decays, while those with $D_0 > 28$ were identified as slow decays. The threshold of $D_0 = 28$ was empirically selected. Then, we performed a feature selection for each of these two groups of decays. These results are also summarized in Table 4.

Table 4. Feature selection results.

Fast Decays ($D_0 \leq$ **28)**		Slow Decays ($D_0 >$ **28)**	
Number of Features	**RMS-EP**	**Number of Features**	**RMS-EP**
3	17.57%	3	6.78%
4	15.23%	4	6.23%
5	15.19%	5	6.13%
6	15.08%	6	6.08%

These results indicate that four features are sufficient to attain adequate performance for the fast decays ($D_0 \leq$ **28**), while three features were sufficient for the slow decays ($D_0 >$ **28**). The selected features are summarized in Table 5.

Table 5. Selected features for the different groups.

	Fast Decays ($D_0 \leq$ **28)**	Slow Decays ($D_0 >$ **28)**
Features	Feature D_0	Feature A_0
	Feature E_2	Feature A_2
	Feature E_3	Feature B_3
	Feature A_5	-

5.4.2 Parameters for Selecting the Database Region

As indicated before, the search was not performed on the entire database, but a region of it was selected based on a specific feature computed from the input measured decay, in order to accelerate the search speed. The selection of both such feature and the size (α, in terms of number of rows) of the selected database region will define the performance of our algorithm. The feature that resulted on the best performance (smallest

RMS-EP) was FeatureB_5. To select the value of α we plot the performance of our algorithm versus α and the processing time versus α (Figure 17). The speed results show an exponential relationship between α and the pixels per second and the box plots from the error percentage shows a minimal improvement after α = 30 at a SNR level of 40 dB and minimal improvement after α = 20 at a SNR level of 25 dB. Based on these results we selected a value of α = 30.

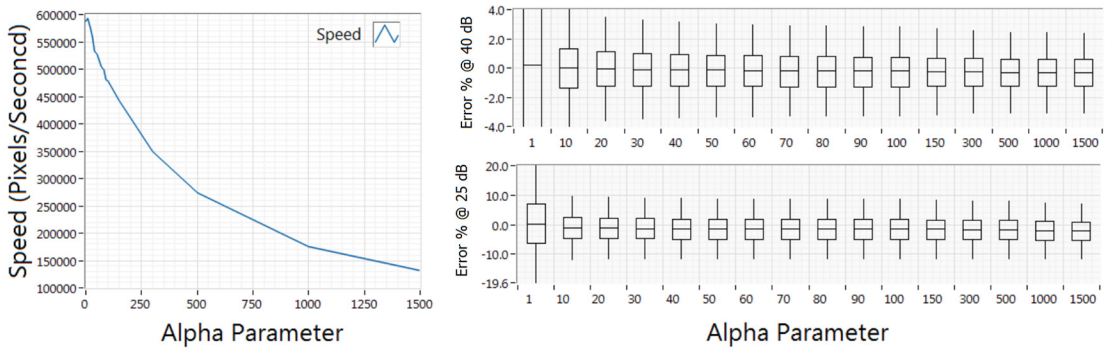

Figure 17. Performance and speed results to select the value of α.

5.4.3 Synthetic Data

5.4.3.1 Lifetime Results

An image map with the 40,000 pixels were created for visual display. Figure 18(a) shows the average lifetime maps at different SNR's. Our method shows a very similar performance than LSIR in the entire range of lifetimes, even at low SNR levels. Figure 18(b), shows the error percentage box plots of each method at 40, 30, 20 and 15 dB SNR. Our method shows an overestimation of the average lifetime values at low SNR. This is

expected since our features are summations of the measured decay and its transformation, and, since the expected value of Poisson noise is always positive, the values of the features are overestimated.

5.4.3.2 Goodness of Fit Results

The same 40,000 pixels were used to compute the Ljung-Box test. Figure 18(c) shows the passing percentage of the Ljung-Box test. The passing percentage indicates the percentage of pixels that their fitting residuals are considered a random signal based on the Ljung-Box test. Our method got similar results than LSIR between 40 and 20 dB SNR. Even at 15 dB our method have good results with almost 85% of passing rate.

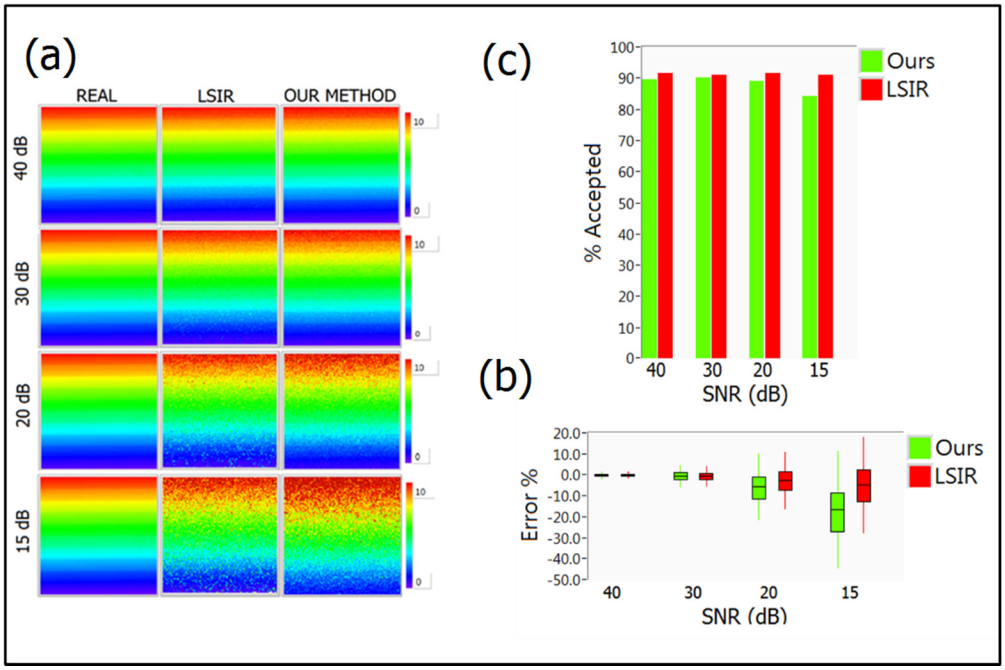

Figure 18. Synthetic data results. (a) Lifetime maps at different SNRs. (b) Distribution of relative error in average lifetime values at different SNRs. (c) Ljung-Box test results at different SNRs.

5.4.4 Experimental Data

5.4.4.1 Standard Dyes Results

The four capillaries were imaged with our system and the lifetime maps of both methods are shown it Figure 19(a). Figure 19(b) shows the lifetime histogram of both methods. We can see from these two figures that the values are similar.

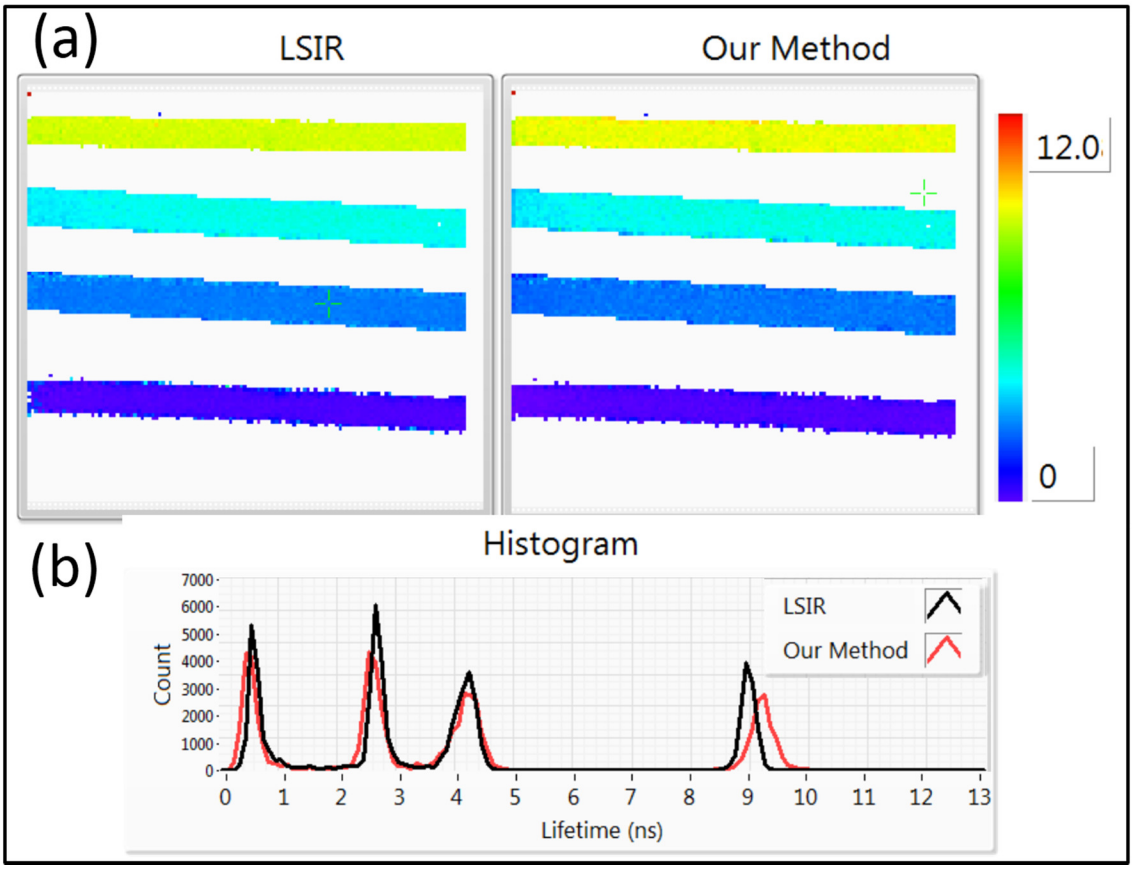

Figure 19. Standard dyes results. (a) Lifetime maps. Color scale in nanoseconds. (b) Lifetime histogram.

Table 6 compare these values with the ones reported by other groups for the same fluorescence dyes.

Table 6. Lifetime results from fluorescence standard dyes. Values are shown as (mean ±SD).

Dye	Our Method	LSIR	Literature
9-CA	9.27 ± 0.63 ns	8.99 ± 0.57 ns	10.3 – 12.28 ns
FAD	2.64 ± 0.29 ns	2.72 ± 0.26 ns	2.3 – 2.85 ns
NADH	0.56 ± 0.17 ns	0.67 ± 0.31 ns	0.3 – 0.5 ns
Fluorescein	4.25 ± 0.21 ns	4.23 ± 0.16 ns	4.0 – 4.2 ns

5.4.4.2 Tissue Data Results

Human oral mucosa from a consented patient was imaged *in vivo* and the lifetime maps of both methods are shown in Figure 20(a). Figure 20(b) shows the lifetime histogram of both methods. The results are consistent with the ones from the dyes experiment, the lifetime values of both methods are very similar. Figure 19(c), Figure 19(e) and Figure 19 (g) shows the maps of the bi-exponential model parameters β, τ_1 and τ_2 correspondently, and Figure 19(d), Figure 19(f) and Figure 19(h) shows their correspondent histograms. As we can see even the individual bi-exponential parameters are similar between both methods, the biggest difference happens on the β parameter and this was expected since we have a poor resolution of 0.1 for this parameter in our method.

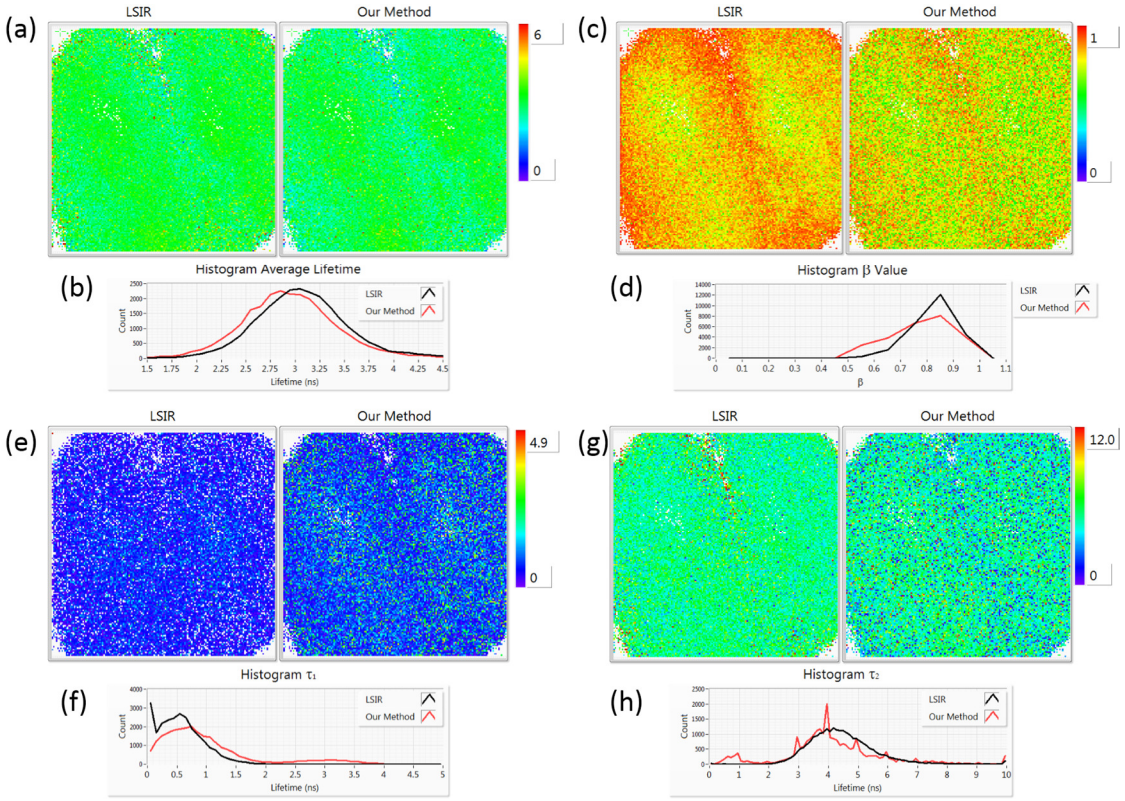

Figure 20. Human oral mucosa results. (a) Average lifetime maps. (b) Average lifetime histogram. (c) β value maps. (d) β value histogram. (e) τ_1 maps. (f) τ_1 histogram. (g) τ_2 maps. (h) τ_2 histogram.

5.4.5 Speed

The most important characteristic of our algorithm is the reduction in computational time to estimate the deconvolved fIRF. We measured the speed of the algorithms by averaging the time to estimate 100,000 decays. Table 7, shows the speed in pixels per second of both methods. As we can see, an improvement of more than 600 times in speed compared to the LSIR method was achieved. To validate that the algorithm is able to estimate the average lifetime in real-time, we are presenting two videos (see

additional material). In the first video, showing 2 fluorescence dyes (FAD and Fluorescein) loaded into capillary tubes being imaged at 4 frames per second, it can be noticed from the histogram that there are no motion artifacts. In the second video, showing a fingerprint being imaged at 1 frames per second, no motion artifacts is noticed and it further demonstrates that our algorithm not only works for single exponential decays.

Table 7. Speed results for both methods.
***Computer: Processor i7-5820K (6 Cores @ 3.3 GHz) and 60 GB RAM.**

Method	Speed (Pixels/Second)*
LSIR	908
Our Algorithm	552,334

5.5 Discussions and Conclusions

We have proposed a fast bi-exponential deconvolution algorithm for real time FLIM data processing. This algorithm selects the best match for the measured fluorescence decay from a database of simulated decays with known bi-exponential parameters. Since the database is built by convolving the instrument response with a family of bi-exponential decays covering a predefined range of lifetimes, deconvolution is no longer required to estimate the fIRF and calculate the average lifetime.

A set of transformations were applied to the measured signal to improve the differentiation between close lifetime values and also to reduce the noise. The features used in this algorithm are fast to calculate, and showed that they are also robust to noise and able to differentiate between similar lifetime values and ranges.

The algorithm described in this paper was successfully validated with both, synthetic and experimental data, proving that it can fit bi-exponential decays and showing similar results and performance than the nonlinear LSIR method.

In terms of accuracy our method was similar to the true lifetime values for the synthetic data tests even at average lifetime values of less than 1 ns, at different SNR, proving that our method is deconvolving the instrument response from the measured decay. Our method showed some overestimation at high levels of noise and this was expected since our features are summations of the measured decay and its transformation, and the expected value of Poisson noise is always positive. As a result of this, our features calculate higher values, similar to the ones of slower decays.

One of our goals with this method was to be able to calculate the average lifetime in real-time and our method showed an increase in speed of more than 600 times compared to the LSIR method. Moreover, it showed a processing speed of 500,000 pixels per second which is faster than the laser repetition rate of the lasers used for pulse sampling FLIM.

FLIM has been also explored for non-destructive tissue characterization and tissue classification, analyzing the fluorescence decay and extracting a set of features (such as the fluorescence intensity, average fluorescence lifetime or the Laguerre coefficients). We believe that the features used in our proposed algorithm can be also utilized for tissue characterization and tissue classification.

In summary, we have developed a fast and accurate bi-exponential algorithm for real-time processing of time-domain FLIM data, which will facilitate practical applications of FLIM, including clinical diagnosis. Furthermore, since this is a general

bi-exponential fitting algorithm, it can be also used in a different variety of applications, including flow cytometry [44, 45], magnetic resonance imaging [46], fluorescence resonance energy transfer [47], among others.

6. FLIM BASED DETECTION OF PRE-CANCEROUS AND CANCEROUS LESIONS FROM BENIGN ORAL LESIONS

6.1 Introduction

Despite of the ease accessibility of the oral cavity, the majority of oral cancers are diagnosed at advantage stages, when the cancer has already metastasized to other locations, most commonly to the lymph nodes of the neck [11]. There are several factors that contribute to the low rate of early detection of oral cancer. One reason is that early stage oral cancer lesions are frequently asymptomatic and therefore unnoticed by the patient. Another reason is that premalignant and malignant oral lesions are very difficult to distinguish from most common benign lesions during clinical visual examination, even for the most experienced health providers. Finally, sampling error during biopsy procedures is also common, particularly in large and diffuse lesions in which the decision on where to take the tissue biopsy is made often randomly. As mentioned in Section 1.3, CADSS systems have emerge to help physicians in their clinical diagnosis by providing them additional information about the lesions. CADSS systems have been used to detect other types of pathologies, including breast cancer [48-50], acute stroke care [51], gastrointestinal lesions [52] and melanoma [53].

Progression of oral cancer is accompanied by alterations in the intrinsic fluorescence properties of the oral tissue as a consequence of changes in the relative abundance of tissue endogenous fluorophores, specifically collagen, nicotinamide adenine dinucleotide (NADH) and flavine adenine dinucleotide (FAD) [54-57]. These changes occur due to difference in metabolism between healthy and malignant cells, as well as to

degradation of stromal collagen. The ability of FLIM to detect biochemical changes makes it suitable for the diagnosis of oral cancer. In Sections 3, a combined FLIM-RCM system was presented. This system was used on a hamster cheek pouch model of oral carcinogenesis to differentiate between dysplastic and normal tissue. In Section 4, a handheld probe FLIM system was used in a clinical study of human oral tissue *ex vivo* and *in vivo*. In this Section the handheld probe from Section 4 was used in an *in vivo* human study aiming to demonstrate the ability to differentiate between precancer and cancer from benign oral lesions.

The *in vivo* human data collected with the FLIM system was separated into benign and malignant lesions based on the histopathological diagnosis. The objective of this study was to use the FLIM data for each patient to design a classifier that can help the differentiation between benign and malignant lesions. Several characteristics or features from the FLIM data were evaluated to perform the classification task. The performance of these features was compared based on the sensitivity and specificity of the correspondent classifier.

6.2 Methods

6.2.1 Subjects

The imaging protocols were approved by the Institutional Review Boards at Texas A&M University and Texas A&M University College of Dentistry. Patients undergoing tissue biopsy examination of suspicious premalignant and malignant oral lesions were recruited. Written informed consent was obtained from all patients recruited. A total of 80

patients were recruited to this study. In 38 of these patients, either FLIM images were not collected (due to the anatomical location of the lesion and/or technical issues with the FLIM endoscopic system) or the quality of the FLIM images was too poor for further processing, see Table 8. It is worth mentioning that the last 9 patients has been successfully imaged. Therefore, the FLIM data from only 42 patients were used. The distribution of imaged oral lesions based on their anatomical location and histopathological diagnosis is provided in Table 9.

Table 8. Distribution of unsuccesful imaging per reason.

Reason	Anatomical Location	Technical Issues	Poor Quality	Total
Number of Patients	9	10	19	38

Table 9. Number of patients per location and diagnosis.

	Benign	**Mild Dysplasia**	**SCC**	**Total**
Tongue	8	5	5	18
Gingiva	9	0	5	14
Oral Mucosa	8	0	2	10
Total	25	5	12	42

6.2.2 Imaging

FLIM data were acquired using the multispectral handheld probe from Section 4. The target oral lesion was first imaged by placing the probe at the center of the lesion. Then, an additional image from a visually healthy region on the contralateral side of the

lesion was also acquired. Therefore, for each patient, a pair of FLIM images was collected (lesion site, contralateral healthy looking site). The multispectral FLIM data consisted of three fluorescence decays per pixel (one per emission band), with 160 x 160 pixels per scan over a FOV of 10 x 10 mm^2.

6.2.3 Histology and Pathological Evaluation

After *in vivo* imaging, a biopsy was taken from the target oral lesion. After surgical excision, the tissue samples were placed in 10% buffered formalin and processed routinely for histopathological evaluation using standard hematoxylin and eosin (H&E) staining. The histological sections were reviewed by two oral pathologists (Drs. Wright and Cheng, TAMU College of Dentistry), and each lesion was diagnosed in one of the following categories: benign, dysplasia, or squamous cell carcinoma (SCC).

6.2.4 Image Preprocessing

The FLIM data was preprocessed as follows before further analysis for tissue classification. Pixels with either a low SNR (less than 25 dB) or saturated intensities were masked and not including in subsequent analysis. A 4 x 4 spatial median filter was applied to improve the SNR of the time-resolved FLIM data. Finally, the integrated intensities for each channel were calibrated to compensate for the different overall spectral response of the emission spectral channels.

6.2.5 Feature Extraction

For each decay (per emission spectral band and per pixel), the following features were extracted: features used during the bi-exponential deconvolution algorithm, average lifetime, highest component of the bi-exponential model, normalized peak intensity and normalized integrated intensity. In addition, the ratios between the peak and integrated intensities per emission band were also included as features. In total 42 features per pixel were extracted. In addition, the FLIM image collected at the contralateral healthy looking side was also used to provide relative values of the previous 42 features, as follows. First, the median pixel value of the feature from the contralateral FLIM image was computed as the reference feature value. Then, this reference feature value was subtracted to each of the corresponding feature pixel values of the lesion image, resulting in 42 relative features. Therefore, a total of 84 features were extracted per pixel. Table 10 summarizes all these features extracted from the FLIM data. The following is a detailed definition of these different features.

6.2.5.1 Bi-exponential Deconvolution Algorithm Features

The bi-exponential deconvolution algorithm described in Section 5 was used to obtain the fIRF. The 8 features used to calculate the fIRF, were used as features of the classifier algorithm, see Table 11.

Table 10. Table showing all the features used for the feature selection step.

#	Description	Ch	Feature ID	#	Description	Ch	Feature ID
1	Feature D_0 described in Section 5.2.2	1	Alg_1_1	43	Alg_1_1 minus reference	1	Alg_1_1_Ref
2	Feature A_0 described in Section 5.2.2	1	Alg_2_1	44	Alg_2_1 minus reference	1	Alg_2_1_Ref
3	Feature A_2 described in Section 5.2.2	1	Alg_3_1	45	Alg_3_1 minus reference	1	Alg_3_1_Ref
4	Feature E_2 described in Section 5.2.2	1	Alg_4_1	46	Alg_4_1 minus reference	1	Alg_4_1_Ref
5	Feature B_3 described in Section 5.2.2	1	Alg_5_1	47	Alg_5_1 minus reference	1	Alg_5_1_Ref
6	Feature E_3 described in Section 5.2.2	1	Alg_6_1	48	Alg_6_1 minus reference	1	Alg_6_1_Ref
7	Feature B_5 described in Section 5.2.2	1	Alg_7_1	49	Alg_7_1 minus reference	1	Alg_7_1_Ref
8	Feature A_5 described in Section 5.2.2	1	Alg_8_1	50	Alg_8_1 minus reference	1	Alg_8_1_Ref
9	Average Lifetime	1	Avg_Lif_1	51	Avg_Lif_1 minus reference	1	Avg_Lif_1_Ref
10	Highest Component	1	Hst_Lif_1	52	Hst_Lif_1 minus reference	1	Hst_Lif_1_Ref
11	Feature D_0 described in Section 5.2.2	2	Alg_1_2	53	Alg_1_2 minus reference	2	Alg_1_2_Ref
12	Feature A_0 described in Section 5.2.2	2	Alg_2_2	54	Alg_2_2 minus reference	2	Alg_2_2_Ref
13	Feature A_2 described in Section 5.2.2	2	Alg_3_2	55	Alg_3_2 minus reference	2	Alg_3_2_Ref
14	Feature E_2 described in Section 5.2.2	2	Alg_4_2	56	Alg_4_2 minus reference	2	Alg_4_2_Ref
15	Feature B_3 described in Section 5.2.2	2	Alg_5_2	57	Alg_5_2 minus reference	2	Alg_5_2_Ref
16	Feature E_3 described in Section 5.2.2	2	Alg_6_2	58	Alg_6_2 minus reference	2	Alg_6_2_Ref
17	Feature B_5 described in Section 5.2.2	2	Alg_7_2	59	Alg_7_2 minus reference	2	Alg_7_2_Ref
18	Feature A_5 described in Section 5.2.2	2	Alg_8_2	60	Alg_8_2 minus reference	2	Alg_8_2_Ref
19	Average Lifetime	2	Avg_Lif_2	61	Avg_Lif_2 minus reference	2	Avg_Lif_2_Ref
20	Highest Component	2	Hst_Lif_2	62	Hst_Lif_2 minus reference	2	Hst_Lif_2_Ref
21	Feature D_0 described in Section 5.2.2	3	Alg_1_3	63	Alg_1_3 minus reference	3	Alg_1_3_Ref
22	Feature A_0 described in Section 5.2.2	3	Alg_2_3	64	Alg_2_3 minus reference	3	Alg_2_3_Ref
23	Feature A_2 described in Section 5.2.2	3	Alg_3_3	65	Alg_3_3 minus reference	3	Alg_3_3_Ref
24	Feature E_2 described in Section 5.2.2	3	Alg_4_3	66	Alg_4_3 minus reference	3	Alg_4_3_Ref
25	Feature B_3 described in Section 5.2.2	3	Alg_5_3	67	Alg_5_3 minus reference	3	Alg_5_3_Ref
26	Feature E_3 described in Section 5.2.2	3	Alg_6_3	68	Alg_6_3 minus reference	3	Alg_6_3_Ref
27	Feature B_5 described in Section 5.2.2	3	Alg_7_3	69	Alg_7_3 minus reference	3	Alg_7_3_Ref
28	Feature A_5 described in Section 5.2.2	3	Alg_8_3	70	Alg_8_3 minus reference	3	Alg_8_3_Ref
29	Average Lifetime	3	Avg_Lif_3	71	Avg_Lif_3 minus reference	3	Avg_Lif_3_Ref
30	Highest Component	3	Hst_Lif_3	72	Hst_Lif_3 minus reference	3	Hst_Lif_3_Ref
31	Normalized Peak Intensity	1	N_Peak_Int_1	73	N_Peak_Int_1 minus reference	1	N_Peak_Int_1_Ref
32	Normalized Peak Intensity	2	N_Peak_Int_2	74	N_Peak_Int_2 minus reference	2	N_Peak_Int_2_Ref
33	Normalized Peak Intensity	3	N_Peak_Int_3	75	N_Peak_Int_3 minus reference	3	N_Peak_Int_3_Ref
34	Normalized Integrated Intensity	1	N_Integrated_Int_1	76	N_Integrated_Int_1 minus reference	1	N_Integrated_Int_1_Ref
35	Normalized Integrated Intensity	2	N_Integrated_Int_2	77	N_Integrated_Int_2 minus reference	2	N_Integrated_Int_2_Ref
36	Normalized Integrated Intensity	3	N_Integrated_Int_3	78	N_Integrated_Int_3 minus reference	3	N_Integrated_Int_3_Ref
37	N_Peak_Int_1 / N_Peak_Int_2	-	R_Peak_1_2	79	R_Peak_1_2 minus reference	-	R_Peak_1_2_Ref
38	N_Peak_Int_1 / N_Peak_Int_3	-	R_Peak_1_3	80	R_Peak_1_3 minus reference	-	R_Peak_1_3_Ref
39	N_Peak_Int_2 / N_Peak_Int_3	-	R_Peak_2_3	81	R_Peak_2_3 minus reference	-	R_Peak_2_3_Ref
40	Integrated_Int_1 / Integrated_Int_2	-	R_Integrated_1_2	82	R_Integrated_1_2 minus reference	-	R_Integrated_1_2_Ref
41	Integrated_Int_1 / Integrated_Int_3	-	R_Integrated_1_3	83	R_Integrated_1_3 minus reference	-	R_Integrated_1_3_Ref
42	Integrated_Int_2 / Integrated_Int_3	-	R_Integrated_2_3	84	R_Integrated_2_3 minus reference	-	R_Integrated_2_3_Ref

Table 11. Features used from the bi-exponential deconvolution algorithm.

Features Used	
Feature D_0	Feature A_0
Feature E_2	Feature A_2
Feature E_3	Feature B_3
Feature A_5	Feature B_5

6.2.5.2 Average Lifetime

The average lifetime feature is calculated as:

$$\tau = \frac{\sum_{n=0}^{N} nh(n)}{\sum_{n=0}^{N} h(n)} \quad \textbf{(28)}$$

where h(n) is the fIRF.

6.2.5.3 Highest Component

The highest component feature is the lifetime with the highest weight of the bi-exponential model obtained by the bi-exponential deconvolution algorithm and is calculated as:

$$Highest\ Component = \begin{cases} \tau_1, & \beta \geq 0.5 \\ \tau_2, & otherwise \end{cases} \quad \textbf{(29)}$$

where τ_1, τ_2 and β are the parameters of the bi-exponential model.

6.2.5.4 Normalized Peak Intensity

The normalized peak intensity feature is calculated for each channel as:

$$I_{norm\_peak\_i} = \frac{\mathrm{I_{peak\_i}}}{\mathrm{I_{peak\_1}} + \mathrm{I_{peak\_2}} + \mathrm{I_{peak\_3}}} \quad \textbf{(30)}$$

$$I_{peak\_i} = max\, h_i(n) \quad \textbf{(31)}$$

where $I_{norm\_peak\_i}$ is the normalized intensity of channel *i*, I_{peak_i} is the peak intensity of channel *i* and $h_i(n)$ is the fIRF of channel *i*.

6.2.5.5 Normalized Integrated Intensity

The normalized integrated intensity feature is calculated for each channel as:

$$I_{norm\_integrated\_i} = \frac{\mathrm{I_{integrated\_i}}}{\mathrm{I_{integrated\_1}} + \mathrm{I_{integrated\_2}} + \mathrm{I_{integrated\_3}}} \quad \textbf{(32)}$$

$$I_{integraetd\_i} = \sum_{n=0}^{N} h_i(n) \quad \textbf{(33)}$$

where $I_{norm\_integrated\_i}$ is the normalized integrated intensity of channel *i*, $I_{integraetd\_i}$ is the integrated intensity of channel *i* and $h_i(n)$ is the fIRF of channel *i*.

6.2.6 Feature Selection

The number of features is critical to the success of a classifier. Too many features can lead to overfitting and poor performance in data independent to the training data. Noisy features or irrelevant features can also decrease the classification performance and increase the computational load. To select only relevant features and reduce the feature

space dimensions, feature selection algorithms could be applied. Feature selection algorithms can be generally divided into wrapper and filter algorithms. Wrapper algorithms utilize the classifier algorithm to score the feature subsets based on the classifier performance. Filter algorithms select subsets of features independently of the classifier. The following wrapper algorithm was adopted and applied in our data, in which feature subsets were selected based on the highest leave-one-out classification performance. First, an exhaustive search of all possible combinations of 3 features was performed. The best 80 3-feature combinations were selected, and a sequential forward search was used, in which features are progressively added. At each iteration, the best 80 combinations were kept. Following this feature selection strategy, the best feature vector of sizes 3, 4, 5 and 6 were identified.

6.2.7 Classifier Algorithm

As mentioned in Section 1.3, a QDA algorithm was used to classify each pixel in one of two categories: 1) benign (B), 2) dysplasia (Dys) or SCC (Dys/SCC). In QDA, the class-conditional probability densities are assumed to me multivariate normal distributions having different mean vectors and different covariance matrices. QDA has been used to differentiate different types of cancer like prostate cancer [58, 59], breast cancer [60, 61], and ovarian and fallopian tube cancer [62].

6.2.8 Validation

Validating a classifier involves testing it on a set of samples that are independent of the training set. This can be done by dividing the dataset into a training set and a validation set. When the dataset is small, it is recommended to use all the dataset for training [63, 64]; however, the classifier cannot be validated using the same data that were used to train the classifier. One approach to overcome this problem is to apply leave-one-out cross-validation (LOOCV) strategies. In this approach, one sample is removed from the training set and used as the test set. This process is repeated for each member of the available dataset. This gives us the advantage of testing with a part of the data that has not been involved in the training, hence it can be considered as being independent, and at the same time using, eventually, all the data both for training and testing [63].

The QDA classifier was trained to classify each pixel of the entire FLIM image as either B or Dys/SCC. However, the LOOCV was applied by excluding a whole entire lesion FLIM data of the training set at every iteration in order to minimize sharing pixels from the same lesion between the training and validation set. Since each lesion corresponds to one independent patient, we named this strategy as Leave-OnePatient-Out cross-validation (LOOPCV). Once all pixels of the testing lesion image had been classified, the entire lesion was classified as Dys/SCC if 25% or more pixels were classified as Dys/SCC; otherwise, the entire lesion was classified as benign. The threshold (25%) for the percentage of Dys/SCC classified pixels was determined by means of giving more importance to malignant pixels and minimize the case of false negatives.

Sensitivity of a classifier is the proportion of patients with disease who test positive (true positive rate). Specificity of a classifier is the proportion of patients without a disease who test negative (true negative rate). The classifier performance was evaluated by computing the sensitivity and specificity for classifying Dys/SCC lesions by pooling the results of all the cross-validation folds.

6.3 Results

As indicated before, a binary classification algorithm was developed to distinguish Dys/SCC from Benign lesions. The following four binary classification problems were solved and their LOOPCV performance quantified:

1) Classification of ALL lesions regardless of their anatomical locations.
2) Classification of all lesions of the tongue.
3) Classification of all lesions of the gingiva.
4) Classification of all lesions of the mucosa.

6.3.1 All Lesions Classification Results

Four different classifiers were trained, each one with either 3, 4, 5 or 6 features. The best features selected for each classifier are summarized in Table 12, and their corresponding LOOPCV confusion matrixes are shown in Table 13. The sensitivity and specificity values of each classifier are shown in Table 14. The pixel classification maps and the percentage of Dys/SCC pixels per image are shown in Figure 21, Figure 22, Figure 23 and Figure 24. As we can see from Table 14, the classification performance increased

with the number of features. The maximum sensitivity of 88% is reached with 6 features and adding one more feature didn't improve the performance (result not shown).

Table 12. Table showing the best subsets for the 4 classifiers using the datasets of all lesions.

	3 Features		4 Features		5 Features		6 Features	
	#	Feature ID	#	Feature ID	#	Feature ID	#	Feature ID
Features	31	N_Peak_Int_1	32	N_Peak_Int_2	4	Alg_4_1	4	Alg_4_1
	37	R_Peak_1_2	37	Ratio_Peak_1_2	33	N_Peak_Int_3	33	N_Peak_Int_3
	45	Alg_3_1_Ref	74	N_Peak_Int_2_Ref	46	Alg_4_1_Ref	37	R_Peak_1_2
	-		84	R_Integrated_2_3_Ref	60	Alg_8_2_Ref	46	Alg_4_1_Ref
	-		-		80	R_Peak_1_3_Ref	60	Alg_8_2_Ref
	-		-		-		80	R_Peak_1_3_Ref

Table 13. Confusion matrixes for the 4 classifiers using the datasets of all lesions.

3 Features

		Predicted	
		Positive	Negative
Observed	Positive	9	8
	Negative	1	24

4 Features

		Predicted	
		Positive	Negative
Observed	Positive	12	5
	Negative	0	25

5 Features

		Predicted	
		Positive	Negative
Observed	Positive	14	3
	Negative	0	25

6 Features

		Predicted	
		Positive	Negative
Observed	Positive	15	2
	Negative	0	25

Table 14. Sensitivity and specificity of detecting Dys/SCC lesions for the 4 classifiers using the datasets of all lesions.

	Sensitivity			Specificity		
		95% Confidence Interval			95% Confidence Interval	
Subset	Estimated Value	Lower Limit	Upper Limit	Estimated Value	Lower Limit	Upper Limit
3 Features	0.53	0.29	0.76	0.96	0.77	0.99
4 Features	0.70	0.44	0.88	1	0.83	1
5 Features	0.82	0.55	0.95	1	0.83	1
6 Features	0.88	0.62	0.97	1	0.83	1

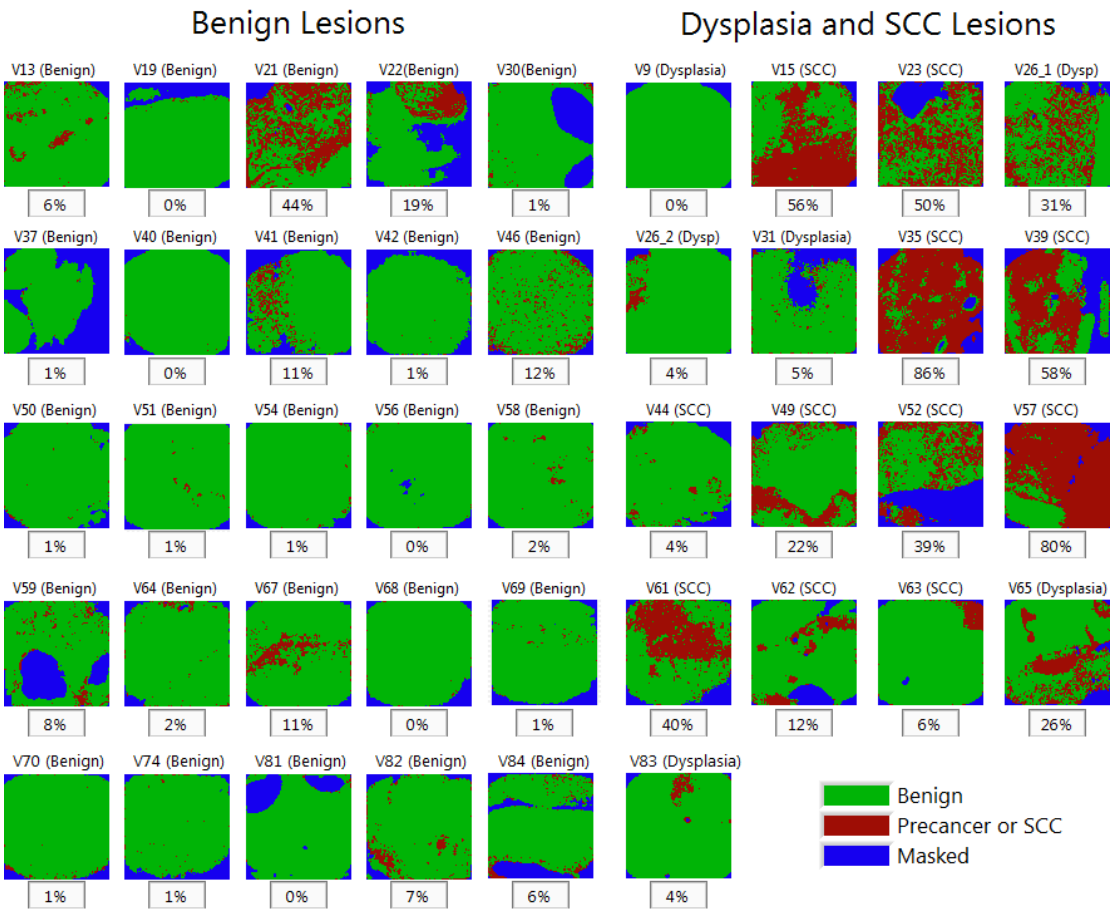

Figure 21. Pixels classification map using 3 features using the datasets of all lesions. Percentage under each image is the percentage of malignant pixels.

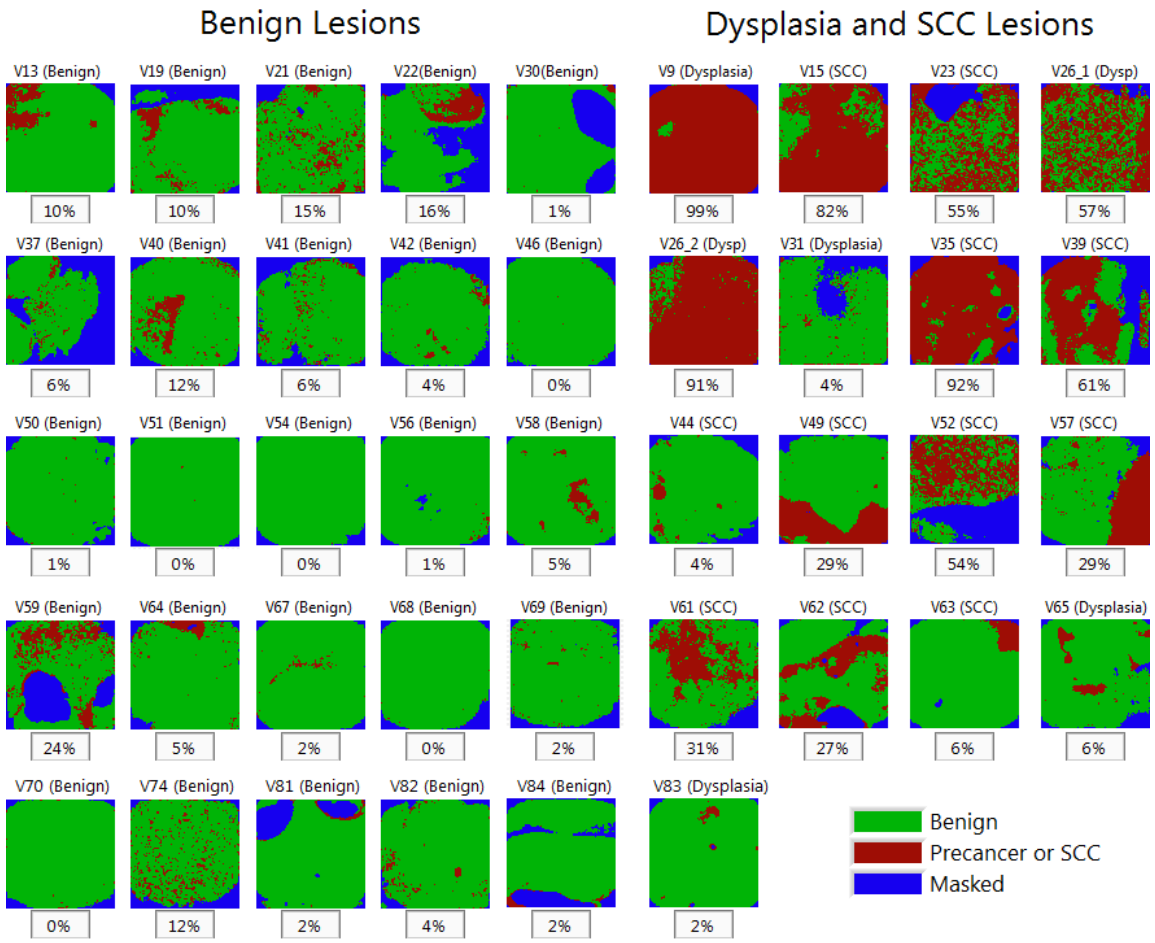

Figure 22. Pixels classification map using 4 features using the datasets of all lesions. Percentage under each image is the percentage of malignant pixels.

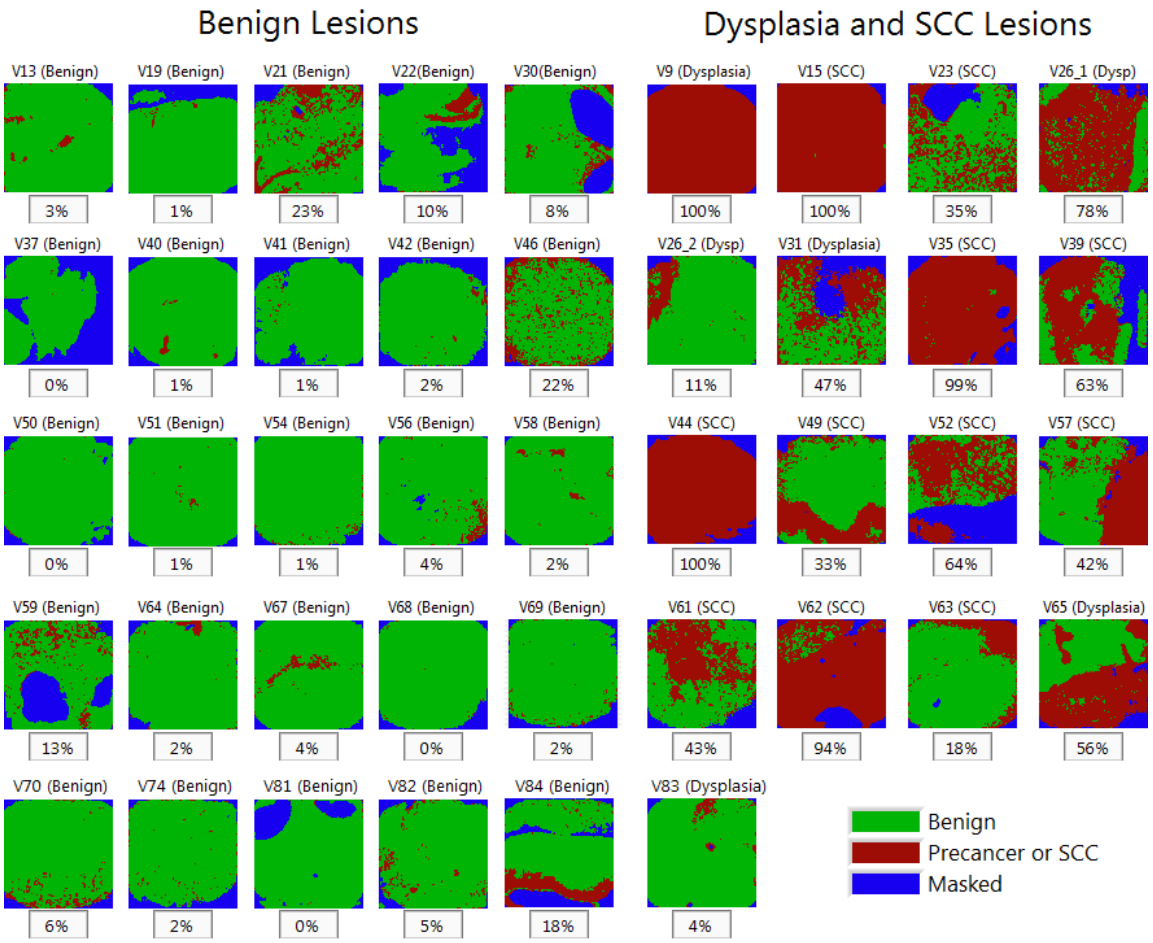

Figure 23. Pixels classification map using 5 features using the datasets of all lesions. Percentage under each image is the percentage of malignant pixels.

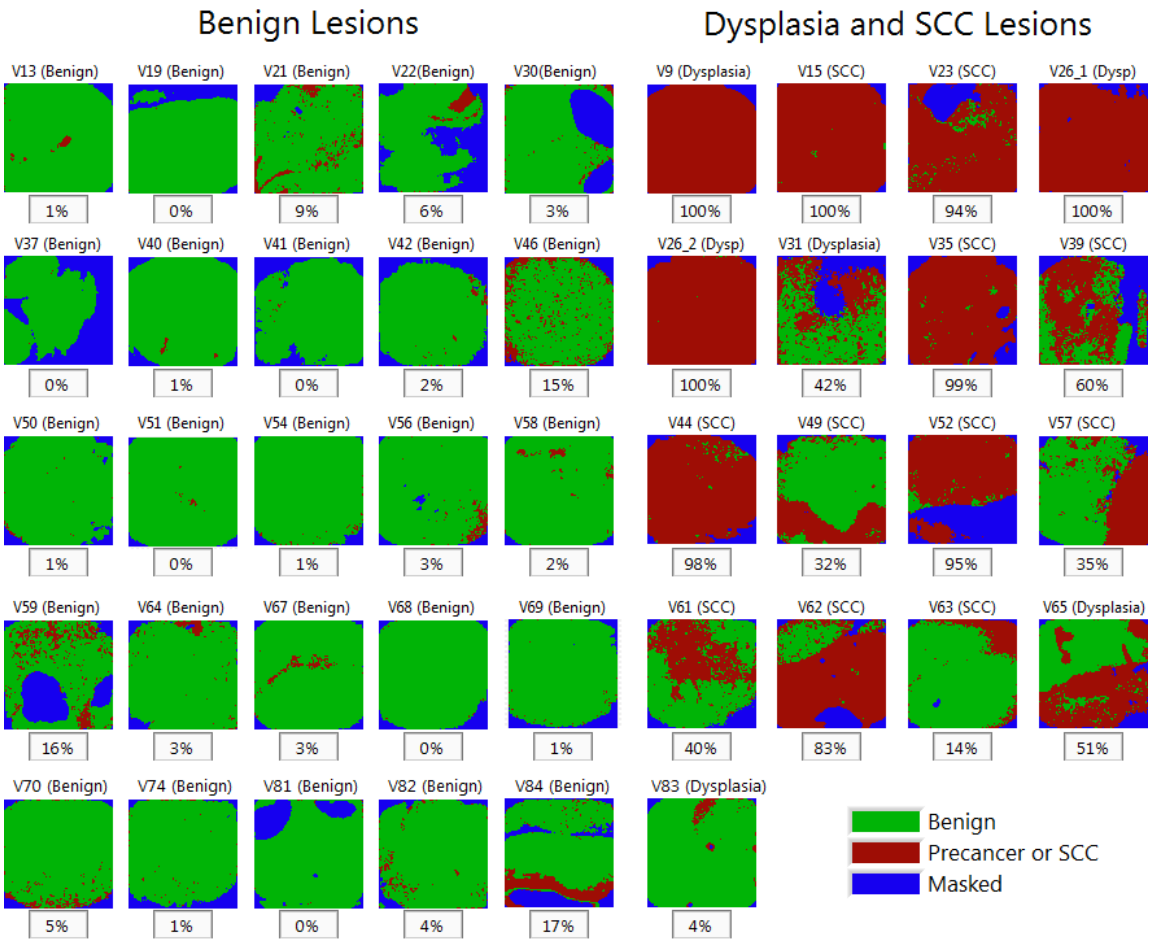

Figure 24. Pixels classification map using 6 features using the datasets of all lesions. Percentage under each image is the percentage of malignant pixels.

6.3.2 Tongue Classifier Results

Four different classifiers were trained, each one with either 3, 4, 5 or 6 features. The best features selected for each classifier are summarized in Table 15, and their corresponding LOOPCV confusion matrixes are shown in Table 16. The sensitivity and specificity values of each classifier are shown in Table 17. The pixel classification maps and the percentage of Dys/SCC pixels per image are shown in Figure 25, Figure 26, Figure

27 and Figure 28. As we can see from Table 17, the sensitivity and specificity is already 100% with a feature set of size 3, which suggest that the algorithm is not overfitting.

Table 15. Table showing the best subsets for the 4 classifiers using the datasets of all tongue lesions.

	3 Features	4 Features	5 Features	6 Features
	Feature ID	Feature ID	Feature ID	Feature ID
Features	Alg_6_1_Ref	R_Integrated_1_2	Alg_1_2	Alg_1_3
	N_Integrated_Int_2_Ref	Algo_8_1_Ref	N_Peak_Int_3	Alg_5_1_Ref
	R_Peak_1_3_Ref	N_Peak_Int_2_Ref	R_Peak_1_3	Alg_1_3_Ref
	-	R_Peak_1_3_Ref	Algo_8_1_Ref	N_Integrated_Int_2_Ref
	-		N_Peak_Int_1_Ref	N_Integrated_Int_3_Ref
	-		-	R_Peak_1_3_Ref

Table 16. Confusion matrixes for the 4 classifiers using the datasets of all tongue lesions.

3 Features

		Predicted	
		Positive	Negative
Observed	Positive	10	0
	Negative	0	8

4 Features

		Predicted	
		Positive	Negative
Observed	Positive	10	0
	Negative	0	8

5 Features

		Predicted	
		Positive	Negative
Observed	Positive	10	0
	Negative	0	8

6 Features

		Predicted	
		Positive	Negative
Observed	Positive	10	0
	Negative	0	8

Table 17. Sensitivity and specificity of detecting Dys/SCC lesions for the 4 classifiers using the datasets of all tongue lesions.

	Sensitivity			Specificity		
		95% Confidence Interval			95% Confidence Interval	
Subset	Estimated Value	Lower Limit	Upper Limit	Estimated Value	Lower Limit	Upper Limit
3 Features	1	0.65	1	1	0.59	1
4 Features	1	0.65	1	1	0.59	1
5 Features	1	0.65	1	1	0.59	1
6 Features	1	0.65	1	1	0.59	1

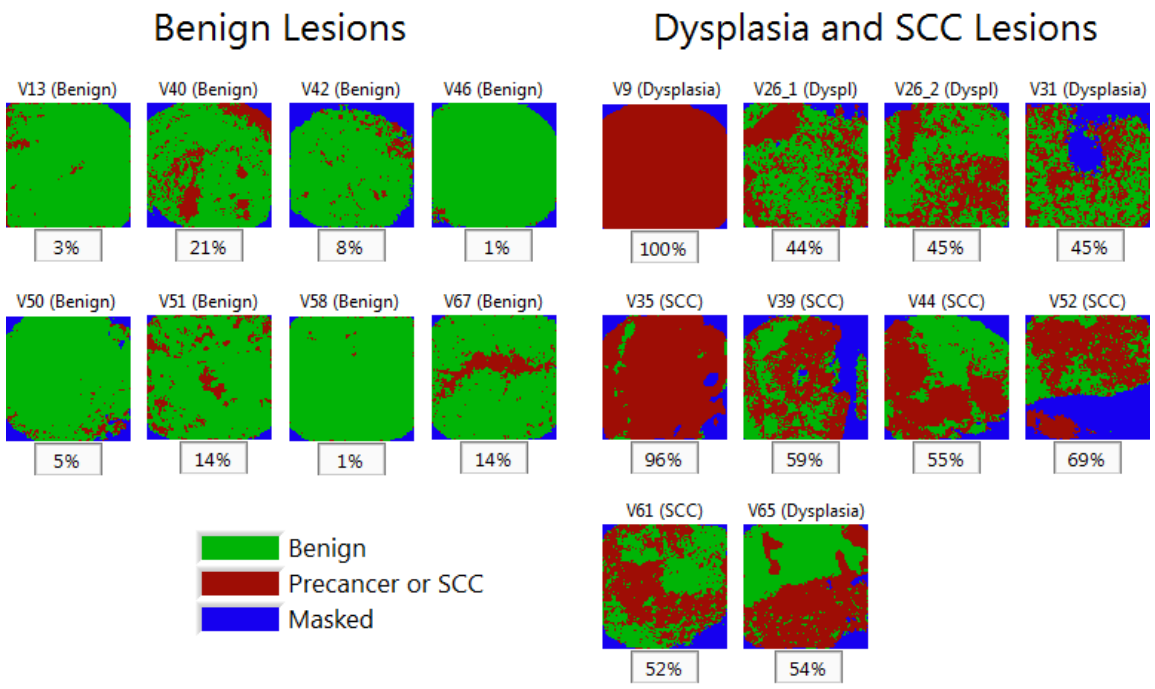

Figure 25. Pixels classification map using 3 features using the datasets of all tongue lesions. Percentage under each image is the percentage of malignant pixels.

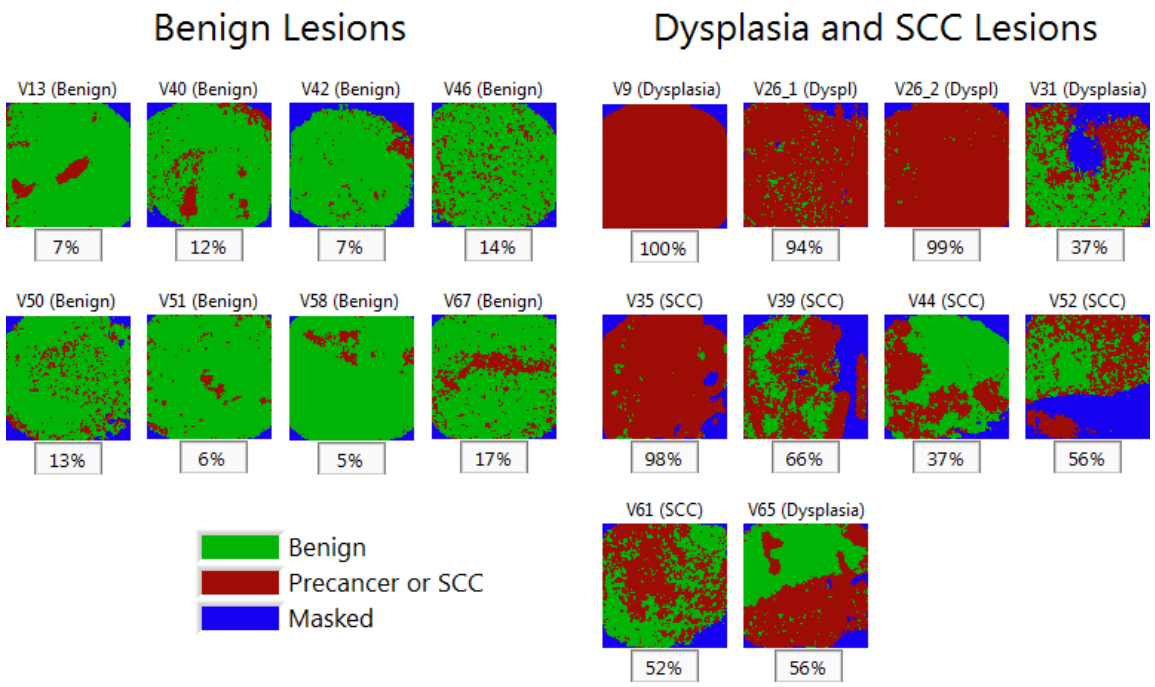

Figure 26. Pixels classification map using 4 features using the datasets of all tongue lesions. Percentage under each image is the percentage of malignant pixels.

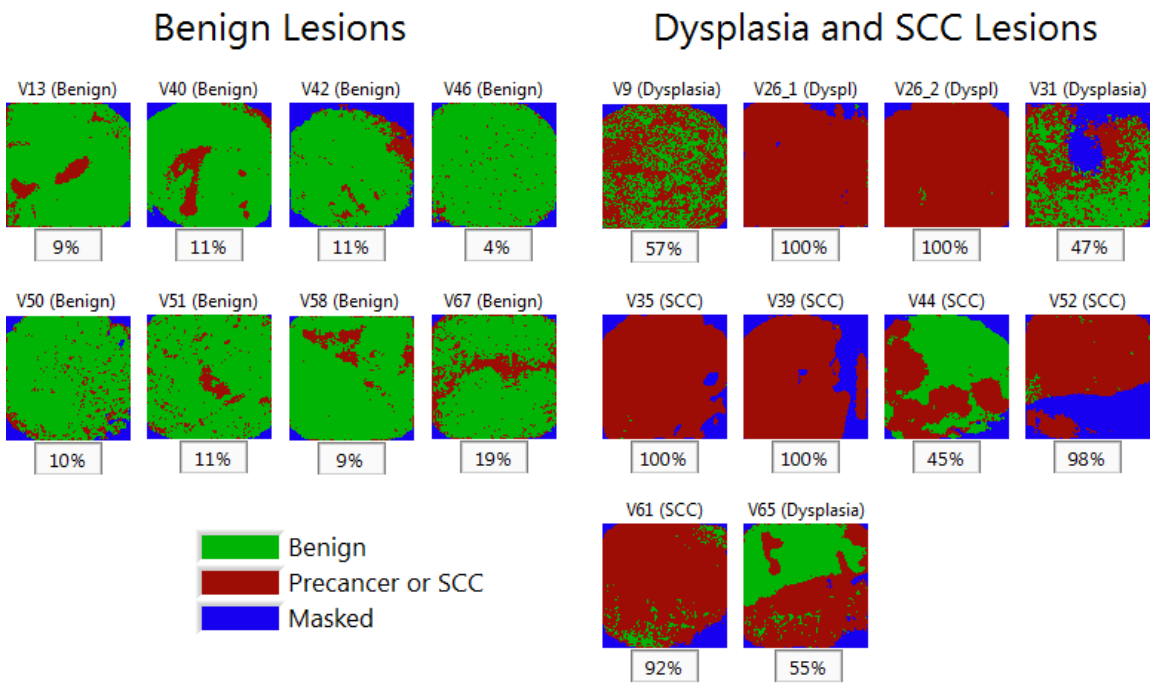

Figure 27. Pixels classification map using 5 features using the datasets of all tongue lesions. Percentage under each image is the percentage of malignant pixels.

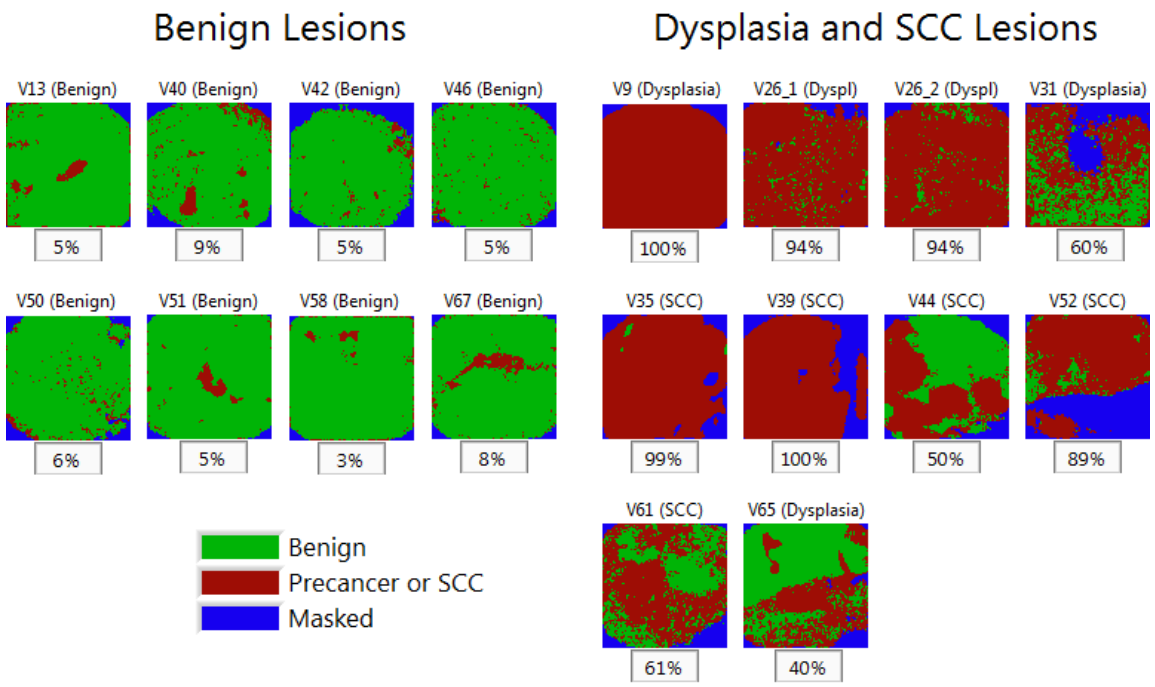

Figure 28. Pixels classification map using 6 features using the datasets of all tongue lesions. Percentage under each image is the percentage of malignant pixels.

6.3.3 Gingiva Classifier Results

Four different classifiers were trained, each one with either 3, 4, 5 or 6 features. The best features selected for each classifier are summarized in Table 18, and their corresponding LOOPCV confusion matrixes are shown in Table 19. The sensitivity and specificity values of each classifier are shown in Table 20. The pixel classification maps and the percentage of Dys/SCC pixels per image are shown in Figure 29, Figure 30, Figure 31 and Figure 32. As we can see from Table 20, the sensitivity and specificity is already 100% with a feature set size 3, which again indicates that the algorithm is not overfitting.

Table 18. Table showing the best subsets for the 4 classifiers using the datasets of all gingiva lesions.

	3 Features		4 Features		5 Features		6 Features	
	#	Feature ID	#	Feature ID	#	Feature ID	#	Feature ID
Features	33	N_Peak_Int_3	21	Alg_1_3	21	Alg_1_3	5	Alg_5_1
	41	R_Integrated_2_3	22	Alg_2_3	22	Alg_2_3	40	R_Integrated_1_2
	67	Alg_5_3_Ref	41	R_Integrated_1_3	41	R_Integrated_1_3	41	R_Integrated_1_3
			75	N_Peak_Int_3_Ref	73	N_Peak_Int_1_Ref	53	Alg_1_2_Ref
			-	-	75	N_Peak_Int_3_Ref	66	Alg_4_3_Ref
			-	-	-	-	78	N_Integrated_Int_3_Ref

Table 19. Confusion matrixes for the 4 classifiers using the datasets of all gingiva lesions.

3 Features

		Predicted	
		Positive	Negative
Observed	Positive	5	0
	Negative	0	9

4 Features

		Predicted	
		Positive	Negative
Observed	Positive	5	0
	Negative	0	9

5 Features

		Predicted	
		Positive	Negative
Observed	Positive	5	0
	Negative	0	9

6 Features

		Predicted	
		Positive	Negative
Observed	Positive	5	0
	Negative	0	9

Table 20. Sensitivity and specificity of detecting Dys/SCC lesions for the 4 classifiers using the datasets of all gingiva lesions.

	Sensitivity			Specificity		
		95% Confidence Interval			95% Confidence Interval	
Subset	Estimated Value	Lower Limit	Upper Limit	Estimated Value	Lower Limit	Upper Limit
3 Features	1	0.46	1	1	0.62	1
4 Features	1	0.46	1	1	0.62	1
5 Features	1	0.46	1	1	0.62	1
6 Features	1	0.46	1	1	0.62	1

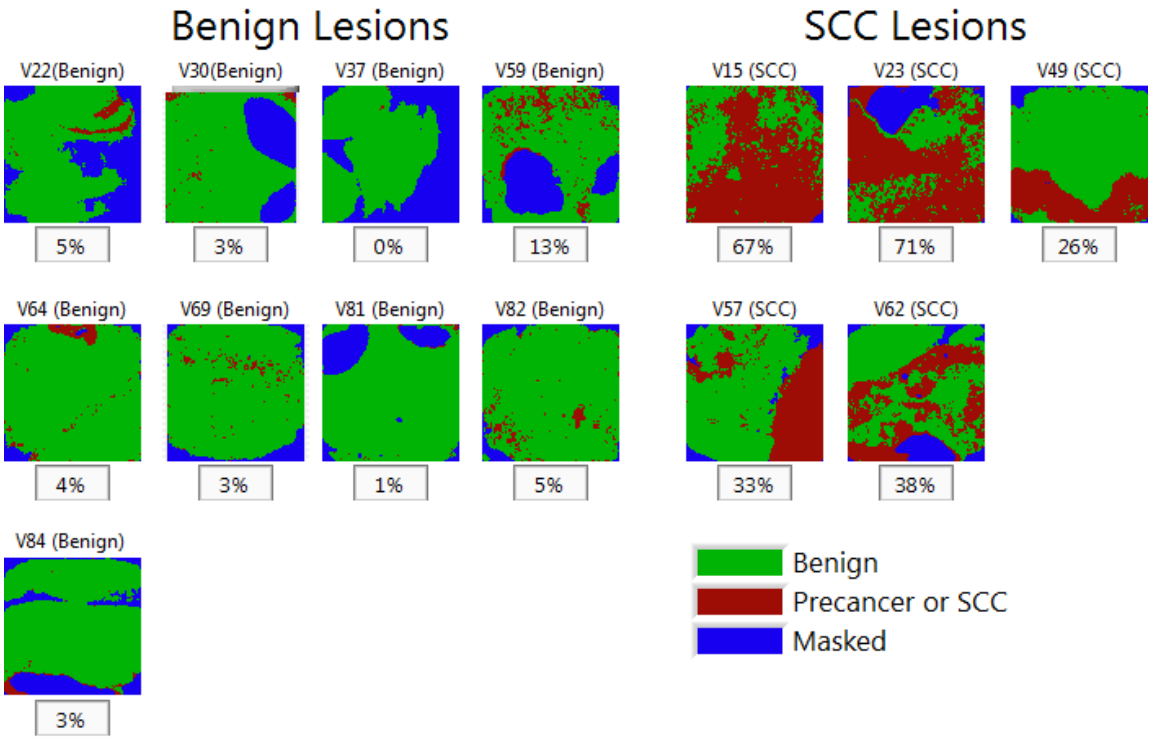

Figure 29. Pixels classification map using 3 features using the datasets of all gingiva lesions. Percentage under each image is the percentage of malignant pixels.

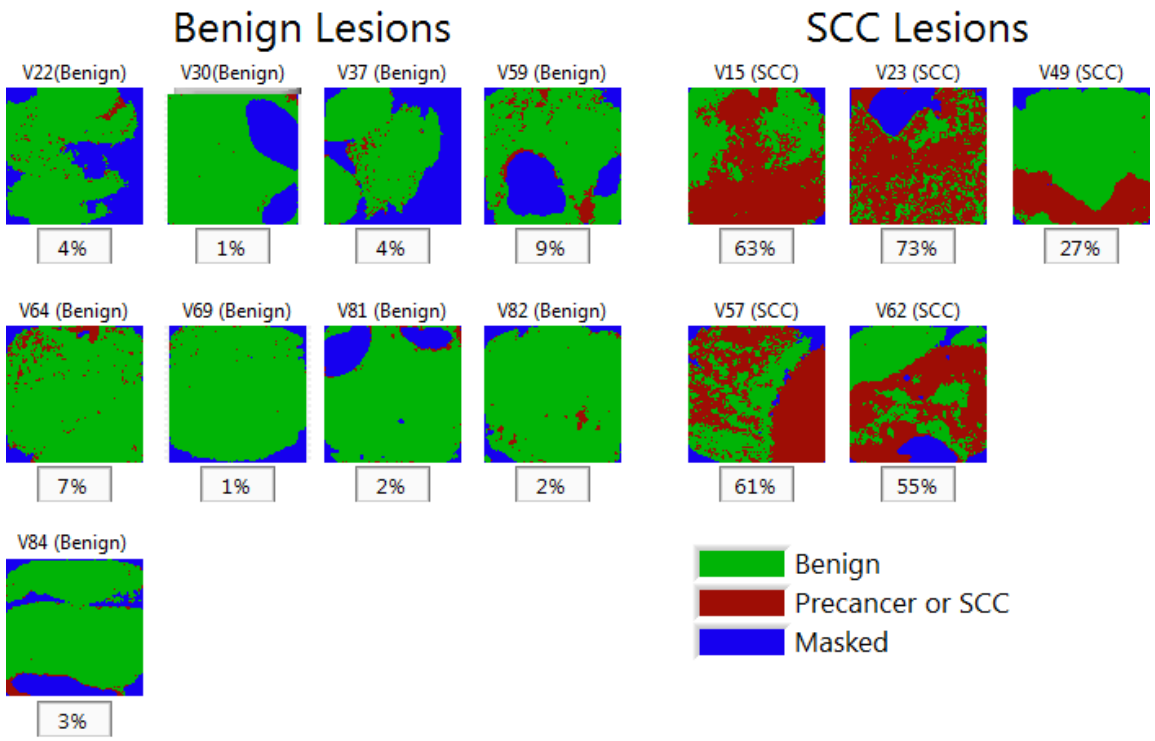

Figure 30. Pixels classification map using 4 features using the datasets of all gingiva lesions. Percentage under each image is the percentage of malignant pixels.

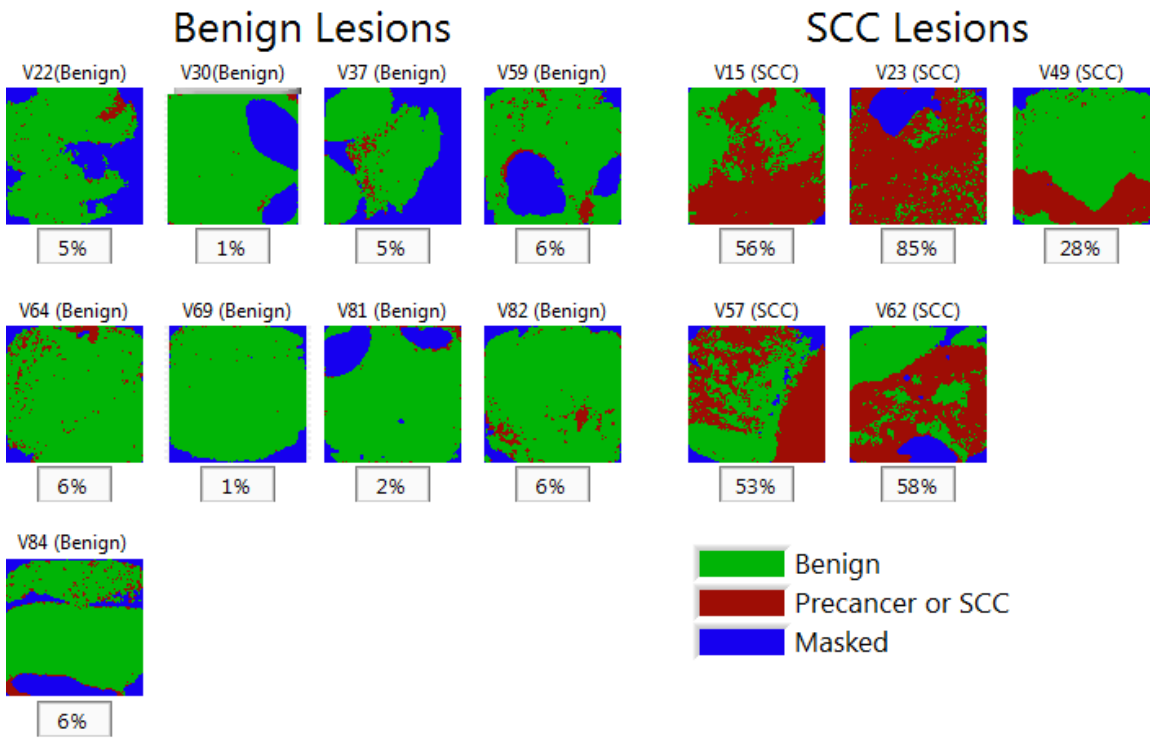

Figure 31. Pixels classification map using 5 features using the datasets of all gingiva lesions. Percentage under each image is the percentage of malignant pixels.

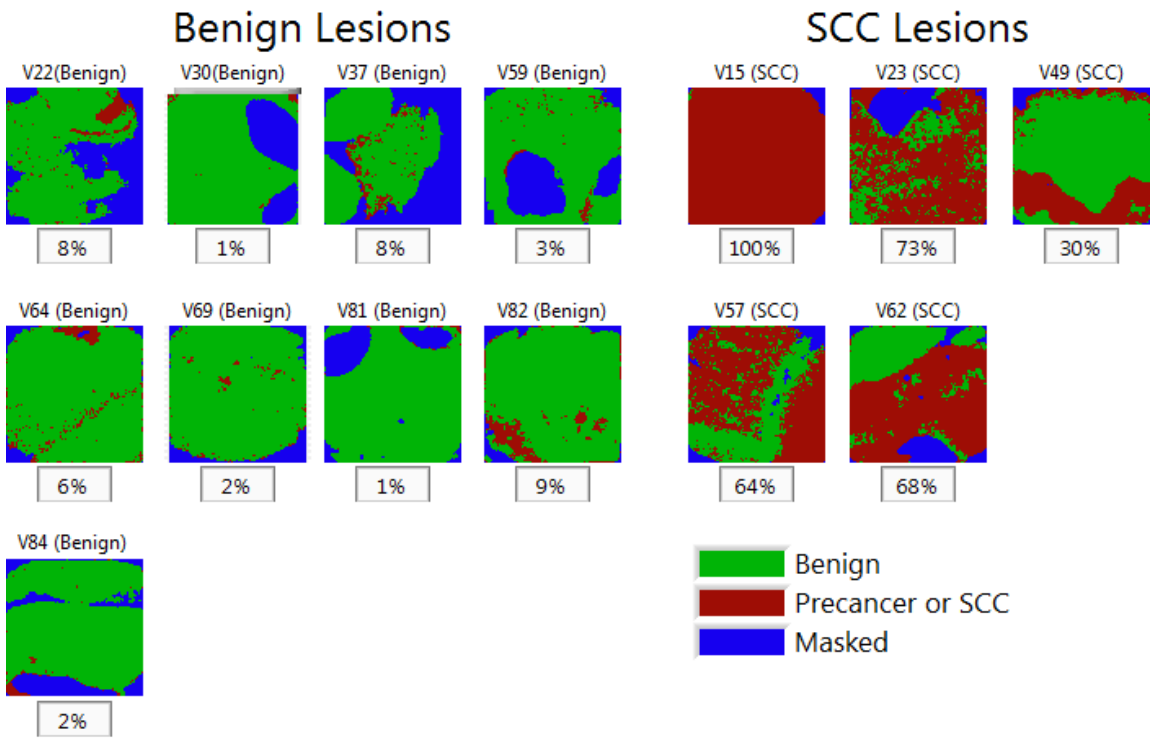

Figure 32. Pixels classification map using 6 features using the datasets of all gingiva lesions. Percentage under each image is the percentage of malignant pixels.

6.3.4 Oral Mucosa Classifier Results

Four different classifiers were trained, each one with either 3, 4, 5 or 6 features. The best features selected for each classifier are summarized in Table 21, and their corresponding LOOPCV confusion matrixes are shown in Table 22. The sensitivity and specificity values of each classifier are shown in Table 23. The pixel classification maps and the percentage of Dys/SCC pixels per image are shown in Figure 33, Figure 34, Figure 35 and Figure 36. Even though the performance of the algorithm is perfect, due to the few

samples, this performance is probably overoptimistic and additional samples are needed to estimate the true performance of this classifier.

Table 21. Table showing the best subsets for the 4 classifiers using the datasets of all oral mucosa lesions.

	3 Features		4 Features		5 Features		6 Features	
	#	Feature ID	#	Feature ID	#	Feature ID	#	Feature ID
Features	24	Alg_4_3	23	Alg_3_3	23	Alg_3_3	23	Alg_3_3
	65	Alg_3_3_Ref	59	Alg_7_2_Ref	27	Alg_7_3	28	Alg_8_3
	72	Hst_Lif_3_Ref	66	Alg_4_3_Ref	43	Alg_1_1_Ref	36	N_Integrated_Int_3
			67	Alg_5_3_Ref	66	Alg_4_3_Ref	44	Alg_2_1_Ref
			-	-	67	Alg_5_3_Ref	66	Alg_4_3_Ref
			-	-	-	-	67	Alg_5_3_Ref

Table 22. Confusion matrixes for the 4 classifiers using the datasets of all oral mucosa lesions.

3 Features

		Predicted	
		Positive	Negative
Observed	Positive	2	0
	Negative	0	8

4 Features

		Predicted	
		Positive	Negative
Observed	Positive	2	0
	Negative	0	8

5 Features

		Predicted	
		Positive	Negative
Observed	Positive	2	0
	Negative	0	8

6 Features

		Predicted	
		Positive	Negative
Observed	Positive	2	0
	Negative	0	8

Table 23. Sensitivity and specificity of detecting Dys/SCC lesions for the 4 classifiers using the datasets of all oral mucosa lesions.

	Sensitivity			Specificity		
		95% Confidence Interval			95% Confidence Interval	
Subset	Estimated Value	Lower Limit	Upper Limit	Estimated Value	Lower Limit	Upper Limit
3 Features	1	0.19	1	1	0.59	1
4 Features	1	0.19	1	1	0.59	1
5 Features	1	0.19	1	1	0.59	1
6 Features	1	0.19	1	1	0.59	1

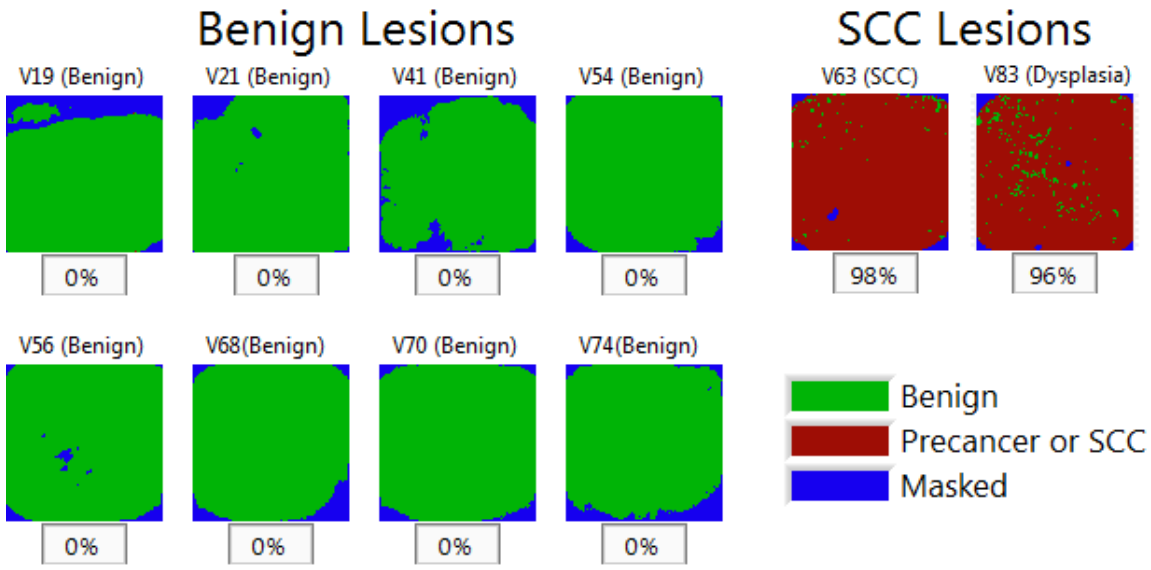

Figure 33. Pixels classification map using 3 features using the datasets of all oral mucosa lesions. Percentage under each image is the percentage of malignant pixels.

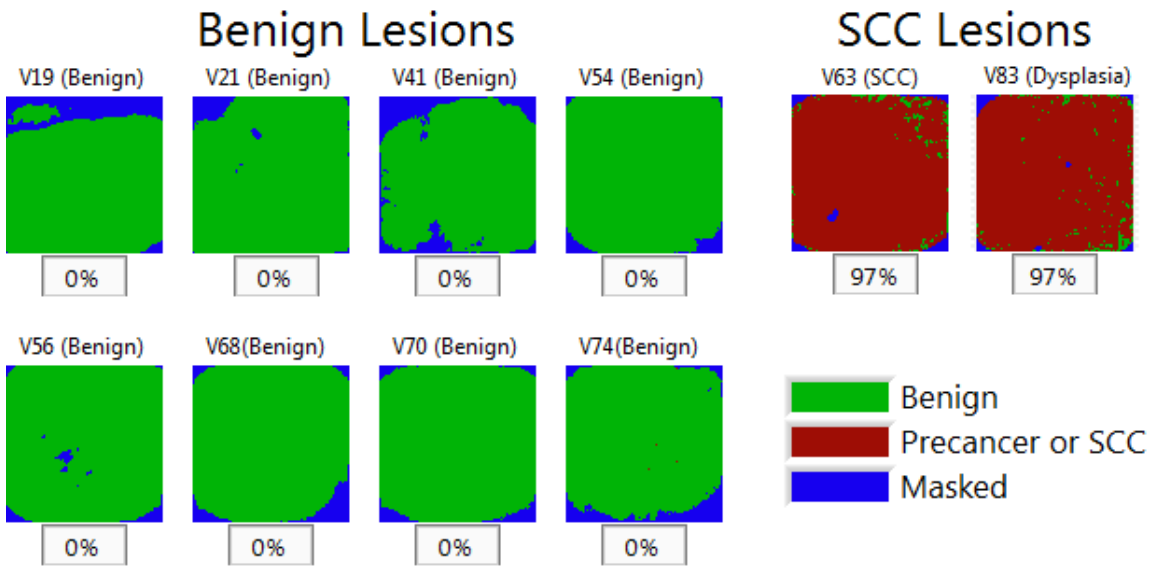

Figure 34. Pixels classification map using 4 features using the datasets of all oral mucosa lesions. Percentage under each image is the percentage of malignant pixels.

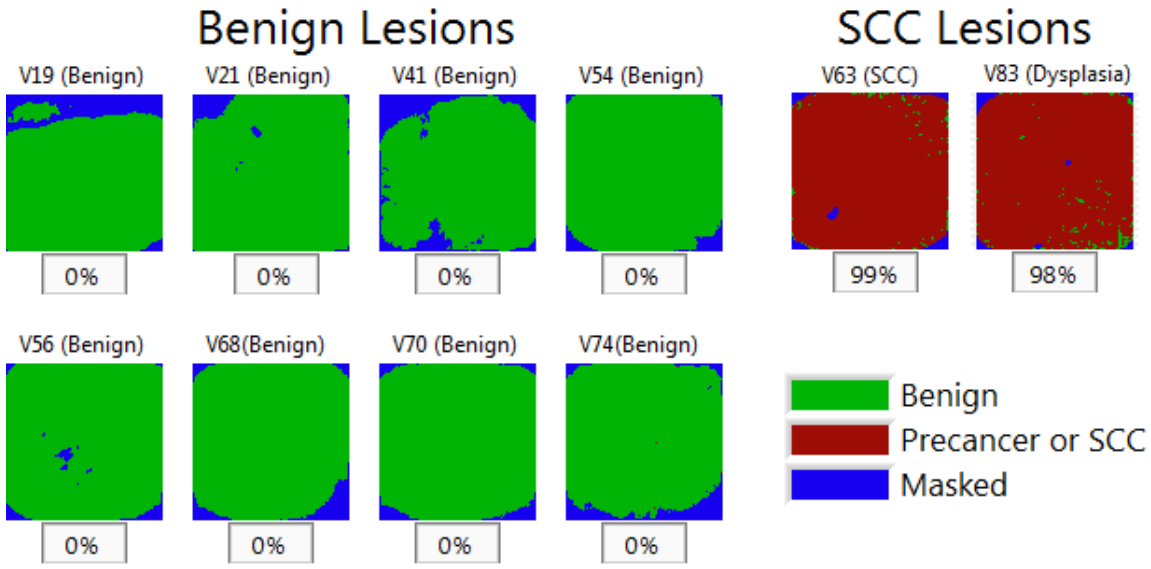

Figure 35. Pixels classification map using 5 features using the datasets of all oral mucosa lesions. Percentage under each image is the percentage of malignant pixels.

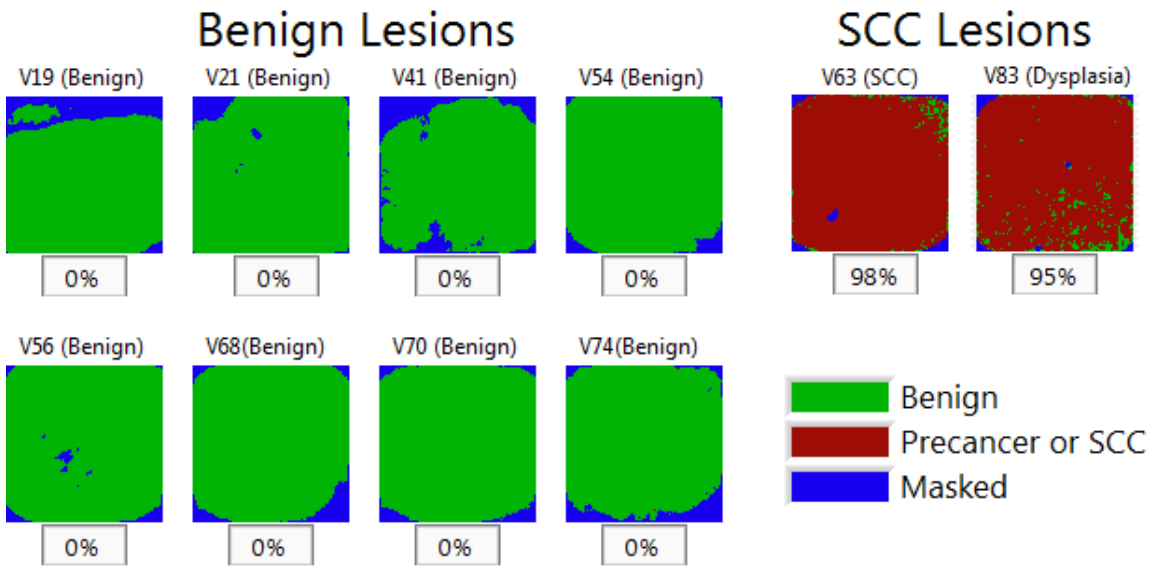

Figure 36. Pixels classification map using 6 features using the datasets of all oral mucosa lesions. Percentage under each image is the percentage of malignant pixels.

6.4 Discussion and Conclusion

This study demonstrates the potential of FLIM to differentiate between precancerous (mild Dysplasia) and cancerous (SCC) lesions from a wide range of benign lesions. The best classifier (using 6 features) trained on all the lesions misclassified only two lesions, which corresponded to the only two Dys/SCC samples from oral mucosa. These might indicate that the two malignant images are different that all the other malignant cases and the performance can be improved by increasing the FLIM database of oral mucosa lesions.

The other three location-specific classifiers were able to reach sensitivity and specificity of 100%. Although these values are probably overoptimistic due to the small sample size, these results are encouraging. In addition, in all cases only three features were

needed, which reduces the probability of overfitting. Although cross-validation method can remove the bias, there is still the possibility that we are overestimating the data by selecting the best possible result. This also applies to the feature selection search, by using all the data in the process we can get overly optimistic results [65, 66]. Nevertheless it shows the potential of this classifiers to become a CADSS system.

There are several limitations to this study. First, the sample size is small and many more patients need to be recruited into our ongoing study. Second, when annotating our data based on the histopathology evaluation, the whole lesion was assigned to a single category in spited of the fact that not all the pixels for that lesion corresponds to the same class. This problem can perhaps be mitigated by exploring unsupervised training algorithms, such as clustering or association rule learning[67]. Another issue we need to address is how the entire lesion is assessed based on the pixel classification maps. We are currently using a threshold of 25% pixels classified as Dys/SCC in order to favor sensitivity over specificity, since for cancer diagnosis it is preferable to have a higher rate of false positives than that of false negatives.

In conclusion, we have demonstrated that FLIM has the potential to distinguish dysplastic and SCC lesions from many benign conditions. Our results also show that our proposed bi-exponential deconvolution algorithm can be also used to extract valuable FLIM features for diagnostic purposes. Altogether, this work has demonstrated the potentials of endogenous FLIM endoscopy as a clinical tool for early detection of oral epithelial cancer. Our future efforts will be focused on continue collecting more data and

improving our classification algorithms to fully demonstrate the capabilities of endogenous FLIM for early detection of oral epithelial cancer.

7. CONCLUSIONS AND FUTURE WORK

7.1 Conclusions

There is no doubt that FLIM has the potential to become a clinical diagnosis technique for several diseases. A central issue for the translation of FLIM into the medical field is the development of a robust, fast and cost-effective FLIM instrumentation suitable for *in vivo* tissue imaging [8]. The main goal of this dissertation was to develop tools that can help to the transition of FLIM systems into the medical field. First, an endoscopic system for fast (0.5-4 frames/second) endogenous FLIM imaging of oral lesions was developed. The FLIM endoscope system is currently being evaluated at Texas A&M University College of Dentistry. This system enable the fast acquisition and large field of view needed for clinical diagnosis. Second, a novel fluorescence lifetime estimation algorithm was developed to achieve robust, accurate, and real-time fluorescence lifetime estimation. This algorithm is enabling real-time FLIM image processing and visualization during the endoscopic examination of patients with suspicious oral lesions. The results showed that the performance of the algorithm are in the same order as the one from the nonlinear LSIR algorithm but more than 2 orders of magnitude faster. Finally, the endoscopic endogenous FLIM data from suspicious oral lesions collected at the Texas A&M College of Dentistry was used to develop machine learning algorithms for automated identification of pre-cancerous and cancerous from benign oral epithelial lesions. Our results indicate that endogenous FLIM endoscopy can detect oral epithelial pre-cancer and cancer from a wider range of benign condition, with levels of sensitivity and specificity above 85%.

All this tools together allow us to acquire, process, display and diagnose an oral lesion in real time. Moreover, with some modifications this tools can be applied to other cancer locations and diseases.

7.2 Future Work

The system is still collecting data at Texas A&M College of Dentistry, by collecting data we'll be improving the algorithms performance, and also allow us to try new algorithms like unsupervised training algorithms and neural networks.

Also a new FLIM system will be collecting data in a hospital in Qatar, the system will be imaging patients that undergo surgery. An implementation of the classifier algorithm will be performed to be able to test the classification maps and the diagnosis in real-time.

REFERENCES

1. Valdés, P.A., et al., *Combined fluorescence and reflectance spectroscopy for in vivo quantification of cancer biomarkers in low-and high-grade glioma surgery.* J Biomed Opt, 2011. **16**(11): p. 116007-11600714.

2. Jabbour, J.M., et al., *Fluorescence lifetime imaging and reflectance confocal microscopy for multiscale imaging of oral precancer.* J Biomed Opt, 2013. **18**(4): p. 046012.

3. Meier, J.D., et al., *Time-resolved laser-induced fluorescence spectroscopy as a diagnostic instrument in head and neck carcinoma.* Otolaryngol Head Neck Surg, 2010. **142**(6): p. 838-44.

4. Park, J., et al., *Biochemical characterization of atherosclerotic plaques by endogenous multispectral fluorescence lifetime imaging microscopy.* Atherosclerosis, 2012. **220**(2): p. 394-401.

5. Marcu, L., et al., *Discrimination of human coronary artery atherosclerotic lipid-rich lesions by time-resolved laser-induced fluorescence spectroscopy.* Arteriosclerosis Thrombosis and Vascular Biology, 2001. **21**(7): p. 1244-1250.

6. Bastiaens, P.I.H. and A. Squire, *Fluorescence lifetime imaging microscopy: spatial resolution of biochemical processes in the cell.* Trends in Cell Biology, 1999. **9**(2): p. 48-52.

7. Sun, Y., R.N. Day, and A. Periasamy, *Investigating protein-protein interactions in living cells using fluorescence lifetime imaging microscopy.* Nat. Protocols, 2011. **6**(9): p. 1324-1340.

8. Shrestha, S., et al., *High-speed multispectral fluorescence lifetime imaging implementation for in vivo applications.* Opt. Lett., 2010. **35**(15): p. 2558-2560.

9. Jiang, P.C., W.S. Grundfest, and O.M. Stafsudd, *Quasi-real-time fluorescence imaging with lifetime dependent contrast.* J Biomed Opt, 2011. **16**(8): p. 086001.

10. Howlader, N., et al., *SEER Cancer Statistics Review, 1975-2013*, 2015, National Cancer Institute.

11. The Oral Cancer Foundation. *Oral Cancer Facts*. 2017; Available from: http://oralcancerfoundation.org.

12. Ahn, Y.C., et al., *Multimodality approach to optical early detection and mapping of oral neoplasia.* J Biomed Opt, 2011. **16**(7): p. 076007.

13. Jo, J.A., et al., *In vivo simultaneous morphological and biochemical optical imaging of oral epithelial cancer.* IEEE Trans Biomed Eng, 2010. **57**(10): p. 2596-9.

14. Belle, A., M.A. Kon, and K. Najarian, *Biomedical informatics for computer-aided decision support systems: a survey.* ScientificWorldJournal, 2013. **2013**: p. 769639.

15. Watcharapichat, P., *Image processing and classification algorithm to detect cancerous cells morphology when using in-vivo probe-based confocal laser endomicroscopy for the lower gastrointestinal tract.*, 2012, Imperial College London.

16. Zhengmao, Y. and G. Auner, *Principal component analysis approach for biomedical sample identification*, in *2004 IEEE International Conference on Systems, Man and Cybernetics* 2004. p. 1348-1353.

17. Peng, H., F. Long, and C. Ding, *Feature selection based on mutual information criteria of max-dependency, max-relevance, and min-redundancy.* IEEE Transactions on Pattern Analysis and Machine Intelligence, 2005. **27**(8): p. 1226-1238.

18. Hastie, T., R. Tibshirani, and J.H. Friedman, *The elements of statistical learning : data mining, inference, and prediction*. 3rd ed. 2009: Springer New York.

19. Lakowicz, J.R., *Principles of Fluorescence Spectroscopy*. 3rd ed. 2006: Springer US.

20. Becker, W., *Fluorescence lifetime imaging--techniques and applications.* J Microsc, 2012. **247**(2): p. 119-36.

21. Ware, W.R., L.J. Doemeny, and T.L. Nemzek, *Deconvolution of fluorescence and phosphorescence decay curves. Least-squares method.* J Phys Chem, 1973. **77**(17): p. 2038-2048.

22. Woods, R.J., et al., *Transient digitizer for the determination of microsecond luminescence lifetimes.* Anal Chem, 1984. **56**(8): p. 1395-400.

23. Huen, T., *Phase-plane method of exponential waveform measurement.* Review of Scientific Instruments, 1969. **40**: p. 1067-1069.

24. Matheson, I.B.C., *The Method of Successive Integration: a General Technique for Recasting Kinetic Equations in a Readily Soluble Form Which Is Linear in the Coefficients and Sufficiently Rapid for Real Time Instrumental Use.* Instrum Sci Technol, 1987. **16**(3): p. 345-373.

25. Halmer, D., et al., *Fast exponential fitting algorithm for real-time instrumental use.* Rev Sci Instrum, 2004. **75**(6): p. 2187-2191.

26. Yu, H., et al., *Estimation of Fluorescence Lifetimes Via Rotational Invariance Techniques.* IEEE Trans Biomed Eng, 2016. **63**(6): p. 1292-300.

27. Colyer, R., et al., *Phasor-based single-molecule fluorescence lifetime imaging using a wide-field photon-counting detector*, in *Proc SPIE Int Soc Opt Eng* 2009. p. 71850T-71850T.

28. Jo, J.A., et al., *Fast model-free deconvolution of fluorescence decay for analysis of biological systems.* J Biomed Opt, 2004. **9**(4): p. 743-52.

29. Dabir, A.S., et al., *Fully automated deconvolution method for on-line analysis of time-resolved fluorescence spectroscopy data based on an iterative Laguerre expansion technique.* J Biomed Opt, 2009. **14**(2): p. 024030-024030.

30. Campos-Delgado, D.U., et al., *Blind deconvolution estimation of fluorescence measurements through quadratic programming.* J Biomed Opt, 2015. **20**(7): p. 075010-075010.

31. Liu, J., et al., *A novel method for fast and robust estimation of fluorescence decay dynamics using constrained least-squares deconvolution with Laguerre expansion.* Phys Med Biol, 2012. **57**(4): p. 843-65.

32. Pande, P. and J.A. Jo, *Automated analysis of fluorescence lifetime imaging microscopy (FLIM) data based on the Laguerre deconvolution method.* IEEE Trans Biomed Eng, 2011. **58**(1): p. 172-81.

33. Warren, S.C., et al., *Rapid Global Fitting of Large Fluorescence Lifetime Imaging Microscopy Datasets.* PLoS ONE, 2013. **8**(8): p. e70687.

34. Campos-Delgado, D.U., et al., *Deconvolution of fluorescence lifetime imaging microscopy by a library of exponentials.* Opt Express, 2015. **23**(18): p. 23748-67.

35. Elson, D.S., et al., *Single-shot fluorescence lifetime imaging using a novel segmented gated optical intensifier*, in *Conference on Lasers and Electro-Optics* 2004. p. 2

36. McGinty, J., et al., *Wide-field fluorescence lifetime imaging of cancer.* Biomed. Opt. Express, 2010. **1**(2): p. 627-640.

37. Grant, D.M., et al., *High speed optically sectioned fluorescence lifetime imaging permits study of live cell signaling events.* Opt. Express, 2007. **15**(24): p. 15656-15673.

38. Becker, W., B. Su, and A. Bergmann, *Fast-acquisition multispectral FLIM by parallel TCSPC*, in *Multiphoton Microscopy in the Biomedical Sciences IX* 2009, SPIE 7183. p. 718305-718305.

39. Gersbach, M., et al., *High frame-rate TCSPC-FLIM using a novel SPAD-based image sensor*, in *Detectors and Imaging Devices: Infrared, focal Plane, Single Photon* 2010, SPIE 7780. p. 77801H-77801H.

40. Cheng, S., et al., *Handheld multispectral fluorescence lifetime imaging system for in vivo applications.* Biomed Opt Express, 2014. **5**(3): p. 921-31.

41. Sun, Y., et al., *In vivo validation of a bimodal technique combining time-resolved fluorescence spectroscopy and ultrasonic backscatter microscopy for diagnosis of oral carcinoma.* J Biomed Opt, 2012. **17**(11): p. 116003.

42. American National Standards Institute and Laser Institute of America, *American National Standard for Safe Use of Lasers*. 2014: Laser Institute of America.

43. Ljung, G.M. and G.E. Box, *On a measure of lack of fit in time series models.* Biometrika, 1978. **65**(2): p. 297-303.

44. Houston, J.P., M.A. Naivar, and J.P. Freyer, *Digital analysis and sorting of fluorescence lifetime by flow cytometry.* Cytometry Part A, 2010. **77A**(9): p. 861-872.

45. Jenkins, P.L., et al., *Flow cytometric separation of spectrally overlapping fluorophores using multifrequency fluorescence lifetime analysis*, in *SPIE 7902, Imaging, Manipulation, and Analysis of Biomolecules, Cells, and Tissues IX* 2011. p. 790216-790216.

46. Barbieri, S., et al., *Impact of the calculation algorithm on biexponential fitting of diffusion-weighted MRI in upper abdominal organs.* Magn Reson Med, 2016. **75**(5): p. 2175-84.

47. Padilla-Parra, S., et al., *Quantitative FRET analysis by fast acquisition time domain FLIM at high spatial resolution in living cells.* Biophys J, 2008. **95**(6): p. 2976-88.

48. GedİK, N. and A. Atasoy, *A computer-aided diagnosis system for breast cancer detection by using a curvelet transform.* Turkish Journal of Electrical Engineering & Computer Sciences, 2013. **21**(4): p. 1002-1014.

49. Kowal, M., et al., *Computer-aided diagnosis of breast cancer based on fine needle biopsy microscopic images.* Comput Biol Med, 2013. **43**(10): p. 1563-72.

50. Soliman, O.S. and A.E. Hassanien, *A Computer Aided Diagnosis System for Breast Cancer Using Support Vector Machine*, in *Rough Sets and Current Trends in Computing* 2012, Springer. p. 106-115.

51. Shieh, Y., et al., *Computer-aided diagnosis of hyperacute stroke with thrombolysis decision support using a contralateral comparative method of CT image analysis.* J Digit Imaging, 2014. **27**(3): p. 392-406.

52. Mesejo, P., *Computer-Aided Classification of Gastrointestinal Lesions in Regular Colonoscopy.* IEEE Transactions on Medical Imaging, 2016. **35**(9): p. 2051-2063.

53. Mollersen, K., et al., *Computer-Aided Decision Support for Melanoma Detection Applied on Melanocytic and Nonmelanocytic Skin Lesions: A Comparison of Two Systems Based on Automatic Analysis of Dermoscopic Images.* Biomed Res Int, 2015. **2015**: p. 579282.

54. Skala, M.C., et al., *In vivo multiphoton fluorescence lifetime imaging of protein-bound and free nicotinamide adenine dinucleotide in normal and precancerous epithelia.* J Biomed Opt, 2007. **12**(2): p. 024014.

55. Muller, M.G., et al., *Spectroscopic detection and evaluation of morphologic and biochemical changes in early human oral carcinoma.* Cancer, 2003. **97**(7): p. 1681-92.

56. Awasthi, K., et al., *Sensitive detection of intracellular environment of normal and cancer cells by autofluorescence lifetime imaging.* J Photochem Photobiol B, 2016. **165**: p. 256-265.

57. Marcu, L., French, Paul M. W., and Elson, Daniel S., *Fluorescence Lifetime Spectroscopy and Imaging : Principles and Applications in Biomedical Diagnostics*. 1st ed. 2014, Baton Rouge, US: CRC Press.

58. Siqueira, L.F.S., et al., *LDA vs. QDA for FT-MIR prostate cancer tissue classification.* Chemometrics and Intelligent Laboratory Systems, 2017. **162**: p. 123-129.

59. Viswanath, S.E., et al., *Central gland and peripheral zone prostate tumors have significantly different quantitative imaging signatures on 3 Tesla endorectal, in vivo T2-weighted MR imagery.* J Magn Reson Imaging, 2012. **36**(1): p. 213-24.

60. Zelig, U., et al., *Early detection of breast cancer using total biochemical analysis of peripheral blood components: a preliminary study.* BMC Cancer, 2015. **15**(1): p. 1-10.

61. Zarei, S., M. Aminghafari, and H. Zali, *Application and Comparison of Different Linear Classification Methods for Breast Cancer Diagnosis.* International Journal of Analytical, Pharmaceutical and Biomedical Sciences, 2015. **4**(2): p. 123-129.

62. Tate, T.H., et al., *Multispectral fluorescence imaging of human ovarian and fallopian tube tissue for early-stage cancer detection.* J Biomed Opt, 2016. **21**(5): p. 56005.

63. Theodoridis, S., *Machine learning : a Bayesian and optimization perspective. Sergios Theodoridis*. 1st ed. 2015: London ; San Diego : Elsevier : Academic Press.

64. Foster, K.R., R. Koprowski, and J.D. Skufca, *Machine learning, medical diagnosis, and biomedical engineering research - commentary.* BioMedical Engineering OnLine, 2014. **13**: p. 94-94.

65. Kriegeskorte, N., et al., *Circular analysis in systems neuroscience: the dangers of double dipping.* Nature Neuroscience, 2009. **12**(5): p. 535-540.

66. Dietterich, T.G., *Approximate Statistical Tests for Comparing Supervised Classification Learning Algorithms.* Neural Computation, 1998. **10**(7): p. 1895-1923.

67. Cios, K.J., et al., *Data mining: a knowledge discovery approach*. 1st ed. 2007: Springer US.